Homoclinic snaking in discrete systems

Rudy Kusdiantara

A thesis presented for degree of
Doctor of Philosophy

Department of Mathematical Sciences
University of Essex

October 2018

 would like to dedicate this thesis to my loving parents,
my wife, and my son ...

Declaration

The work in this thesis is based on research carried out with my supervisor Dr. Hadi Susanto at the Department of Mathematical Sciences, University of Essex, United Kingdom. No part of this thesis has been submitted elsewhere for any other degree or qualification, and it is all my own work, unless referenced, to the contrary, in the text.

Rudy Kusdiantara
October 2018

Acknowledgements

First above all, I praise the Almighty Allah, the most Most Beneficent and most Merciful because of His favours and loves for giving me strength and spirit to accomplish this thesis.

Foremost, I would like to express my sincere gratitude to my supervisor Dr. Hadi Susanto for the continuous support of my Ph.D study and research, for his patience, motivation, enthusiasm, and immense knowledge. His guidance helped me in all the time of research and writing of this thesis. I could not have imagined having a better advisor and mentor for my Ph.D study.

Besides my advisor, I would like to thank my Chair of Supervisory Board and internal examiner Dr. Georgi Grahovski, for the supports, encouragement, and insightful comments. My sincere thanks also goes to my external examiner Dr. David Lloyd, for the advice, kindness and constructive questions.

The most heartfelt gratitude is to my beloved wife and best friend, Laelati Nurfitriani and my little prince Darish Rayyan Kusdiantara for their total moral support, patience, and motivations. I thank my fellow friends in our department: Mba Ilen, Mba Rahmi, Omar, Amal, Junaid, Tahani, Awatf, Lana, and Syilla, for the interesting group discussions and all the fun we had in the last four years and also my friends in Indonesian friends: Mas Arief's family, Mba Fira's family, Mas Rendra, Mba Ajeng, Bang Ahmad's family, Bu Rani's family, Mas Vogy, Pak Joash, Pak Nino, and many others for the help and during my time in UK.

Last but not the least, I would like to thank my family: my mother Ngatijah and my father Radi Puspa Wiranto, for giving birth to me at the first place and supporting me spiritually throughout my life and also for my brother Tangkas Kintoko Aji and sister Kinanti Firdasani for the moral support. I am thankful also to the Lembaga Pengelolaan Dana Pendidikan (Indonesia Endowment Fund for Education) for providing me financial support.

Abstract

In this thesis, we investigate analytically and numerically bifurcations of localized solutions in discrete systems, i.e., the discrete Swift-Hohenberg, an optical cavity equation, and the discrete Allen-Cahn equation, which have infinitely multiplicity called homoclinic snaking.

First, we study the discrete Swift-Hohenberg equation with cubic and quintic nonlinearity, obtained from discretizing the spatial derivatives of the Swift-Hohenberg equation using central finite differences. We investigate the discretization effect on the bifurcation behavior, where we identify three regions of the coupling parameter, i.e., strong, weak, and intermediate coupling. In the intermediate coupling region, multiple Maxwell points can occur for the periodic solutions and may cause irregular snaking and isolas. Theoretical analysis for the snaking and stability of the corresponding solutions is provided in the weak coupling region.

Next, we study time-independent solutions of an optical cavity equation with saturable nonlinearity. When the nonlinearity is of Kerr-type (i.e., cubic), one obtains the discrete version of Lugiato-Lefever equation. The equation admits uniform and localized solutions. Localized solutions can be formed by combining two different uniform states, which can develop a snaking structure in their bifurcation diagram when a control parameter is varied, i.e., homoclinic snaking. $\Subset$-shaped isolas may also occur when the background of localized states disappear at a certain bifurcation parameter value. The semi-analytical approximation is also proposed to determine the stability of the corresponding solutions.

Finally, we present a study on time-independent solutions of the two-dimensional discrete Allen-Cahn equation with cubic and quintic nonlinearity. Three different types of lattices are considered, i.e., square, honeycomb, and triangular lattices. Localized solutions of discrete Allen-Cahn equation also can be formed by com-

bining two different uniform states. We introduce an active-cell approximation, which is extended from the one-active site approximation in one-dimensional case for a weakly coupled system.

Publications

Most of the work of this thesis has been published or is submitted for publication.

- Parts of Chapter 2 in this thesis have been published in :
  R. Kusdiantara and H. Susanto. Homoclinic snaking in the discrete Swift-Hohenberg equation. *Physical Review E* ***96***, *062214* (2017).

- Parts of Chapter 3 in this thesis will be in :
  R. Kusdiantara, H. Susanto, and A. R. Champneys. Homoclinic snaking of discrete solitons in saturable optical cavities.

- Parts of Chapter 4 in this thesis have been submitted in :
  R. Kusdiantara and H. Susanto. Snakes in square, honeycomb, and triangular lattices. *Nonlinearity* (2018).

Additional works :

- H. Susanto, R. Kusdiantara, N. Li, O.B. Kirikchi, D. Adzkiya, E.R.M. Putri, and T. Asfihani. Snakes and ghosts in a parity-times-symmetric chain of dimers, *Physical Review E* ***97***, *062204* (2018).

- R. Rusin, R. Kusdiantara, and H. Susanto. Variational approximations using Gaussian ansatz, false instability, and its remedy in nonlinear Schrödinger lattices, accepted in *Journal of Physics A: Mathematical and Theoretical* (2018).

- Y. Muda, F.T. Akbar, R. Kusdiantaraa, B.E. Gunara, and H. Susanto. Justification of the rotating wave approximation in damped, driven weakly coupled oscillators, submitted to *Asymptotic Analysis* (2018).

- T. Al-Karkhi, R. Kusdiantara, H. Susanto, and E. Codling. Bloom formation and Turing patterns in a phytoplankton competition model, submitted to *Journal of Mathematical Biology* (2018).

- Y. Muda, F.T. Akbar, R. Kusdiantaraa, B.E. Gunara, and H. Susanto. Justification and numerical comparisons of the discrete nonlinear Schrodinger equation from a parametrically driven nonlinear Klein-Gordon equation with damping, submitted to *Nonlinear Dynamics* (2018).

Contents

Chapter 1

Introduction

1.1 What is pattern formation?

Patterns are distinguishable regularities of structure in the natural world [4, 5]. The pattern or organised complexity of structure needs not appear from something complicated, but it could be originated by simple physical laws. In general, there is no mathematical precise definition of patterns. One can say that patterns are related to repetition of similar structures and typically extended in space or time.

1.2 History

Research on patterns has a long history and goes back to ancient times with the study of geometry [15]. In the following, we will only name several figures from the 19th and 20th centuries and briefly discuss their results, that we find to be relevant to our study.

In 1873, Belgian physicist Joseph Plateau developed a *minimal surface* concept, namely a surface that locally minimizes its area from examining soap film (thin layers of liquid that are enveloped by air) [75].

Between 1899-1904, German biologist and artist Ernst Haeckel illustrated hundreds of various organisms and emphasised their symmetry in *Kunstformen der Natur* (Art Forms in Nature) to support Darwinian theory [49, 50].

German psychologist Adolf Zeising claimed that the *golden ratio* appeared in the arrangement of branches along stems of plans and veins in leaves. Then he extended his study to the proportion of chemical compounds, geometry of crystals, skeleton of animals, and branching of veins and nerves. From these phenomena, he saw that the *golden ratio* is [72] :

> *"the universal law in which contained the basic-principle of all the form of beauty and completeness in the realm of nature and art, and which permeates, as a paramount spiritual ideal, all structures, forms and proportions, whether cosmic or individual, organic or inorganic, acoustic or optical; which finds its fullest realization, however, in the human form.* [1] *"*

American photographer Wilson Bentley is the first known photographer of snowflakes. In 1885, he took the first micrograph of snowflakes and snowcrystals, see Fig. 1.1. He poetically described snowflakes as "tiny miracles of beauty" and snow crystals as "ice flowers" [12].

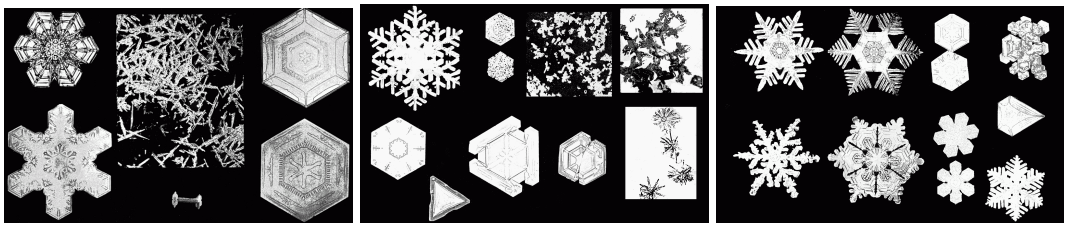

Figure 1.1. The first known micrograph of snowcrystals and snowflakes by Bentley [12].

English computer scientist, mathematician, cryptanalyst, and theoretical biologist Alan Turing analyzed the pattern creation in living organisms, called *morphogenesis*. In 1952, he suggested a system of chemical reactions modelled by a reaction-diffusion process of two catalysts in partial differential equations [89].

[1] Translated from Padovan [72], p.306

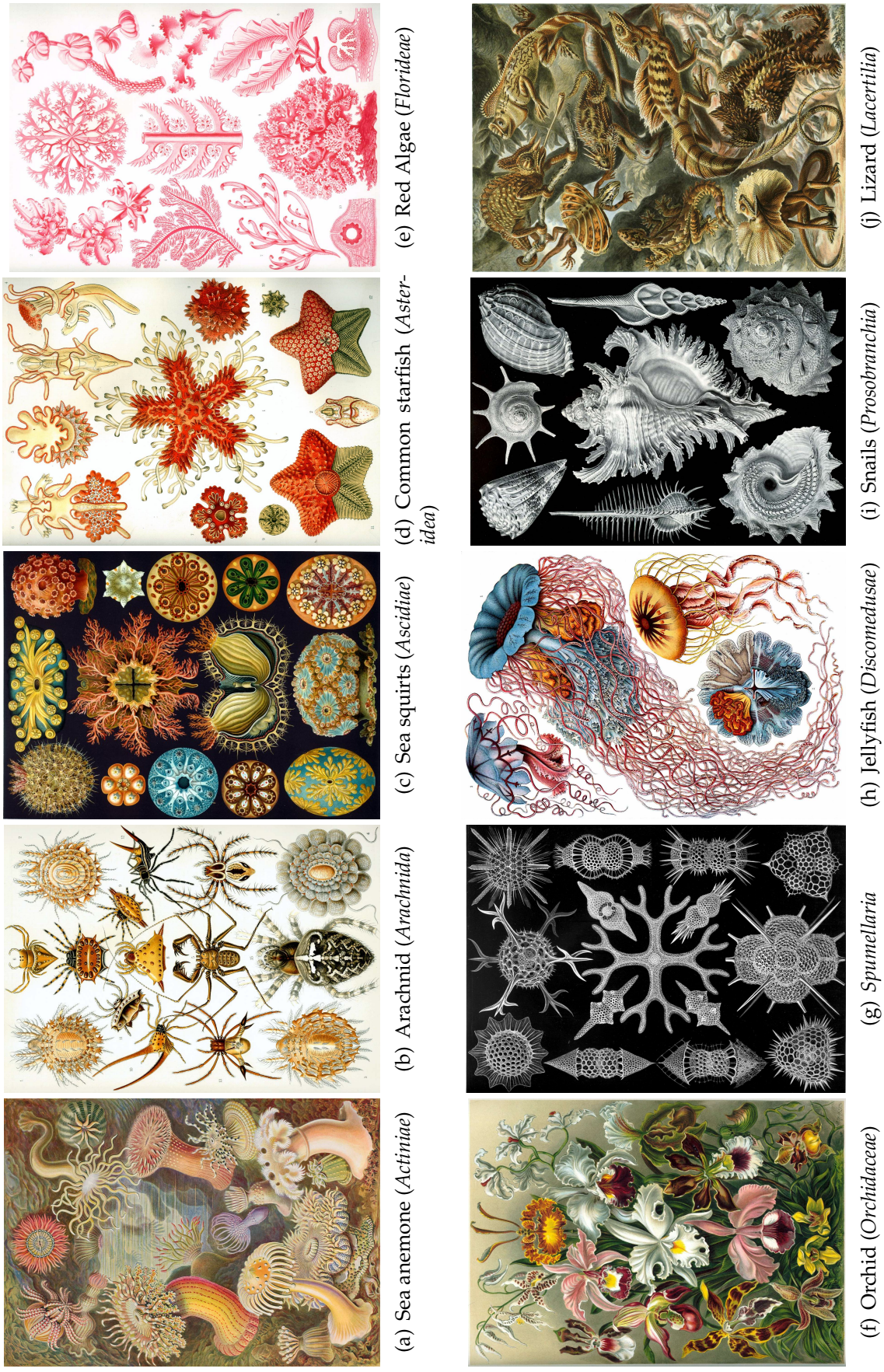

(a) Sea anemone (*Actiniae*) (b) Arachnid (*Arachnida*) (c) Sea squirts (*Ascidiae*) (d) Common starfish (*Asteridea*) (e) Red Algae (*Florideae*)

(f) Orchid (*Orchidaceae*) (g) *Spumellaria* (h) Jellyfish (*Discomedusae*) (i) Snails (*Prosobranchia*) (j) Lizard (*Lacertilia*)

Figure 1.2. Haeckel gallery of prints from *Kunstformen der Natur* (Art Forms in Nature) [49, 50].

Hungarian theoretical biologist Aristid Lindenmayer developed the L-system (Lindenmayer system), which is a parallel rewriting system and a type of formal grammar to illustrate the behavior of plant cells and to model plant developments. L-system could be used to illustrate the plants growth in style of *fractal* [63].

1.3 Types of pattern

Fractals

Fractals are used to explain naturally occurring objects. Expanding symmetry is when similar patterns increase in the small scale. Thus, it is called self-similar pattern if the replication is the same in every scale [13]. Fractal-like patterns in natures exhibit self-similarity, such as Romanesco broccoli, river networks, lightning bolt, snowflakes, etc.

Spirals

Spiral is a curve which emerges from a point, moving further away and revolving around the point. In physics, spirals are the lowest energy configuration which originates spontaneously from self-organizing processes in dynamical systems. In chemistry, spiral is generated by a reaction-diffusion process which involves activation and inhibition [39]. Examples of spirals patterns in nature can be seen in *phyllotaxis* plants, snail shells, sunflower, bighorn sheep, etc.

Flow and meanders

Pattern in nature may appear from flow, when a laminar (smooth) flow starts to break up because its velocity becomes larger than its viscosity [91]. Furthermore, these flows may form meander, i.e., when the fluid flows start to create a vortex which forms a positive feed back loop and accelerates erosion [93].

Waves and dunes

In physics, waves are disturbances that transfer energy through matters (air or water) or space and making their mediums oscillate as they pass by [45]. Dunes are created when wind passes over sand and forms ripple patterns in the large body of sand, i.e., sand in the dessert.

Bubbles and foam

Soap bubble is a very thin film of water soap enveloping air that forms an empty sphere with a surface that appears to gradually change colour (*iridescence*). Foams are mass bubbles that bond and form a structure, for example *Spumellaria* which has foam-like structure, see Fig. 1.2(g). Foams consist of soap films satisfying Plateau's laws [75].

Tessellations

Tessellation of flat surface is tiling of a plane using one or more geometric shapes by repeating the tiles, i.e., honeycomb, halite crystals, snakefruit scales, etc. By using mathematics, tessellations can be universalized to higher dimensions and complex geometries.

Cracks

Cracks are linear opening, which is formed in a material to reduce stress on the surface. It is also associated with the material elasticity. Hence, crack patterns in materials are indicator of the material's elasticity [82].

Spots and stripes

Spots and stripes commonly appear on animals, such as zebra, leopard, anglerfish, etc. for the purpose of camouflage [5]. This pattern helps them increase their chances to survive and preserve their species. The next function of patterns in animals skin is signalling and warning, for instance in ladybird and coral snake [92]. They will be avoided by their predators because of their bold colour. In particular, spots and stripes can also be explained by a reaction-diffusion system (*morphogenesis*) [89].

(a) Romanesco broccoli [2]

(b) Lichtenberg figure [3]

(c) *Phyllotaxis* of spiral aloe [4]

(d) Spiral of sunflower seed [5]

(e) Oxbow lake create meander pattern [6]

(f) Sand ripples on the dessert [7]

(g) Cube-shaped crystals of halite [8]

(h) Natural tessellation honeycomb [9]

(i) Overlapping scales of snakefruit [10]

(j) Cracks patten on dried sewage [11]

(k) Zebra stripes [12]

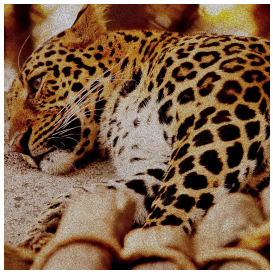

(l) Leopard spots [13]

Figure 1.3. Types of pattern in nature.

[2]*Brassica oleracea var. botrytis* by Coyau. Image downloaded from Wikimedia Common on April 2018.

[3]High voltage dielectric breakdown within a block of plexiglas creates a beautiful fractal pattern called a Lichtenberg Figure by Bert Hickman. Image downloaded from Wikimedia Common on April 2018.

[4]*Aloe polyphylla* Schönland ex Pillans by J. Brew. Image downloaded from Wikimedia Common on April 2018.

[5]Close up of *Helianthus annuus* by Michael Schönitzer. Image downloaded from Wikimedia Common on April 2018.

[6]Oxbow lake, Yamal Peninsula, Russia by Katorisi. Image downloaded from Wikimedia Common on April 2018.

[7]In the Mojave desert, near Kelso, California by Murray Foubister. Image downloaded from Wikimedia Common on April 2018.

[8]Specimen-grade example of salt in its native crystallized form by Rob Lavinsky. Image downloaded from Wikimedia Common on April 2018.

[9]Bee on his alvear by Giuliagi. Image downloaded from Wikimedia Common on April 2018.

[10]Salak or snakefruit by Takeaway. Image downloaded from Wikimedia Common on April 2018.

[11]Desiccation cracks in dried sludge of a sewage plant by Hannes Grobe. Image downloaded from Wikimedia Common on April 2018.

[12]Grevy's zebra striping pattern by Nojhan. Image downloaded from Wikimedia Common on April 2018.

[13]Common Leopard is also known as *Panthera pardus* was taken at Padmaja Naidu Himalayan Zoological Park by Riabonny. Image downloaded from Wikimedia Common on April 2018.

1.4 The Swift-Hohenberg equation

The Swift-Hohenberg equation is seen as a prototypical pattern forming system since it has the simplest finite-wavelength pattern forming instability [31]. In 1977, Swift and Hohenberg developed the model for Rayleigh-Bernard instability in roll waves [85]. We write the Swift-Hohenberg equation in the form [21]

$$\frac{\partial u}{\partial t} = ru - \left(\frac{\partial^2}{\partial x^2} + q_c^2\right)^2 u + b_3 u^3 - b_5 u^5, \tag{1.1}$$

where r is the control parameter and $q_c = 1$, $b_3 = 2$, $b_5 = 1$. The equation has two symmetries, i.e., invariant under $u \to -u$ and $x \to -x$. In the presence of periodic boundary conditions with period L, the equation possesses a Lyapunov functional F, which we refer to as an energy, given by [21]

$$\begin{aligned} F(u) &= \int_0^L \mathcal{J}(u)\,\mathrm{d}x \\ &= \int_0^L \left(-\frac{1}{2}ru^2 + \frac{1}{2}\left[\left(\frac{\partial^2}{\partial x^2} + q_c^2\right)u\right]^2 - \frac{1}{4}b_3u^4 + \frac{1}{6}b_5u^6\right)\mathrm{d}x, \end{aligned} \tag{1.2}$$

such that

$$u_t = -\frac{\delta F}{\delta u}. \tag{1.3}$$

It follows that along any trajectory the energy decreases to a (local) minimum in time, i.e.,

$$\frac{dF}{dt} = -\int_0^L (\partial_t u)^2\,\mathrm{d}x \le 0. \tag{1.4}$$

In particular, no Hopf bifurcations are possible and (at fixed x) all time dependence ultimately dies out [18–21]. The variational derivative F satisfies

$$\frac{\delta F}{\delta u} = \frac{\partial \mathcal{J}}{\partial u} - \frac{d}{dx}\frac{\partial \mathcal{J}}{\partial u_x}. \tag{1.5}$$

Equation (1.1) is a fourth order PDE in x which, in appropriate coordinates, obeys Hamilton's equations, i.e., [21]

$$\mathcal{H} = -\frac{1}{2}\left(r - q_c^4\right)u^2 + q_c^2\left(\frac{\partial u}{\partial x}\right)^2 - \frac{1}{2}\left(\frac{\partial^2 u}{\partial x^2}\right)^2 + \frac{\partial u}{\partial x}\frac{\partial^3 u}{\partial x^3} - \frac{1}{4}b_3u^4 + \frac{1}{6}b_5u^6. \tag{1.6}$$

Localized states correspond to orbits of this system that are homoclinic (i.e., a path in phase space connecting an equilibrium to itself, that lies in the intersection of the stable and unstable manifolds) to the zero solution $u = 0$. Such orbits must lie in the surface $H = 0$ [16, 17, 21].

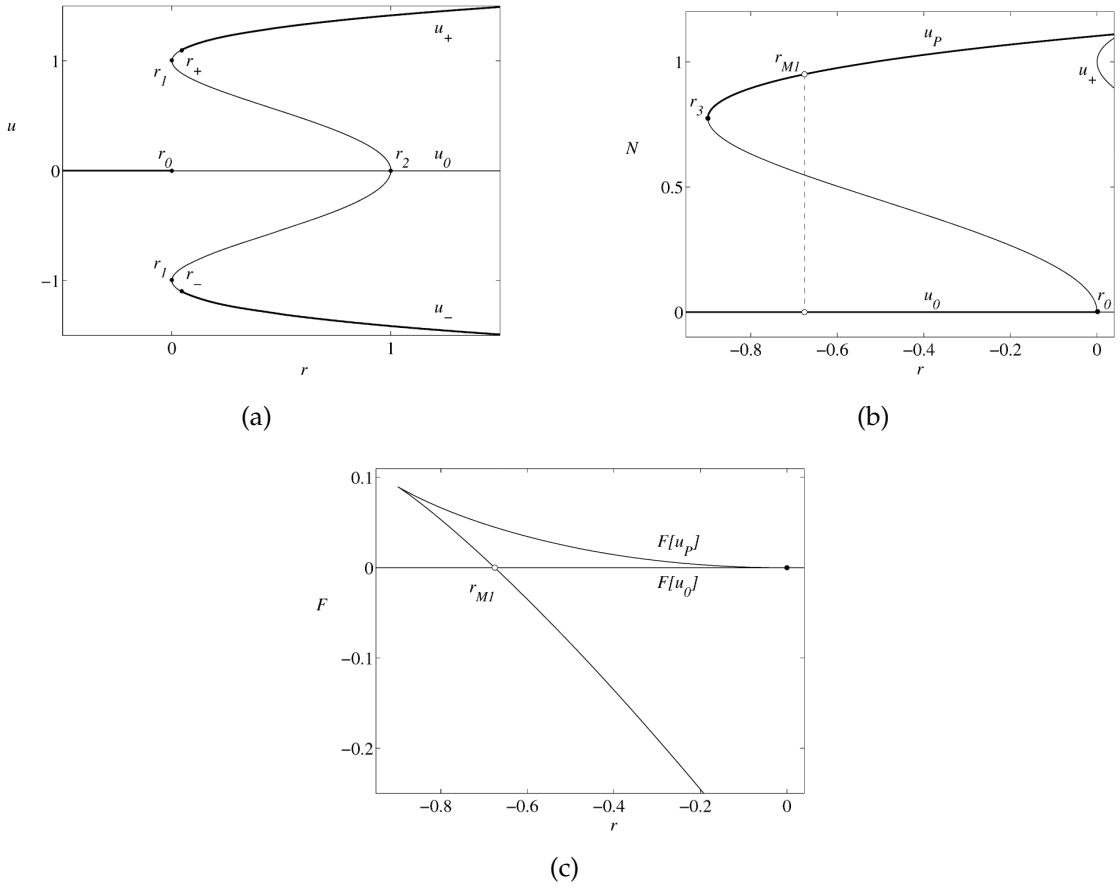

Figure 1.4. (a) The uniform solution u_0 and $u_\pm$ as a function of r. Labelled bifurcations are $r_0 = 0$, $r_1 = 0$, $r_2 = 1$, $r_\simeq = 0.04289$. The thick lines indicate stability. (b) Bifurcation diagrams are showing the norm $N \equiv \left(L_c^{-1}\int_0^{L_c} u^2 dx\right)^{\frac{1}{2}}$ of pattern states u_P with wave length L_c as a function of r. The location of saddle-node is $r_3 \simeq -0.8991$. (c) Energy F of the uniform and periodic branches as a function of r. The Maxwell point $r_{M1} = -0.6752$. Reprinted from Burke *et al.*[21].

The linear stability of the stationary solution $u_s(x)$ of period L can be determined by writing

$$u(x,t) = u_s(x) + \epsilon\tilde{u}(x)e^{\lambda t}. \tag{1.7}$$

By substituting (1.7) into (1.1) and linearizing around $\epsilon = 0$, we obtain the eigenvalue problem

$$\lambda\tilde{u}(x) = \mathcal{L}\tilde{u}(x), \tag{1.8}$$

where

$$\mathcal{L} := r - \left(\frac{\partial^2}{\partial x^2} + q_c^2\right)^2 + 3b_3u_s^2(x) - 5b_5u_s^4(x), \tag{1.9}$$

which is the linear differential operator.

The Swift-Hohenberg equation (1.1) has the uniform solution given by

$$0 = (r - q_c)u + b_3u^3 - b_5u^5, \tag{1.10}$$

that can be solved to yield

$$u_0 = 0, \quad u_\pm = \left(\frac{1}{b_5}\left[b_3 \pm \sqrt{b_3^2 + 4b_5\left(r - q_c^2\right)}\right]\right)^{\frac{1}{2}}, \tag{1.11}$$

and are shown in Fig. 1.4(a) [21].To determine the stability of the uniform solutions, one has $\tilde{u}(x) = e^{ikx}$, where k is the wave number of the perturbation, from which we obtain the dispersion relation

$$\lambda(k) = r - q_c^4 - k^4 + 2k^2q_c^2 + 3b_3u^2 - 5b_5u^4. \tag{1.12}$$

The uniform solution u_0 changes stability with respect to spatially periodic perturbations with wave length $L_c = 2\pi/q_c$ and creates a branch of periodic solution/pattern state u_P, which bifurcates from r_0. We also can obtain the saddle-

node bifurcation in the uniform solution at point r_1. The details of the stability changes in the uniform solutions are depicted in Fig. 1.4(a).

The branch of the spatially periodic solution is computed by using numerical continuation [37]. The results are summarized in Fig. 1.4(b). We have Maxwell point r_{M1}, which is when the periodic solution has the same energy with the zero state u_0. We have Maxwell point r_{M1}, which has zero wave velocity and a stationary front exists, at which the trivial and patterned solutions are equally energetically favoured and stationary fronts connecting the two states can exist [35]. Note that we have bistability between the periodic solution u_P and uniform solution u_0 in the interval $r_3 < r < r_0$.

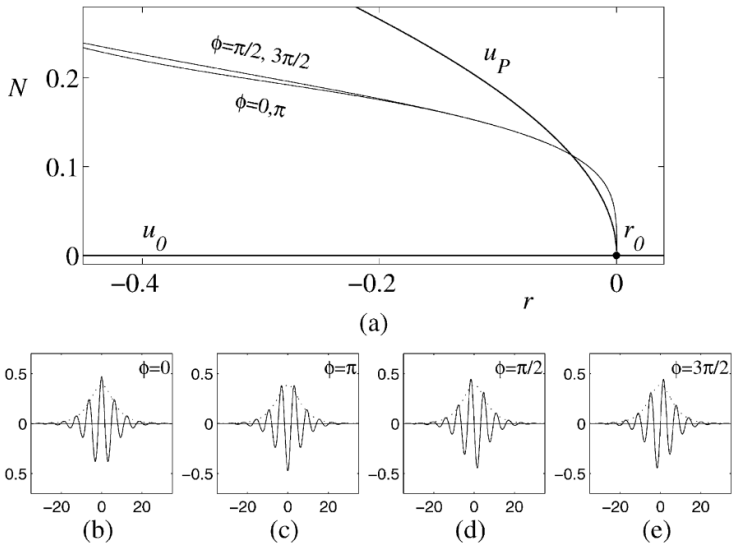

Figure 1.5. Bifurcation diagrams are showing the branches of the localized solutions around r_0. The smaller panels show localized solutions for four different phase-shifts. The amplitude that we obtained from (1.18) is also shown. Reprinted from Burke *et al.*[21].

Localized solutions also bifurcate around r_0. This state can be obtained by performing an asymptotic expansion analysis, see Burke *et al.* [21]. Defining the small parameter ϵ, write $r = -\epsilon^2\mu_2$, $\mu_2 > 0$, and looking for stationary solutions from (1.1) in the form

$$u(x) = \epsilon\left(A(X)e^{iq_c x} + \text{c.c.}\right) + O(\epsilon^2). \tag{1.13}$$

where $X \equiv \epsilon x$ is a large scale over which the amplitude of the pattern changes. Thus, we have

$$4q_c^2 A_{XX} = \mu_2 A - 3b_3 A|A|^2 + O(\epsilon). \tag{1.14}$$

Since $b_3 > 0$, the bifurcation at the origin is *subcritical*. The simplest nontrivial solution is

$$A(X) = \left(\frac{\mu_2}{3b_3}\right)^{\frac{1}{2}} e^{i\phi} + O(\epsilon), \tag{1.15}$$

corresponding to spatially periodic states with period L_c near r_0. Thus, we have

$$u_P(x) = 2\left(\frac{-r}{b_3}\right)^{\frac{1}{2}} \cos\left(q_c x + \phi\right) + O(r). \tag{1.16}$$

The other solution can be found, which corresponds to the localized solution with $A \to 0$ as $X \to \pm\infty$, to be

$$A(X) = \left(\frac{2\mu_2}{3b_3}\right)^{\frac{1}{2}} \operatorname{sech}\left(\frac{X\sqrt{\mu_2}}{2q_c}\right) e^{i\phi} + O(\epsilon), \tag{1.17}$$

which yields

$$u_l(x) = 2\left(\frac{-2r}{3b_3}\right)^{1/2} \operatorname{sech}\left(\frac{x\sqrt{r}}{2q_c}\right) \cos\left(q_c x + \phi\right) + O(r). \tag{1.18}$$

The spontaneous pattern formation also can be studied around the onset of instability by performing asymptotic expansion analysis, see Dean *et al.* [35]. By defining small parameter $0 < \epsilon \ll 1$ and writing $X = \epsilon^2 x$, $T = \epsilon^4 t$, where the two spatial variables x and X are treated as independent in the subsequent expansion, we look for solutions in the form

$$u(x,t) = U(x, X, T). \tag{1.19}$$

We need to balance of nonlinear terms and slow-scale derivatives. The parameters are then scaled as $r = \epsilon^4 r_4, b3 = \epsilon^2 s_2$. We also set $q_c = 1$ and $b_5 = 1$ to make the analysis is simpler. We are interested in the bistability given by a subcritical pattern-forming bifurcation, so choose $b_3 > 0$. Equation (1.1) becomes

$$\epsilon^4 \frac{\partial U}{\partial T} = \epsilon^4 r_4 U - \left(1 + \frac{\partial^2}{\partial x^2} + 2\epsilon^2 \frac{\partial^2}{\partial x \partial X} + \epsilon^4 \frac{\partial^2}{\partial X^2}\right) U + \epsilon^4 s_2 U^3 - \epsilon^4 U^5. \tag{1.20}$$

A formal asymptotic analysis may now be carried out by expanding U in powers of ϵ^2 as

$$U(x, X, T) = \sum_{n=0}^{N-1} \epsilon^{2n} U_n(x, X, T) + R_N(x, X, T). \tag{1.21}$$

We truncated the expansion, retaining only those terms up to $O(\epsilon^{2N-2})$.

The leading-order solution to Eq. (1.20) is

$$U_0(x, X, T) = A_0(X, T) e^{ix} + \bar{A}_0(X, T) e^{-ix}, \tag{1.22}$$

where the bar denotes the complex conjugate. The pattern thus consists of slowly modulated spatial oscillations. The envelope A_0 is then determined by a solvability condition arising at $O(\epsilon^4)$, in the form of the Ginzburg-Landau equation

$$\frac{\partial A_0}{\partial T} = r_4 A_0 + 4 \frac{\partial^2 A_0}{\partial X^2} + 3 s_2 |A_0|^2 A_0 - 10 |A_0|^4 A_0. \tag{1.23}$$

A steady solution in the form of a front connecting the zero and non-zero states can be found at

$$r_4 = r_{Ma} := -\frac{27}{160} s_2^2, \tag{1.24}$$

given by

$$A_0(X, T) = A_f(X) e^{i\phi}, \tag{1.25}$$

where

$$A_f(X) = \left(\frac{3}{10}\right)^{1/4} \frac{\sqrt{\mu}}{1+e^{\mu X}}, \tag{1.26}$$

with ϕ an arbitrary real constant and $\mu = \sqrt{-r_{Ma}}$. Thus, $\epsilon^4 r_{Ma}$ provides a first approximation to the Maxwell point r_{M1}, see Fig. 1.4. We can consider Eq. (1.26) as a travelling wave with zero wavespeed. In fact, a stationary front solution to Eq. (1.23) can only exist at $r_4 = r_{Ma}$. For $r_4 > r_{Ma}$, the equivalent solutions is a travelling wave in which the non-zero solution is more "dominant" than the zero solution, while for $r_4 < r_{Ma}$ the converse occurs.

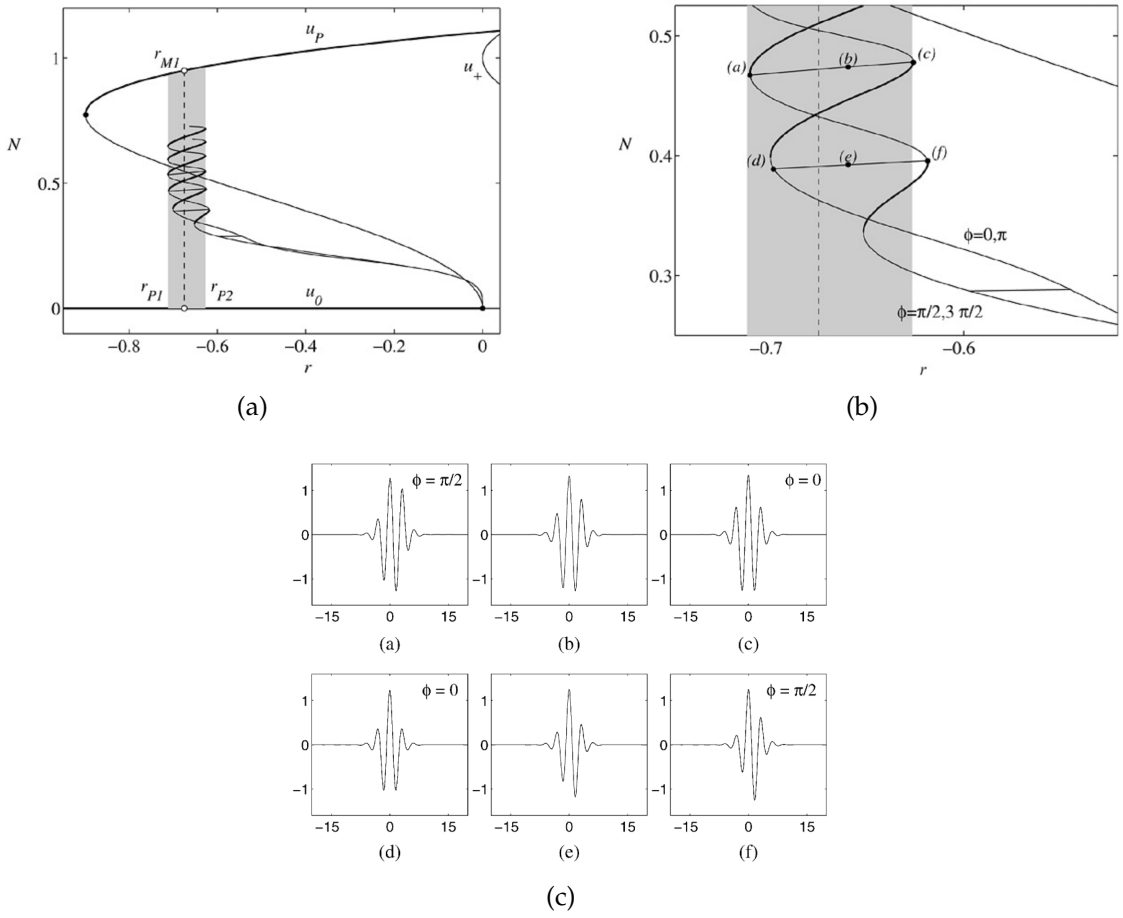

Figure 1.6. (a), (b) Bifurcation diagrams of the uniform and periodic solutions, showing two homoclinic snaking. The pinning regime (shaded) is in between $r_{P1} \simeq -0.7126$ and $r_{P2} \simeq -0.6267$. The two snaking solutions are connected by secondary branches of localized but asymmetric solutions. Thick lines indicate the stable solutions. The dashed line represents the location of the Maxwell point r_{M1} between the uniform and the periodic solutions. (b) Closeup showing the 'rungs' connecting the snaking branches. (c) Sample profiles $u_l(x)$ at the saddle-nodes in panel (b). Reprinted from Burke *et al.* [21].

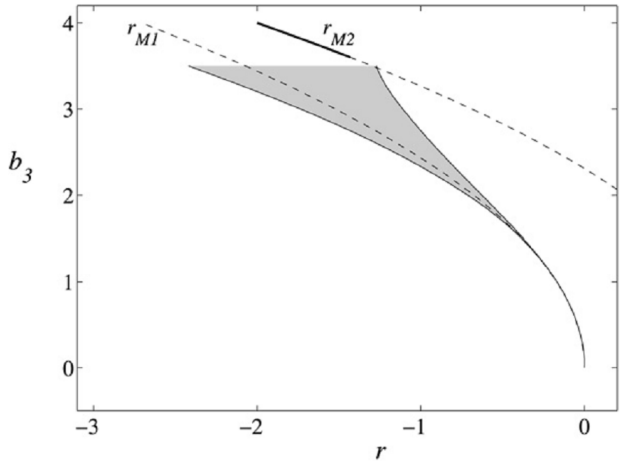

Figure 1.7. The pinning regimes (shaded) of the heteroclinic to the trivial u_0 state. This region located between r_{P1} and r_{P2} is created in a codimension-2 bifurcation at $(r, b_3) \simeq (0, 0)$. Dashed lines correspond to the Maxwell points. Reprinted from Burke *et al.* [21].

Figure 1.5 shows the bifurcation diagrams and their localized solutions around r_0, which are obtained from the asymptotic analysis (1.18). It is also shown that the localized solution has two phase-shifts, with $\phi = 0$, $\phi = \pi$, $\phi = \pi/2$, and $\phi = 3\pi/2$, where $\phi = 0$ and $\phi = \pi$ are antisymmetric with respect to each other and also for $\phi = \pi/2$ and $\phi = 3\pi/2$.

By using (1.18) as our initial condition and performing numerical continuation as a function of r for equation (1.1) in each branches, we will obtain the snaking-like structure in the bifurcation diagram as shown in Fig. 1.6. The results show that the snaking is present in the pinning region, which is bounded by the saddle-node bifurcations. As the norm increases, the periodic state invades the background (trivial) state, namely u_0. In the pinning region, the localized solution has infinite multiplicity due to the unbounded domain.

Figure 1.7 shows the existence of the heteroclinic connection, which is a path in phase space which connects two different equilibrium points, to the trivial state u_0. The heteroclinic connection appears when b_3 is being varied which is around $b_3 \simeq 3.521$. Above these values, the snaking collapses and become straight line, which is the Maxwell point. The Maxwell point is when uniform state u_+ and

trivial states u_0 have the same energy, i.e.,

$$r_{M2} = q_c^4 - \frac{3b_3^2}{16b_5}.$$

1.5 Discrete optical cavity equation

The study of homoclinic snaking of localized structures also emerged in the field of optics, particularly in optical cavities. An optical cavity, resonating cavity or optical resonator is an arrangement of mirrors that forms a standing wave cavity resonator for light waves. Optical cavities are a major component of lasers, surrounding the gain medium and providing feedback of the laser light. Light confined in the cavity reflects multiple times producing standing waves. Cavity solitons are self-localized states of light appearing in the transverse plane of a cavity as bright spots sitting on a dark background. Experimentally, they can be characterized by the following properties: (1) self-localized states, independent of the system boundaries whose shape and size is fixed by the system parameters and do not depend on the excitation that gave birth to them; (2) existing in several (ideally arbitrary) transverse locations of the cavity and can be independently manipulated (written, erased,); (3) can be "moved" or set into motion [7]. Yulin *et al.* [96, 97] reported the existence of homoclinic snaking in discrete model for optical cavity with an imposed periodic structure and saturable nonlinearity. The model of the discrete optical cavity equation is given by

$$i\frac{\partial A_n}{\partial t} + \delta A_n + \alpha\frac{|A_n|^2}{1+|A_n|^2} + c\,(A_{n+1} + A_{n-1} - 2A_n) = Pe^{iqn}, \quad -\infty < n < \infty, \tag{1.27}$$

which is a one-dimensional lattice equation for a complex field $A_n \in \mathbb{C}$.

This study generalises the earlier research on optical cavity equation, which has been conducted by Egorov *et al.* [40, 43, 74]. The variable A_n corresponds

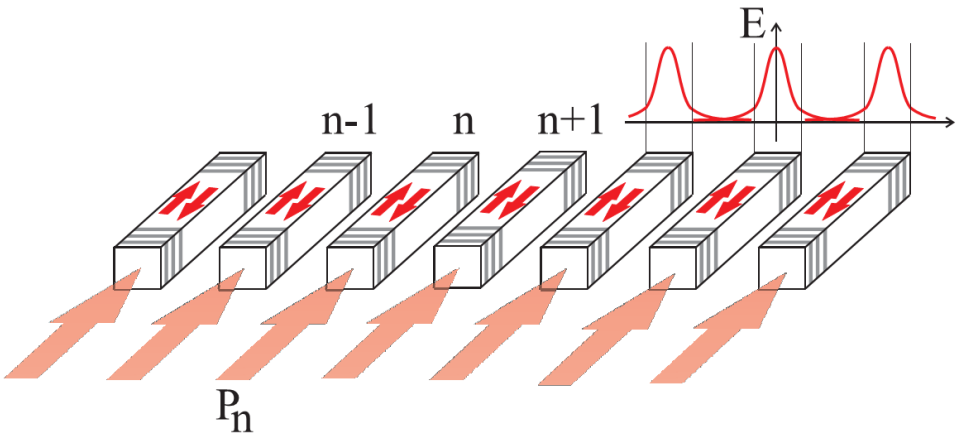

Figure 1.8. Sketch of a periodic optical structure composed of identical resonators pumped by coherent light, which is described by equation (1.27). Reprinted from Yulin *et al.* [97].

to the amplitude of the magnetic field inside the nth identical resonator in a one-dimensional array. The parameter $c \geq 0$ indicates the coefficient of coupling between the neighboring oscillators. The limit $c \to 0$ corresponds to the anti-continuum limit where the oscillators are independent of each other and $c \to \infty$ represents the continuum limit. The parameter $Re(\delta)$ represents detuning of the pump frequency from the resonant frequency of the oscillators. The parameter α corresponds to strength of the Kerr effect of intensity-dependent refractive index, where the physical realistic effect of the saturation for large intensity has been included. One has defocusing ($Re(\alpha) < 0$), purely dissipative ($Re(\alpha) = 0$), and focusing ($Re(\alpha) > 0$) nonlinearity. The parameter P represents the amplitude of an applied optical pump field whose phase is a function in space with period $2\pi/q$. In the case where $q = 0$, where there is no phase gradient of the pump [97, 98].

The whole qualitative description of the snaking bifurcation that found in equation (1.27) is presented in Table 1.1. Examples for all of the cases are depicted in Figs. 1.9–1.15.

Figure 1.9 shows a bifurcation diagram of stationary solutions, i.e., uniform and localized solutions for $\alpha = 10$ and $\delta = -9.2$ as a function of pump field P. It shows that the bifurcation diagram has stable and unstable bright solitons.

Parameters				Description	Example
α	c	$Re(\delta)$	$Im(\delta)$		
>0	$\to\infty$	$-\alpha<\delta<0$	0	bright solitons & multipulses	Fig. 1.9
>0	$\to\infty$	$-\alpha<Re(\delta)<0$	>0	thin snakes of bright and grey solitons for large enough $Im(\delta)$	Fig. 1.10
>0	finite	$-\alpha<Re(\delta)<0$	>0	wide snakes of bright and grey solitons	Fig. 1.11
>0	finite or $\to\infty$	$-\frac{9\alpha}{8}<Re(\delta)<0$	≥ 0	snakes of bright and grey solitons	Fig. 1.12
<0	$\to\infty$	$0<Re(\delta)<\frac{9\alpha}{8}$	0	topological solitons	Fig. 1.13
<0	finite or $\to\infty$	$0<Re(\delta)<\frac{9\alpha}{8}$	>0	wide snakes of bright and grey solitons	Fig. 1.14
imag.	$\to\infty$	$Re(\delta)<0$	>0	wide and thin snakes of bright and grey solitons	Fig. 1.15

Table 1.1: Qualitative description of kinds of snaking bifurcation curves found in equation (1.27). The limit $c\to\infty$ represents the continuum limit, whereas finite c corresponds to a discrete lattice. Reprinted from Yulin *et al.* [97].

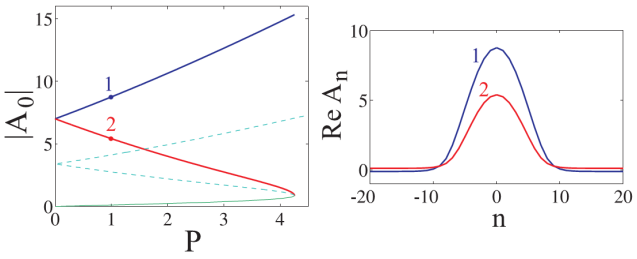

Figure 1.9. Bifurcation diagram for $\alpha=10$ and $\delta=-9.2$ and its corresponding solution profiles at $P=1$. The blue and red solid lines indicate stable and unstable homoclinic solution, respectively. The green solid and dashed lines indicate stable and unstable uniform solution, respectively. Reprinted from Yulin *et al.* [97].

Figure 1.10 shows a bifurcation diagram of stationary solutions for $\alpha=10$, $\delta=-9.2+1i$, and $c=12$ as a function of pump field P. It shows that a snake appears when δ is complex. We have thin snake of bright and grey solitons when $Im(\delta)$ is large enough. For the sake of convenience, we show the snakes in the figures by

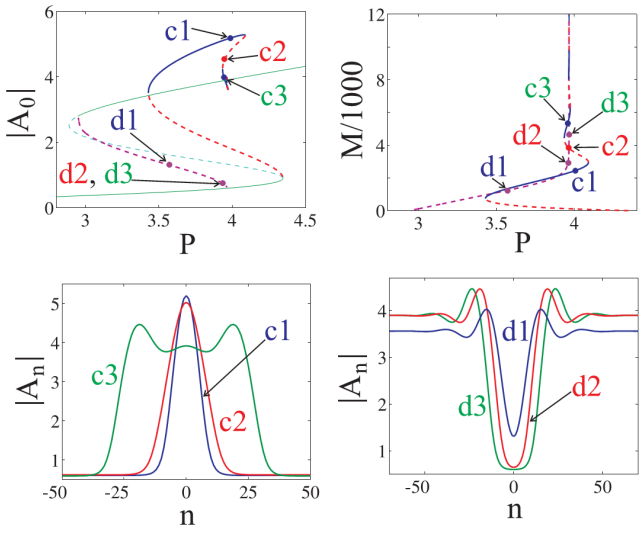

Figure 1.10. Bifurcation diagram for $\alpha = 10$, $\delta = -9.2 + 1i$, and $c = 12$ and its corresponding solution profiles at points $c1$, $c2$, $c3$, $d1$, $d2$, and $d3$. The thinner solid green and dashed cyan lines show the stable and unstable uniform solutions, respectively. The solid blue and dashed red lines correspond to stable and unstable bright solitons, respectively, whereas dashed magenta lines correspond to the grey soliton, which is always unstable. Reprinted from Yulin *et al.* [97].

the norm [97, 98]

$$M = \sum_n (|A_n - A_\infty|). \tag{1.28}$$

Figure 1.11 shows a bifurcation diagram of stationary solutions for $\alpha = 10$ and $c = 0.5$ with $\delta = -9.2 + 1i$ and $\delta = -9.2 + 0.7i$ as a function of pump field P. It shows that a wide snake of bright and grey solitons appear when we consider small c coupling.

Figure 1.12 shows a bifurcation diagram of stationary solutions for $\alpha = 10$ $\delta = -10.3$, and $c = 25$ as a function of pump field P. It shows that a snake of bright and grey solitons appear in this parameter values.

Figure 1.13 shows a bifurcation diagram of stationary solutions for $\alpha = 10$ $\delta = -10.3$, and $c = 25$ as a function of pump field P. It shows that the snake of topological solitons (grey solitons for $P > 0$) appears which can never be temporally stable.

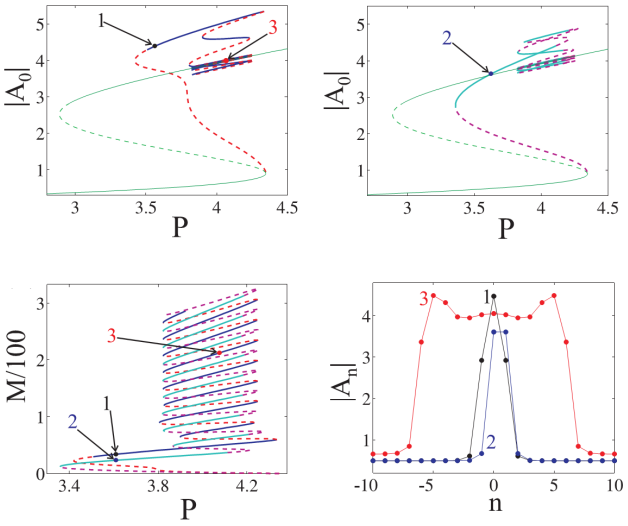

(a)

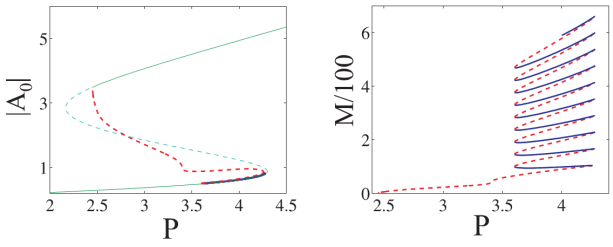

(b)

Figure 1.11. (a) Similiar to the bright solitons in Fig. 1.10 but in the discrete case with $c = 0.5$. (b) Similiar to panel (a) but $\delta = -9.2 + 0.7i$. Solid lines (blue and cyan) indicate stable parts of the bifurcation diagrams and dashed lines (red and magenta) represent unstable parts. Reprinted from Yulin *et al.* [97].

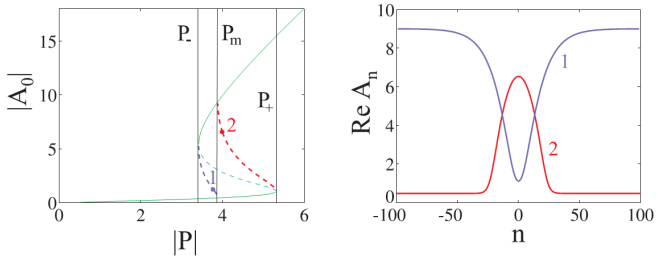

Figure 1.12. Similiar to the Fig. 1.9 but for $\alpha = 10$, $\delta = -10.3$, and $c = 25$ and its corresponding solutions at points 1 and 2 for $P = 3.8$ and 4, respectively. Reprinted from Yulin *et al.* [97].

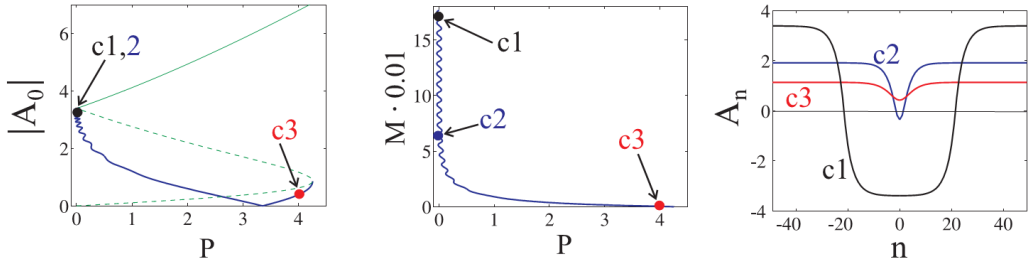

Figure 1.13. Bifurcation diagrams for the "topological" onsite conservative solitons (grey solitons for $P > 0$) as a function of the pump P for $\delta = 9.2$, $\alpha = -10$, and $c = 15$. The thick blue line corresponds to the solitons, and the thin green line shows the uniform solutions, with dashed line representing instability. Reprinted from Yulin *et al.* [97].

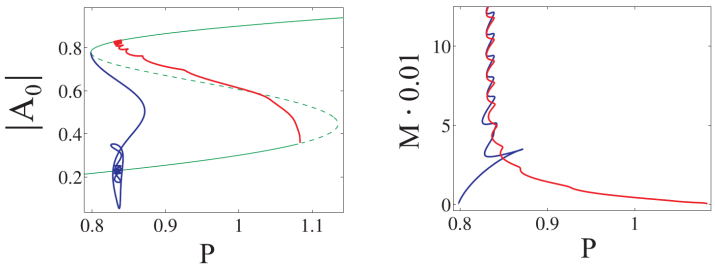

(a)

Figure 1.14. Bifurcation diagrams of bright (red line) and grey (blue line) onsite solitons as the pump P varies for $\delta = 4 + 1i$, $\alpha = -10$, and $c = 1$. Reprinted from Yulin *et al.* [97].

Figure 1.14 shows a bifurcation diagram of stationary solutions for $\delta = 4 + 1i$, $\alpha = -10$, and $c = 1$ as a function of pump field P. It shows that a snake of bright and grey solitons appear in this parameter value.

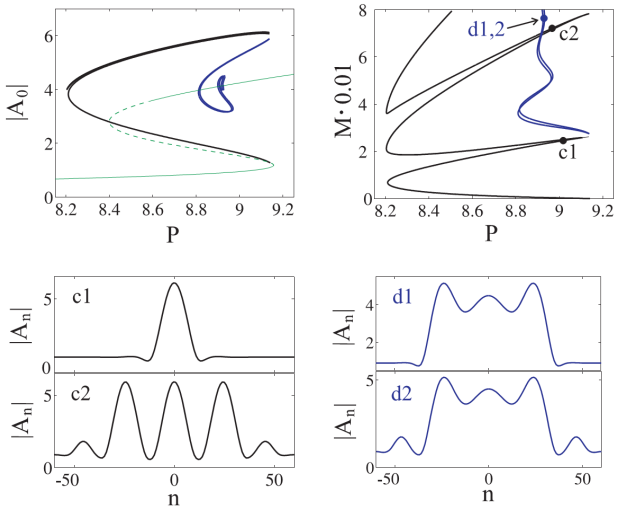

Figure 1.15. Similar to Fig. 1.14 but for $\delta = 1.05 + 17i$, $\alpha = -16i$, and $c = 15$. Reprinted from Yulin *et al.* [97].

Figure 1.15 shows a bifurcation diagram of stationary solutions for $\delta = 1.05 + 17i$, $\alpha = -16i$, and $c = 15$ as a function of pump field P. We have wide snakes of bright and grey solitons when c is large enough and thin snakes when c is small.

1.6 Discrete Allen-Cahn equation

Homoclinic snaking in 1D and 2D Allen-Cahn equation with cubic-quintic nonlinearity was conducted by Taylor and Dawes [86]. They investigated the snaking and isolas mechanism in the system.

One-dimensional lattice

Taylor and Dawes [86] considered the following equation on the integer lattice $\mathbb{Z}$:

$$\dot{u}_n = \mu u_n + C(u_{n+1} + u_{n-1} - 2u_n) + 2u_n^3 - u_n^5, \tag{1.29}$$

where u_n is a scalar variable for each lattice site, C is the strength of linear coupling between adjecent sites, and $-1 < \mu < 0$ is the bifurcation parameter. The addition of a time derivative term is to indicate the (in)stability of the equilibrium states. One can write equation (1.29) as $\dot{u}_n = -\partial F/\partial u_n$, where F is a Lyapunov functional, which we refer to as an energy, given by

$$F = \sum_n -\frac{1}{2}\mu u_n^2 + \frac{1}{2}C(u_{n+1} - u_n)^2 - \frac{1}{2}u_n^4 + \frac{1}{6}u_n^6. \tag{1.30}$$

Thus $\dot{F} \leq 0$, so that every solution of equation (1.29) flows down gradients of the potential toward an equilibrium solution and every stable equilibrium states is local minimum of the potential. No periodic dynamics or complex dynamics are therefore possible [86].

Equation (1.29) has five uniform states, i.e., one trivial or zero state $u_n = 0$ and four uniform states $u_n = \pm u_\pm$, where $u_\pm = 1 \pm \sqrt{1+\mu}$. The zero state $u_n = 0$ is linearly stable for $\mu < 0$ and unstable for $\mu > 0$. The lower uniform state $u_- = \sqrt{1-\sqrt{1+\mu}}$ exists in $-1 < \mu < 0$ and is always unstable. Meanwhile, the upper uniform state $u_+ = \sqrt{1+\sqrt{1+\mu}}$ exists in $\mu > -1$ and is always stable. One also has saddle-node bifurcations at $\mu = -1$.

Each node potential for the uniform state $u_n = u_*$ is given by $F(u_*) = -\frac{1}{2}\mu u_*^2 - \frac{1}{4}u_*^4 + \frac{1}{6}u_*$. Thus the system acts to minimize the total potential. The zero state has zero potential and the upper state u_+ depends only on μ. By considering the double root of $F(u) = 0$, one find that the upper state u_+ has zero potential at $\mu = \mu_{mx} = -3/4$, i.e., *Maxwell point*. When $\mu > \mu_{mx}$ the upper state is energetically more favourable and when $\mu < \mu_{mx}$ the zero state is energetically more favourable. By using numerical continuation program AUTO [38] and using periodic and

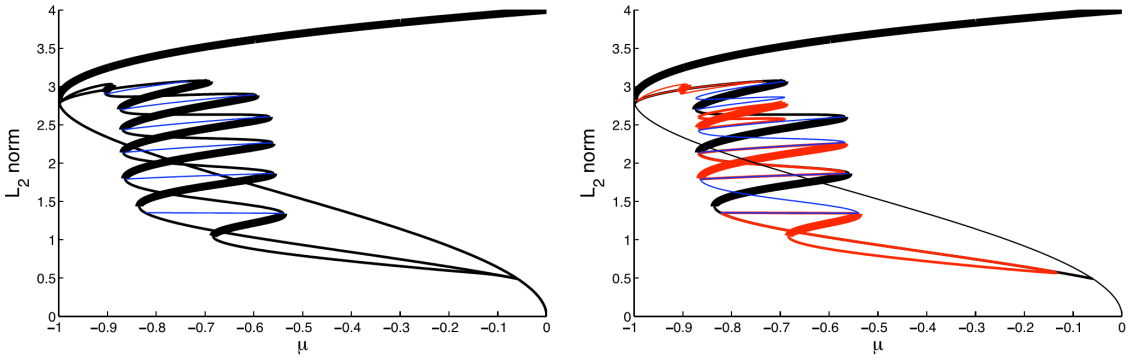

Figure 1.16. Left bifurcation diagram in one dimension for an array of $N = 8$ nodes with periodic boundary condition and $C = 0.2$. Thick and thin black lines represent stable and unstable solutions, respectively. The thin blue horizontal lines are asymmetric "ladder" solutions. Right bifurcation diagram with Neumann boundary condition. The red curves are isolas, and the blue curves terminate at branch points on the black snaking curve. Reprinted from Taylor and Dawes [86].

Neumann boundary condition, Taylor and Dawes obtained bifurcation diagrams in Fig. 1.16. The result resembles the homoclinic snaking for the Swift-Hohenberg equation in a finite domain with branches of the localized solutions bifurcating from the uniform solution around $\mu \approx -0.07$ and turning around in a succession of

fold bifurcations to form two intertwined snakes of the localized structures, one of site-centred and one of bond-centred solutions, before reconnecting to the uniform branch at $\mu = -0.98$.

Figure 1.17 shows the solution profiles in the right hand saddle-node bifurcation points for periodic boundary conditions. The upper three solutions are site-centred and hence are reflection symmetry about the lattice point $n = 4$. The lower three plots are bond-centred and are reflections-symmetric about midpoint between $n = 4$ and 5.

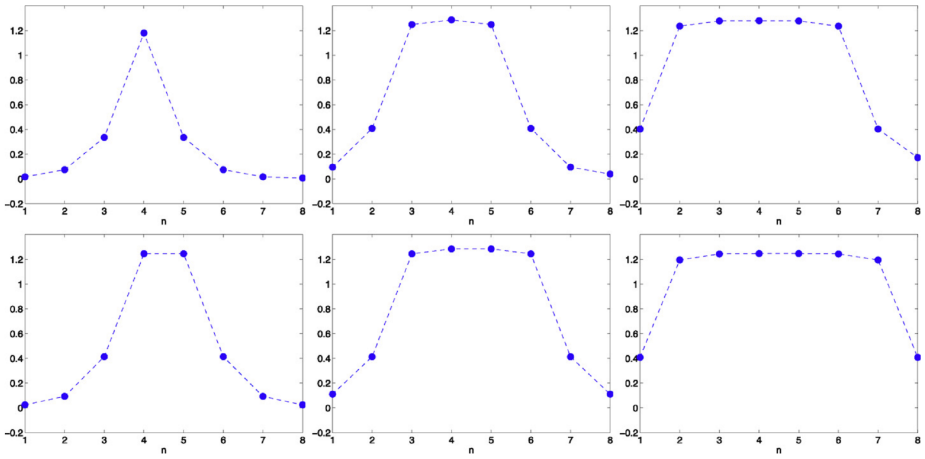

Figure 1.17. Equilibrium solution profiles of equation (1.29) on 1D lattices with $N = 8$ using periodic boundary condition taking $C = 0.2$. Profiles correspond to the right hand saddle-node bifurcation points of Fig. 1.16. Reprinted from Taylor and Dawes [86].

Isola solutions also may appear in the bifurcation diagrams by changing from the periodic boundary condition into Neumann boundary condition as shown in Fig. 1.16, which appear due to the attachment and detachment process. The pinning region for 1-cell, 2-cell, and 3-cell localized solution is depicted in Fig. 1.18. The front solution is indicated by the blue curves which extend up to $C = 1$: on an infinite lattice the edges of the snaking regime asymptote to these curves as the width of the localized state increases. The vertical dashed line is the Maxwell point $\mu = -3/4$. The result is for $N = 100$.

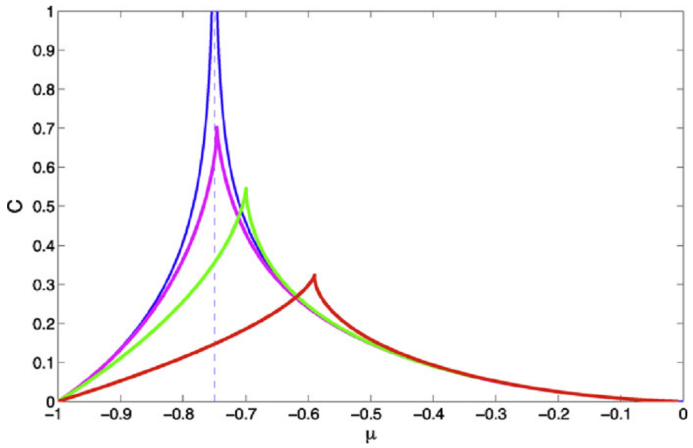

Figure 1.18. Region of existence of localized states in the (μ, C) plane; 1-cell localized states (red, peak at $C \approx 0.33$), 2-cell (green, peak at $C \approx 0.55$), and 3-cell (magenta, peak at $C \approx= 0.7$). Reprinted from Taylor and Dawes [86].

Two-dimensional lattice

The two dimensional interpretation of equation (1.29) has two nearest-neighbor difference operators, i.e.,

$$\begin{aligned} \Delta^{+} u_{n,m} &\equiv u_{n+1,m} + u_{n-1,m} + u_{n,m+1} + u_{n,m+1} - 4u_{n,m}, \\ \Delta^{\times} u_{n,m} &\equiv u_{n+1,m+1} + u_{n-1,m-1} + u_{n-1,m+1} + u_{n+1,m+1} - 4u_{n,m}. \end{aligned} \tag{1.31}$$

Thus, the 2D discrete Allen-Cahn equation is given by

$$\dot{u}_{n,m} = \mu u_{n,m} + C^{+}\Delta^{+} u_{n,m} + C^{\times}\Delta^{\times} u_{n,m} + 2u_{n,m}^{3} - u_{n,m}^{5}, \tag{1.32}$$

where there are two coupling parameters C^{+} and $C^{\times}$, the coefficients of all nearest-neighbor coupling. In [86], Taylor and Dawes only consider $C^{\times} = 0$, periodic boundary condition, and bond-centred solution to simplify the discussion. They also introduced the scaled version of the $\mathbb{L}_2$ norm to plot the bifurcation diagram, which is given by

$$M = \left(\frac{\sum_{n,m} u_{n,m}^{2}}{1 + \sqrt{1+\mu}} \right)^{\frac{1}{2}}. \tag{1.33}$$

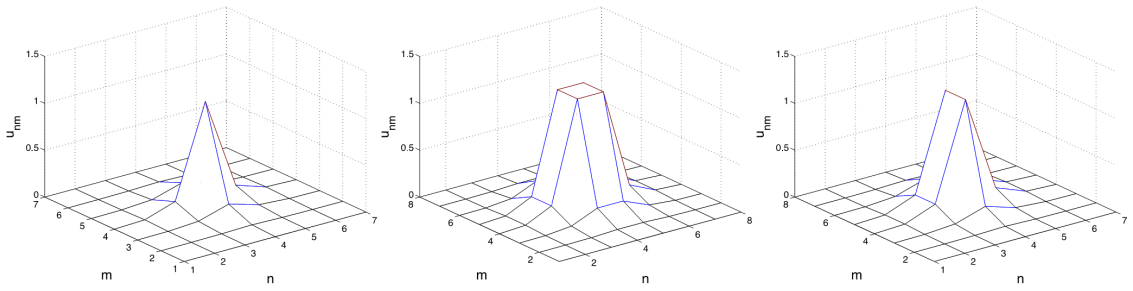

Figure 1.19. Three typical localized solutions to equation (1.32) with $C^+ = 0.1$, $C^\times = 0$, and $\mu = -0.6$. Three solutions are respectively site-centred, bond-centred, and hybrid. Reprinted from Taylor and Dawes [86].

As in the 1D case, by performing numerical continuation in AUTO, using periodic boundary condition, and using bond-centred solution in Fig. 1.19 as an initial condition, one can obtain the snaking solution as shown in Fig. 1.20. The first thirty encountered saddle-node bifurcations from Fig. 1.20 is shown in Fig. 1.21.

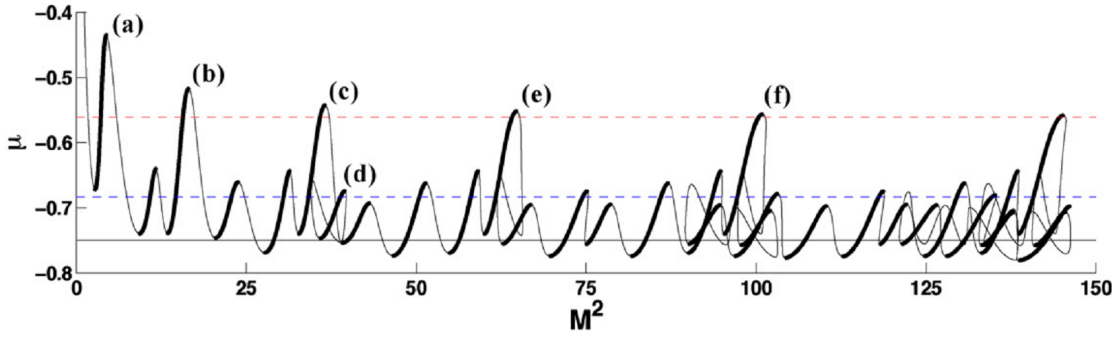

Figure 1.20. Bifurcation diagram of the bond-centred solutions of equation (1.32) with $C^+ = 0.2$ and $C^\times = 0$. The switchbacks occur near $M^2 = 36$, 64, 100, and 144. Solid black lines indicate the Maxwell point $\mu = -3/4$. Red horizontal dashed lines at $\mu \approx -0.56076$ indicates the asymptotic location of saddle-node bifurcations on the 1D snake with coupling strength $C = C^+ + 2C^\times$, far up the 1D snake. Blue horizontal dashed lines at $\mu \approx -0.68309$ indicate the asymptotic location of saddle-node bifurcations on the 1D snake with coupling strength $C = 2C^+ + C^\times$. Thin and thick lines indicate unstable and stable solutions, respectively. Reprinted from Taylor and Dawes [86].

The evolution of bond-centred localised states as we move up the snaking curve is shown in Fig. 1.21. Starting from indicated point (a) in which four cells are close to “upper state" u_+ and the rest are near zero state u_0, new “upper" state u_+ cells are added to the solution profile starting in the center of the faces, and

then progressing outwards towards the corners until the profile is square, at which point the sequence repeats itself [86].

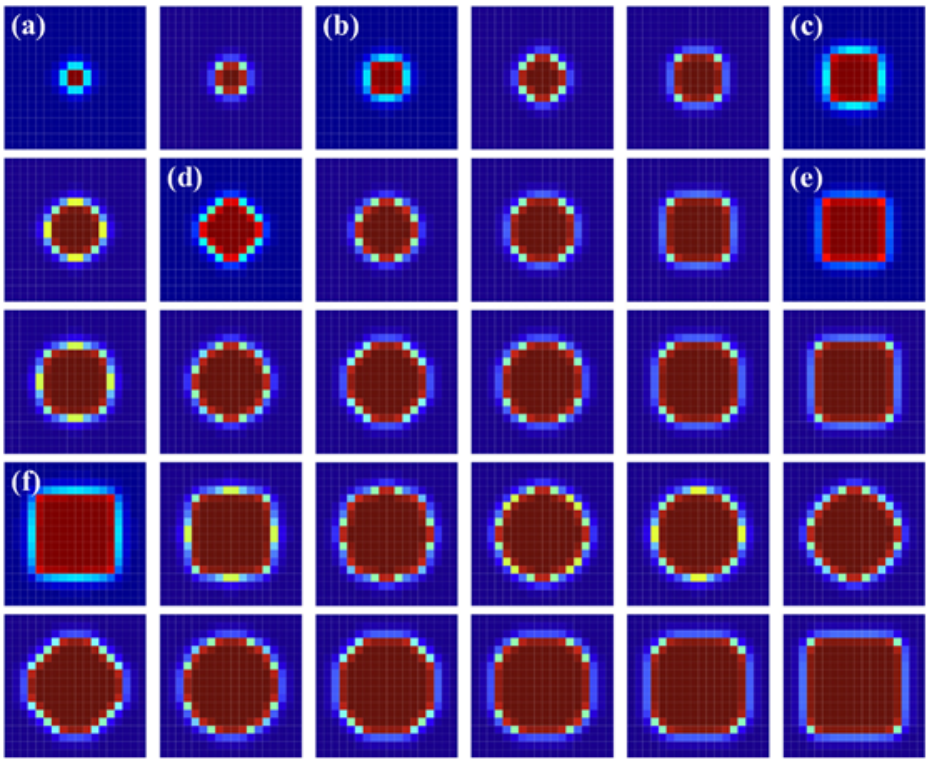

Figure 1.21. The first 30 bond-centred localized states encountered at saddle-node bifurcation points corresponding to local maxima of μ, moving along the snaking curve with M increasing, for fixed $C^+ = 0.2$. Labels (a)-(f) correspond to the labelled saddle-node bifrucations on the snake indicated in Fig. 1.20. Reprinted from Taylor and Dawes [86].

1.7 Numerical continuation

In this thesis, we seek for time-independent solutions by using a Newton-Raphson method to obtain their bifurcation diagrams.

Consider the equation

$$\mathbf{G}(\mathbf{u},\lambda) = 0, \quad \mathbf{u},\ \mathbf{G}(\cdot,\cdot) \in \mathbb{R}^n, \quad \lambda \in \mathbb{R}. \tag{1.34}$$

Let

$$\mathbf{x} \equiv (\mathbf{u},\lambda). \tag{1.35}$$

Then Eq. (1.34) can be written as

$$\mathbf{G}(\mathbf{x}) = \mathbf{0}, \quad \mathbf{G} : \mathbb{R}^{n+1} \to \mathbb{R}^n. \tag{1.36}$$

Suppose we have a solution $\mathbf{x}_0 = (\mathbf{u}_0, \lambda_0)$ of $\mathbf{G}(\mathbf{x}) = 0$. $\mathbf{x}_0$ is called a regular solution if

$$\text{Rank}\,(\mathbf{G}_x(\mathbf{x}_0)) = n.$$

In this case, the Implicit Function Theorem guarantees the existence of solution $\mathbf{u}(\lambda)$ near λ_0 and natural parameter continuation as a simple adaptation of the iterative solver to a parametrized problem can be employed to find a solution curve, i.e., the solution at λ_0 is used as the initial guess for the solution at $(\lambda_0 + \Delta\lambda)$ with $\Delta\lambda$ sufficiently small.

However, as the bifurcation parameter λ is being varied, there can be turning points. At the special points, the corresponding solutions are no longer regular, i.e., the Jacobian has at least a zero eigenvalue. We use a pseudo-arclength method to continue the computations past them and avoid the zero eigenvalue in Jacobian matrix of the system [57].

The method is based on the observation that the "ideal" parameterization of a curve is arclength. Pseudo-arclength is an approximation of the arclength in the tangent space of the curve. The resulting modified natural continuation method makes a step in pseudo-arclength (rather than λ). In nontechnical terms, we consider λ as a variable, instead of a parameter, in which case we need to append an additional equation to Eq. (1.36). There are several choices of the extra constraint [57]. One possibility that we employ in our computations is

$$\theta \|\mathbf{u} - \mathbf{u}_0\|^2 + (1-\theta)\|\lambda - \lambda_0\|^2 - d_s = 0, \tag{1.37}$$

where $0 \leq \theta \leq 1$ is a weighting parameter and d_s is the "distance" between $\mathbf{x}_0$ and the new solution we seek $\mathbf{x}$.

Algorithm 1 shows the general idea to construct bifurcation diagrams by using pseudo-archlength method.

Algorithm 1 Pseudo-archlength

Input: *MaxIter* is number of iteration, θ is weighting parameter, d_s is step size, $\mathbf{u}_0$ is initial condition at point $\lambda^{(1)}$, and $\lambda^{(2)}$ is initial point for the second iteration.
Output: $(\mathbf{u}^{(1)}, \mathbf{u}^{(2)}, \mathbf{u}^{(3)}, \ldots, \mathbf{u}^{(j)})$ are set of solutions from Eq. 1.34 at corresponding bifurcation parameters $(\lambda^{(1)}, \lambda^{(2)}, \lambda^{(3)}, \ldots, \lambda^{(j)})$, where $j \leq MaxIter$.

for $i = 1$ **to** *MaxIter* **do**
  if $i = 1$ **then**
    We solve $G(\mathbf{u}^{(1)}, \lambda^{(1)}) = 0$ with $\mathbf{u}_0$ as initial condition at point $\lambda^{(1)}$.
  else if $i = 2$ **then**
    We solve $G(\mathbf{u}^{(2)}, \lambda^{(2)}) = 0$ with $\mathbf{u}_0$ as initial condition at point $\lambda^{(2)}$.
  else
    We solve

$$\begin{aligned} G(\mathbf{u}^{(i)}, \lambda^{(i)}) &= 0, \\ \theta \|\mathbf{u}^{(i)} - \mathbf{u}^{(i-1)}\|^2 + (1-\theta)\|\lambda^{(i)} - \lambda^{(i-1)}\|^2 - d_s &= 0, \end{aligned}$$

    where

$$\begin{aligned} \mathbf{u}^{(i)} &= 2\mathbf{u}^{(i-1)} - \mathbf{u}^{(i-2)}, \\ \lambda^{(i)} &= 2\lambda^{(i-1)} - \lambda^{(i-2)}, \end{aligned}$$

    with $(\mathbf{u}^{(i-1)}, \lambda^{(i-1)})$ as initial condition.
  end if
  if Stopping criteria is achieved **then**
    Stop
  end if
end for

1.8 Overview of thesis

The aim of this thesis is to study the existence and behavior of the homoclinic snaking and the stability of localized solutions in several discrete systems.

In Chapter 2, we consider the discrete Swift-Hohenberg equation by discretizing the spatial derivative using central finite difference and introduce discretization parameter h. We note several interesting properties, such as multiple Maxwell points, snaking-like structures in the periodic solution, and complicated switchbacks in bifurcation diagrams of the localized solution. We also perform an asymptotic expansion to analyze the solution around the bifurcation point. Moreover, we also approximate the pinning region in the weakly coupled condition.

In Chapter 3, we study the discrete optical cavity equation with saturable nonlinearity. Therein, we study homoclinic snaking, linear stability, and pinning region of localized solutions. We calculate the pinning region by varying the coupling strength, linear, and nonlinear parameters. The appearance of the ⋐-shaped isola from the detachment process around the turning point in the snaking bifurcation is also being discussed. We also analyze and approximate the pinning region using a one-active site approximation.

In Chapter 4, we study the 2D discrete Allen-Cahn equation with cubic and quintic nonlinearity. The main difference with previous study by Taylor and Dawes [86] is that we consider three lattice types in 2D system, namely, square, honeycomb, and triangular lattice domains. Furthermore, we use active cell approximations to analyze and approximate the existing saddle-node bifurcations for all of the lattice types where good agreement is obtained.

Finally, Chapter 5 summarises our work carried out in this thesis and concludes with suggestions for future research.

Chapter 2

Homoclinic snaking in the discrete Swift-Hohenberg equation

2.1 Introduction

Homoclinic snaking in nonlinear dynamical systems is a snaking structure of the bifurcation curve for spatially localized states, which are homoclinic orbits in the phase space, in a parameter plane between a control parameter against, e.g., the norm of the states [94]. A standard model for pattern formation and the commonly studied equation for homoclinic snaking is the Swift-Hohenberg equation with cubic and quintic nonlinearity [26, 33, 58], that models a physical problem of fluid having thermal fluctuation near Rayleigh-Bernard instability [1, 85]. The snaking structure has (possibly infinitely) many turning points, i.e., saddle-node bifurcations, forming the boundaries of the snaking region [58]. In spatially continuous systems, the localized structures can appear as a result of bistability between a uniform state and a periodic state around the uniform state itself. Generally, the two states are connected by a front which can drift in one direction. However, at a specific parameter value known as Maxwell point, the front has no preference between the two states which occurs when they have

the same energy [16, 53]. Combining two fronts back to back forms a localized state that can make a snaking structure in its bifurcation curve. The phenomenon has been studied theoretically in, e.g., [10] that predicts the presence of snakes and ladders, [17, 60] that analyze localized periodic patterns using multiple scale expansions, [19–21] that provide thorough numerical continuations of homoclinic snaking in the Swift-Hohenberg equation, and [28] that studies localized patterns as particle-type solutions (see also [33] for a short review of coherent structure emergence based on localized structures). Homoclinic snaking has been observed experimentally in, e.g., spatially extended nonlinear dissipative systems [26], vertical-cavity semiconductor optical amplifiers [6], nematic liquid crystal layers with a spatially modulated input beam [51], and magnetic fluids [65].

Homoclinic snaking in continuous systems was first described in [11, 76] to be caused by a pinning effect, by which the front locks to the pattern, resulting in a finite range of parameter values around the Maxwell point where a stationary localized solution can exist. The interval in which a snaking occurs is also therefore referred to as the pinning region that has been studied numerically in, e.g., [19–21, 79, 94]. In general, the pinning effect cannot be described by multiple asymptotics [76], i.e., the length of the pinning region is exponentially small in a parameter which is related to the pattern amplitude. The approximation of the pinning region was provided by Kozyreff and Chapman [23, 60] and Dean *et al.* [35] using a beyond-all-order asymptotics and by Susanto and Matthews [68, 84] using variational methods.

Homoclinic snaking is also observed in spatially discrete systems, such as in the discrete bistable nonlinear Schrödinger equation [22, 24, 25], which leads to a subcritical Allen-Cahn equation [86], optical cavity solitons [97, 98], discrete systems with a weakly broken pitchfork bifurcation [27], and in patterns on networks appearing due to Turing instabilities [70]. If in the continuous case the

front locking is due to pattern formation, in the discrete systems it is due to the imposed lattice. The pinning region in this case was approximated analytically by Matthews and Susanto [68] and Dean *et al.* [34].

Note that in all the aforementioned references, homoclinic snaking is studied either in continuous systems or discrete ones that no longer admit snaking in the continuum limit. The transition of snaking structures from the discrete to the continuous limit is unfortunately rather lacking, which is particularly important because, e.g., when solving a continuous equation numerically, unavoidably one actually solves its discrete approximation. It is then necessary to recognize features that appear due to the discretization. Here, we provide a comprehensive study on the subject. We consider the discrete cubic-quintic Swift-Hohenberg equation, obtained from discretizing the spatial derivatives of the (continuous) Swift-Hohenberg equation with central finite differences. To our best knowledge, previous works on the discrete equation are only Peletier and Rodríguez [73, 78], who studied pattern formations in the system with a few sites only, and Collet [29] that views the system as a discrete-time lattice map and analyzes the instability of homogeneous stationary solutions.

Here, we report interesting and different properties that are not shared by the continuum counterpart, such as multiple Maxwell points, i.e., parameter values with periodic solutions having zero energies, bifurcation curves of periodic solutions exhibiting a snaking behavior, and localized states with complicated bifurcation diagrams. In general, we characterize three different regions of the discretization parameter, wherein the discrete Swift-Hohenberg equation behaves either similarly or differently from the continuum limit. Moreover, we provide theoretical analysis of the snaking and the pinning region in the uncoupled limit, i.e., weak coupling region, through formal perturbation expansions, which is generally applicable to any strongly discrete system.

The chapter is outlined as follows. The spatially discrete Swift-Hohenberg equation is discussed in Sec. 2.2. In the section, we also study the stability of the uniform solutions. We discuss periodic solutions in Sec. 2.3. Section 2.5 is on localized solutions and their asymptotic expressions that are obtained through multiple scale expansions. The width of the pinning region for varying parameters is also discussed in the section. We then derive this width asymptotically in the uncoupled limit in Sec. 2.6, which is then compared with computational results, where good agreement is obtained. Conclusions are in Sec. 2.7.

2.2 Governing equation and uniform solutions

The cubic-quintic Swift-Hohenberg equation is given by [17]

$$\frac{\partial u}{\partial t} = ru - \left(1 + \frac{\partial^2}{\partial x^2}\right)^2 u + b_3 u^3 - b_5 u^5, \tag{2.1}$$

where $u = u(x,t)$ is a scalar function defined on the real line, r is a real bifurcation parameter (control or stress parameter) [1], and b_3 and b_5 are nonlinearity coefficients. Equation (2.1) is invariant under $x \to -x$ and $u \to -u$. We take parameter $b_5 = 1$ [1, 21].

The discrete Swift-Hohenberg equation is obtained from (2.1) by discretizing the spatial derivatives using central finite difference

$$\frac{du_n}{dt} = (r-1)u_n - \frac{2}{h^2}\Delta_2 u_n - \frac{1}{h^4}\Delta_4 u_n + b_3 u_n^3 - b_5 u_n^5, \tag{2.2}$$

where $\Delta_2 u_n = u_{n+1} - 2u_n + u_{n-1}$, $\Delta_4 u_n = u_{n+2} - 4u_{n+1} + 6u_n - 4u_{n-1} + u_{n-2}$, and h is the discretization parameter. In the results presented below, mostly we take $b_3 = 2$. However, we also consider different values of the parameter.

In this work, we study the time-independent solution of Eq. (2.2), i.e.,

$$\frac{du_n}{dt} = 0. \tag{2.3}$$

Equation (2.1) can be written as $\frac{du_n}{dt} = -P\frac{\delta E}{\delta u_n}$, where the Lyapunov function E, referred to as the energy function of the system, is given by

$$\begin{aligned} E &= \frac{1}{P}\sum_{n=1}^{P}\left\{-\frac{1}{2}(r-1){u_n}^2 - \frac{1}{2}\left(\frac{(u_{n+1}-u_n)^2+(u_n-u_{n-1})^2}{h^2}\right) + \frac{1}{2}\frac{(u_{n-1}-2u_n+u_{n+1})^2}{h^4}\right. \\ &\quad \left. -\frac{1}{4}b_3{u_n}^4 + \frac{1}{6}b_5{u_n}^6\right\}, \end{aligned} \tag{2.4}$$

and P is the period of the solution, i.e., $u_{n+P} = u_n$.

The discrete Swift-Hohenberg equation has the same uniform solution $u_n = U_j$ as the continuum limit studied in [21], which is given by

$$0 = (r-1)U_j + b_3U_j^3 - b_5U_j^5, \tag{2.5}$$

that can be solved to yield

$$U_0 = 0, \quad U_+ = \left[\frac{1}{2b_5}\left(b_3 \pm \sqrt{b_3^2 + 4b_5(r-1)}\right)\right]^{\frac{1}{2}}, \tag{2.6}$$

and its mirror symmetric $U_- = -U_+$. The bifurcation diagram of the uniform solutions is shown in Fig. 2.1. The two branches of U_+ collide at

$$r_1 = 1 - \frac{b_3^2}{4b_5}$$

and U_+ with the minus sign bifurcates from U_0 at $r_2 = 1$.

To determine the linear stability of a solution $\tilde{u}_n$, we write

$$u_n = \tilde{u}_n + \epsilon e^{\lambda t}\hat{u}_n. \tag{2.7}$$

After substituting the ansatz into equation (2.2) and linearizing it about $\epsilon = 0$, we obtain the linear equation

$$\lambda \hat{u}_n = \mathcal{L}\hat{u}_n, \tag{2.8}$$

where

$$\mathcal{L} := r - 1 - \frac{2}{h^2}\Delta_2 - \frac{1}{h^4}\Delta_4 + 3b_3\tilde{u}_n^2 - 5b_5\tilde{u}_n^4$$

and the spectrum λ defines the stability of the solution $\tilde{u}_n$. A solution is said to be stable when all $\lambda \leq 0$ and unstable when $\exists\lambda > 0$. The spectrum of the linear differential operator $\mathcal{L}$ on the infinite dimensional space is the set of all complex numbers λ such that $(\mathcal{L} - \lambda)$ either has no inverse or is unbounded. In general, the spectrum of the linear operator will consist of a continuous spectrum and a discrete spectrum (eigenvalue) [54].

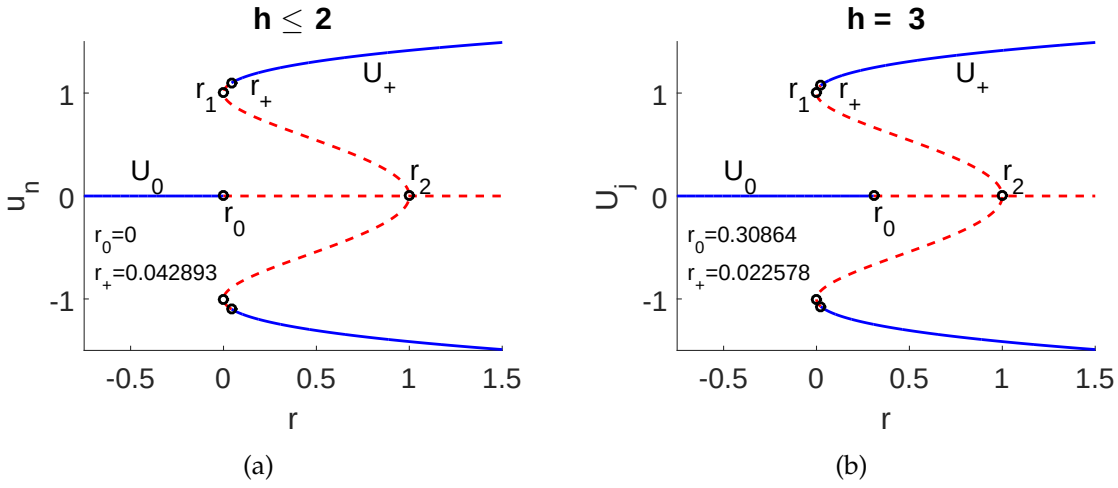

Figure 2.1. The existence curve of the uniform solutions of the governing equation (2.2). Blue solid and red dashed lines indicate, respectively, stable and unstable solutions.

For the uniform solution $\tilde{u}_n = U_j$, $j = 0, +, -$, one has $\hat{u}_n = e^{ikhn}$, where k is the wavenumber of the perturbation, from which we obtain the dispersion relation

$$\lambda(k) = r - 1 + 3b_3{U_j}^2 - 5b_5{U_j}^4 - 4\left(\frac{\cos(kh) - 1}{h^2}\right)\left(1 + \frac{\cos(kh) - 1}{h^2}\right). \tag{2.9}$$

The continuous spectrum is the interval of values that can be attained by λ for all $k \in \mathbb{R}$. The point r_0, i.e., $j = 0$ in (4.13), corresponds to the condition when the maximum of the function touches the horizontal axis, which is attained at the wave number

$$k = \frac{1}{h}\left(\pi \pm \arccos\left(\frac{1}{2}h^2 - 1\right)\right), \tag{2.10}$$

for $h < 2$ and

$$k = \pm\left(\frac{\pi}{h}\right), \tag{2.11}$$

for $h \geq 2$. The numbers are important in the study of bifurcating periodic solutions and localized solutions below. They will be the wave numbers of the carrier wave of the localized solutions.

2.2.1 Stability for $h < 2$

By substituting Eq. (2.10) into (4.13) and considering $j = 0$ and $\lambda(k) = 0$, we obtain that U_0 changes stability at

$$r_0 = 0. \tag{2.12}$$

Using the same procedure for U_+, we obtain that it changes stability at

$$r_+ = \frac{5}{4} - \frac{b_3}{8b_5}\left(b_3 + \sqrt{b_3^2 + 4b_5}\right). \tag{2.13}$$

Equations (2.12) and (2.13) indicate that the stability of U_0 and U_+ does not depend on the discretization parameter for $h < 2$. The stability of the uniform solutions is depicted in Fig. 2.1(a), which is the same as the continuous Swift-Hohenberg equation [21].

2.2.2 Stability for $h \geq 2$

Following the same steps as the case of $h < 2$, we obtain that for $h \geq 2$ the stability change for U_0 and U_+ occurs, respectively, at

$$r_0 = 1 - \frac{8}{h^2} + \frac{16}{h^4}, \tag{2.14}$$

$$r_+ = \left(1 + \frac{2}{h^2} - \frac{4}{h^4}\right) - \frac{b_3}{8b_5}\left(b_3 + \frac{1}{h^2}\sqrt{h^4 b_3^2 + 32b_5(h^2-2)}\right). \tag{2.15}$$

The stability of the uniform solutions now depends on h.

Figure 2.1(b) shows the bifurcation diagram of the uniform solutions for $h = 3$. The point r_0 at which U_0 changes its stability is shifted to the right. In the limit $h \to \infty$, the stability of U_0 changes at $r_0 = 1$. The stability of U_+ also changes as a function of h. We can see that r_+ is getting closer to r_1 as h increases and in the limit when $h \to \infty$, the stability of U_+ changes at $r_+ = r_1 = 0$.

One main difference between the uniform solutions of the continuous and the discrete equations is that in the strongly discrete case ($h > 2$), one can have a bistability between U_0 and U_+, i.e., when $r_0 > r_+$.

2.3 Periodic solutions

The discrete Swift-Hohenberg equation also admits periodic solutions that bifurcate from the uniform solution U_0 at $r = r_0$. We can obtain an approximation to the bifurcating periodic solution by writing

$$u_{P,n} = U_0 + \hat{\varepsilon}\cos(khn), \tag{2.16}$$

with $\hat{\varepsilon}$ small and k given by (2.10) or (2.11). Note that for the continuous function $f(x) = \cos(kx)$, its period is easily given by $P = 2\pi/k$. For the discrete function

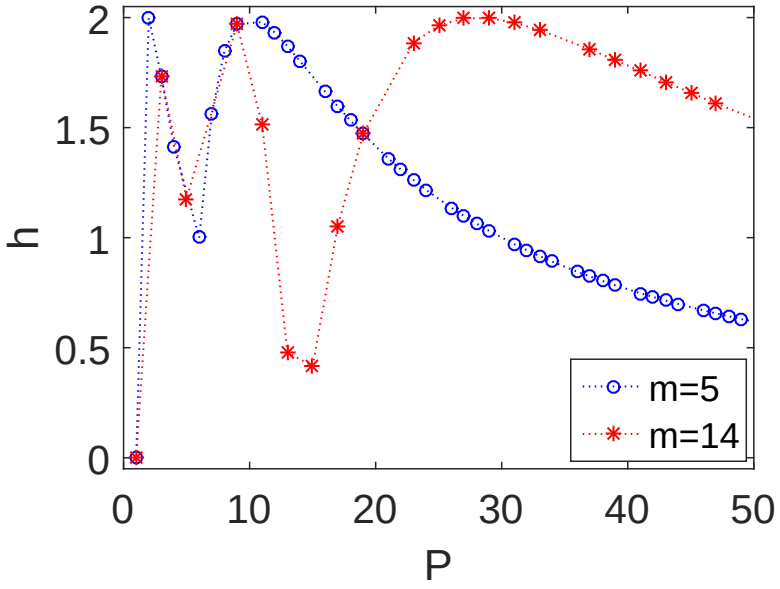

Figure 2.2. The relation between the discretization parameter h and the period P for $h \leq 2$ and two values of m, i.e., $m = 5$ and $m = 14$.

$f_n = \cos(khn)$, the period is calculated differently [71], i.e., it is periodic with period $P \in \mathbb{Z}^+$ if $\exists m \in \mathbb{Z}^+$ that does not have any factor in common with P, such that

$$P = \frac{2\pi m}{kh}. \tag{2.17}$$

The solution (2.16) is therefore periodic only if there are integers m and P with no common factors that satisfy (2.17). For $h < 2$, using (2.10) the plot of (2.17) is shown in Fig. 2.2 , relating the discretization parameter h and the period P for several values of m. Note that not every $h < 2$ will yield periodic solutions. There are values of the parameter that correspond to almost-periodic (i.e., quasi-periodic) functions. However, the study of these quasi-periodic solutions is beyond the scope of the present chapter and is addressed for future work. For $h \geq 2$, (2.17) with (2.11) implies that all the bifurcating periodic solutions have period $P = 2$.

Substituting Eq. (2.16) into the energy function (2.4) and finding the minimum of E, i.e.,

$$\frac{\partial E}{\partial \hat{\varepsilon}} = 0,$$

yield an approximate amplitude $\hat{\varepsilon}$ of the periodic solutions about U_0, that is given by

$$\hat{\varepsilon}(r) = \left(\frac{b_3 - (4rb_5 + b_3^2)^{\frac{1}{2}}}{2b_5} \right)^{\frac{1}{2}} \tag{2.18}$$

for $h < 2$ and

$$\hat{\varepsilon}(r) = \left(\frac{h^2 b_3 - \left[\left(b_5 (4r-1) + b_3^2 \right) h^4 + 32 b_5 \left(h^2 - 2 \right) \right]^{\frac{1}{2}}}{2b_5} \right)^{\frac{1}{2}} \tag{2.19}$$

for $h \geq 2$. One can also perform asymptotic analysis using multiple scale expansions to obtain the bifurcating periodic solution. This is presented in Section 2.4 [see (2.34)].

We solve Eq. (2.3) numerically using a Newton-Raphson method with periodic boundary conditions and using (2.16) and (2.18) or (2.19) as an initial guess in our numerics. Note that, herein, we take the computational number of sites N to be a multiple of P. We use a pseudo-arclength method to continue the computations past limit points [81]. We present the bifurcation diagram in the $(r, \|u\|)$ plane with

$$\|u\| = \left(\frac{1}{N} \sum_{n=1}^{N} u_n^2 \right)^{\frac{1}{2}}. \tag{2.20}$$

After a periodic solution is found, we determine its stability by solving the eigenvalue problem (2.8), where $\tilde{u}_n$ is now a periodic solution, i.e., $\tilde{u}_n = u_{P,n}$. At the same time, we also seek for its Maxwell points r_{M1}, i.e., points where the periodic state $u_{P,n}$ and the zero solution U_0 have the same energy ($E[u_{P,n}] = E[U_0] = 0$).

In the next subsections, we divide the parameter interval into three regions, i.e., $h < 1$, $1 \leq h < 2$, and $h \geq 2$. The main reason is the qualitative features of the solutions in each region, which are distinguishably different.

2.3.1 Periodic solutions for $h < 1$

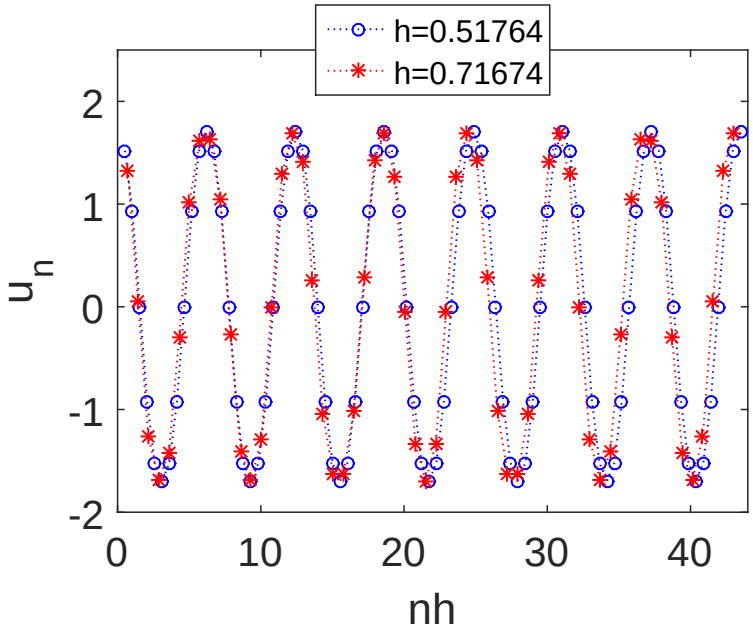

Figure 2.3. Periodic solutions for $h = 0.5176$ and 0.7167 for $r = 1$.

Figure 2.3 shows the profile of two periodic solutions for $h = 0.5176$ and 0.7167 which correspond to $P = 12, m = 1$ and $P = 60, m = 7$, i.e., the second solution has a period of five times larger than the first. We choose these two values of h that are representative to the case $h < 1$.

Figures 2.4(a) and 2.4(b) show the bifurcation diagram and the stability of the periodic solutions for the two values of h above. The diagrams are similar to those of the continuous Swift-Hohenberg equation [21]. However, the discretization causes the appearance of an additional branch and possibly a Maxwell point. Note that in the continuous case, periodic solutions only have one upper branch and one Maxwell point [19, 20]. In panel (a), we also plot the analytical approximation (2.16) and (2.34), that is obtained using multiple scale asymptotics, showing good agreement.

Figures 2.4(c) and 2.4(d) show the energy function of the periodic solutions for the two values of h above. Both panels show similar plots to those of the

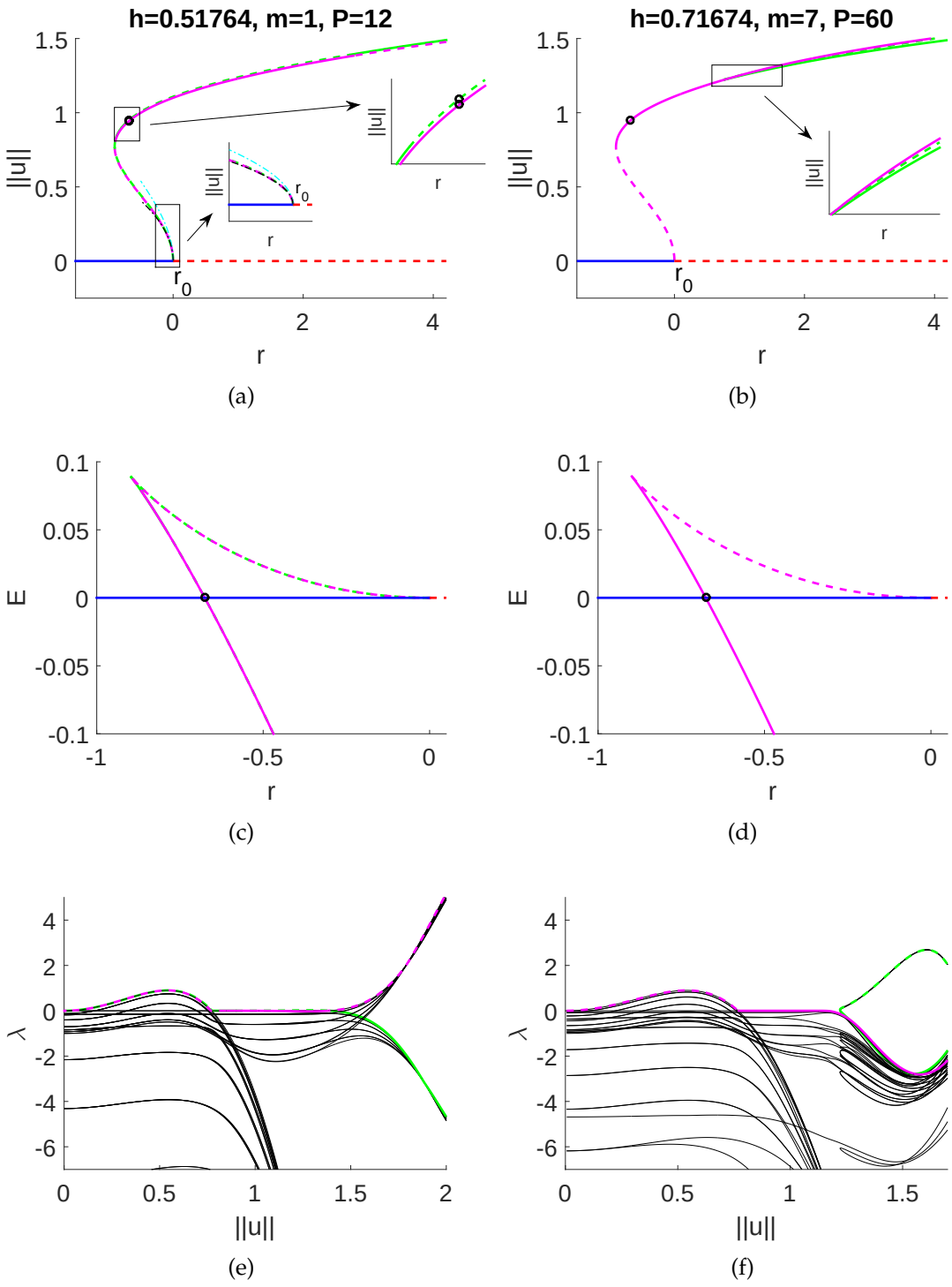

Figure 2.4. (a), (b) Bifurcation diagrams of periodic solutions for (a) $h = 0.5176$ and (b) $h = 0.7167$. (c), (d) The energy function of the periodic solutions. (e), (f) Eigenvalues of the periodic solutions. The magenta and green lines correspond to periodic solutions along the main and extra bifurcation curves, respectively. Black thin lines in (e) and (f) indicate non-critical eigenvalues of the periodic solutions. Solid and dashed lines correspond to stability and instability, respectively. Circles indicate Maxwell points. The dashed-dotted cyan and black lines in panel (a) are amplitudes (2.16) and (2.34), respectively.

continuous Swift-Hohenberg equation. The energy curves of the periodic solution $E[u_P]$ cross the horizontal axis at Maxwell points. In panel (c) the points are at $r_{M1} = -0.6755$ (stable) and $r_{M1} = -0.6754$ (unstable), while in panel (b) the (stable) Maxwell point is at $r_{M1} = -0.6762$. The free energy curves of the two upper branches are indistinguishably close to each other.

Figures 2.4(e) and 2.4(f) show the spectrum of the periodic solutions along the two branches. Green and magenta lines indicate the critical eigenvalues of the periodic solutions along the primary and secondary upper branch.

We also considered several other values of the discretization parameter h. The main difference between the continuous and the weakly discrete case is indeed the presence of an extra branch of periodic solutions that may also contain an additional Maxwell point. We conjecture that the splitting point where the primary and the secondary upper branches emerge moves to $r \to \infty$ as $h \to 0$, even though it may not increase uniformly. Note that in Fig. 2.4(a) the value of h is smaller than that in Fig. 2.4(b), but the branching point of the former occurs at a smaller value of r than that of the latter. Additionally there can be changes of the stability of the periodic solutions along the upper branches.

2.3.2 Periodic solutions for $1 \leq h < 2$

Figures 2.5(a) and 2.5(b) show the bifurcation diagrams of several periodic solutions for two values of h in the interval $1 \leq h < 2$. The diagrams show snaking behavior with multiple Maxwell points along the stable and unstable branches, which was not seen in the previous case $h < 1$ (including the continuous case).

Figures 2.5(c) and 2.5(d) show the corresponding solutions at the points indicated in Fig. 2.5(b). At the beginning, the solution looks like localized states separated by a finite distance. As the norm increases, it gradually delocalizes and forms long stretches of periodic oscillations enclosed by fronts as shown in

Fig. 2.5(d). Both cases of localization and delocalization are equivalent to a single localized state in a finite domain. This explains the slanted snaking diagrams observed in Fig. 2.5 (see also Fig. 2.6 that will be discussed later) [59]. When the solution becomes completely oscillating, the existence curve stops snaking.

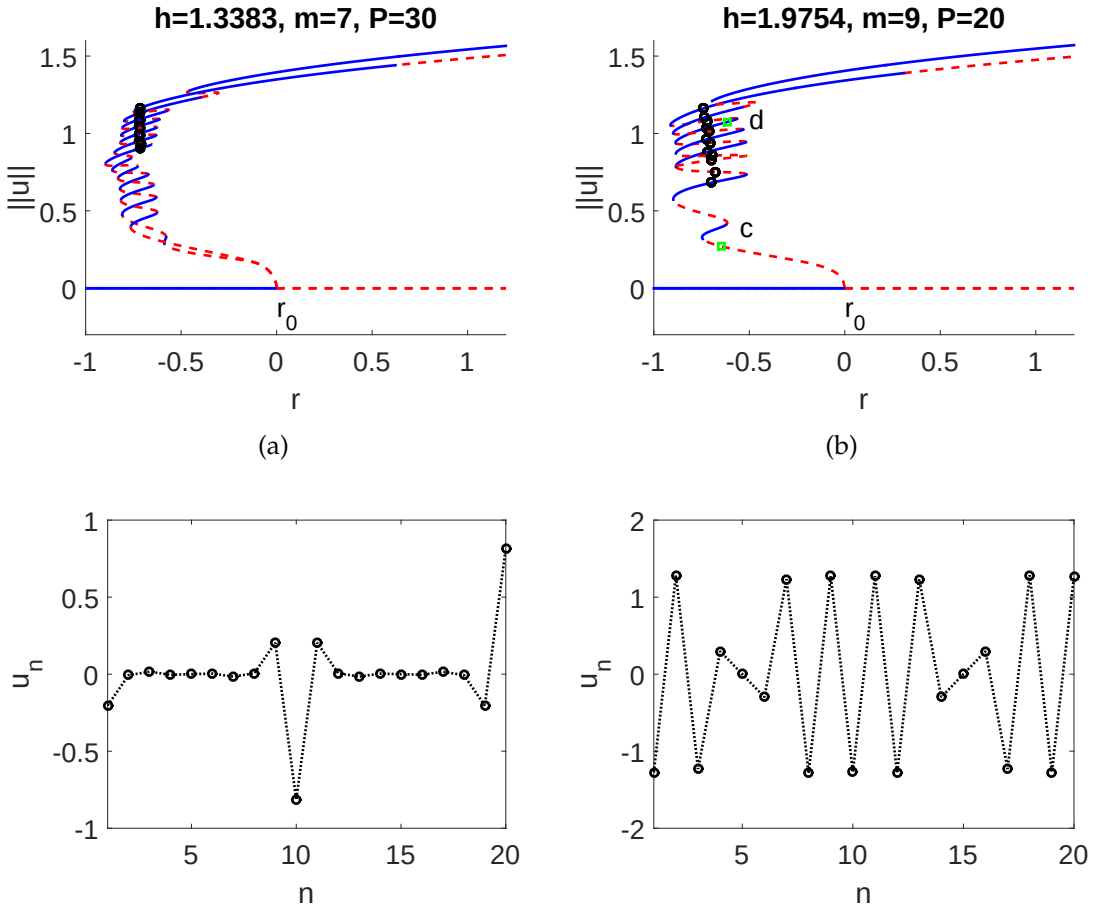

Figure 2.5. (a), (b) The bifurcation diagram of periodic solutions for two values of h with $1 \leq h < 2$. (c), (d) Solution profiles for $h = 1.9754$ at several values of r, indicated in (b).

Comparing the panels in 2.5(a) and 2.5(b), one can note that the complexity of the snaking in the bifurcation curves does not depend on the discretization parameter h. To study how the bifurcation curve in one of the panels changes into the other, one would normally vary the parameter h. However, in the present numerical setup it may not be possible because we fix the number of sites following the periodicity of the solution, which depends on h. To be consistent, if we were

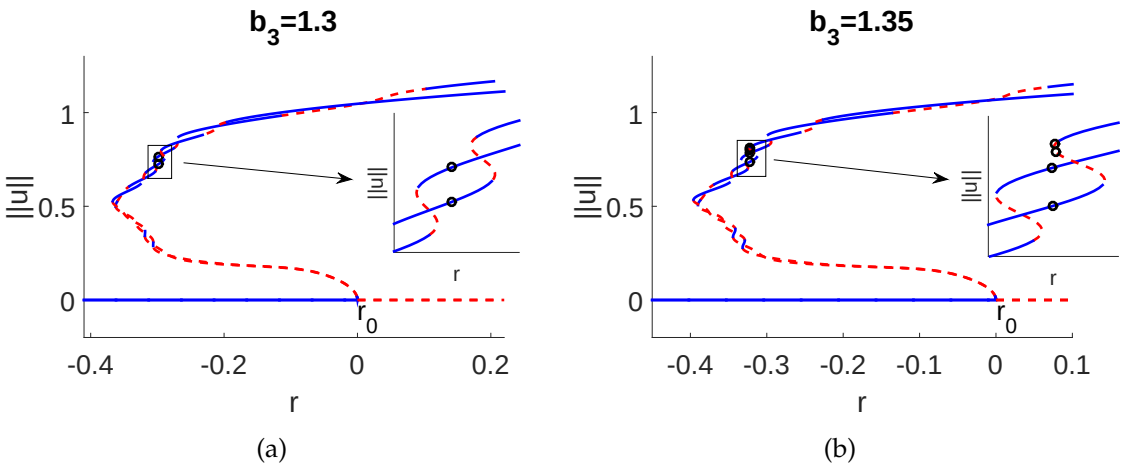

(a) (b)

Figure 2.6. The appearance of additional Maxwell points as we vary parameter b_3 for $h = 1.3383$, $m = 7$, and $P = 30$.

to vary the parameter we would also need to change the number of grid points, which can be non trivial to do. In the infinite domain, the change may be related to the attachment or detachment of some parts of the bifurcation curves.

The presence of multiple Maxwell points due to the vanishing of the energy function of the periodic solutions seems to be related to the snaking. To understand the appearance of the additional Maxwell points, it is easier to study them through varying b_3 than h, which is shown in Fig. 2.6. The existence curve that initially only has two Maxwell points are seen to have four Maxwell points in Fig. 2.6(b) as b_3 increases. Such an addition occurs from the tip of a turning point, i.e., a saddle-node bifurcation.

2.3.3 Periodic solutions for $h \geq 2$

Figure 2.7 shows the bifurcation diagram of two periodic solutions for $h \geq 2$. Note that in this case, the wave number is always π as given in (2.11) and hence $P = 2$. The parameter only causes the bifurcation point r_0 to shift to the right. As $h \to \infty$, the bifurcation diagram will be equivalent to that of the uniform solution, see Fig. 2.1.

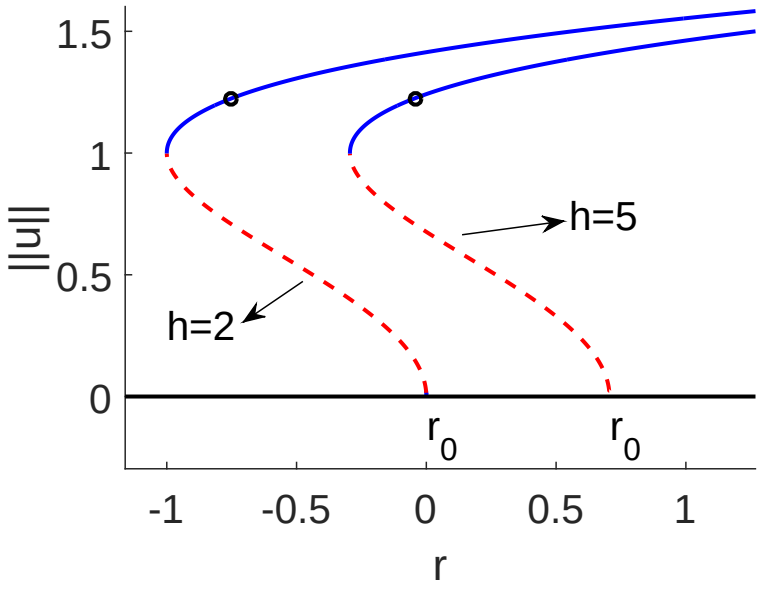

Figure 2.7. Bifurcation diagram of the periodic solutions for $h \geq 2$.

We can obtain the Maxwell point r_{M1} exactly by equaling the energy of the zero and the periodic solutions (2.3) and (2.19) to yield

$$r_{M1} = 1 - \frac{8}{h^2} + \frac{16}{h^4} - \frac{3b_3^2}{16b_5}. \tag{2.21}$$

2.4 Asymptotic expansion of localized solutions

Defining new variables [95]

$$X = \epsilon n, \quad T = \epsilon^2 t, \quad r = \epsilon^2 r_1 + r_0,$$

and writing

$$\begin{aligned} u_n(t) \;=\; & \epsilon e^{i\psi} F(X,\tau,T) + \epsilon^2 G_0(X,\tau,T) + \epsilon^2 e^{i\psi} G_1(X,\tau,T) + \epsilon^2 e^{2i\psi} G_2(X,\tau,T) \\ & + \epsilon^3 H_0(X,\tau,T) + \epsilon^3 e^{i\psi} H_1(X,\tau,T) + \ldots + \text{c.c.}, \end{aligned} \tag{2.22}$$

where $\psi = khn$ with k being the wavenumber of the carrier wave (2.10), (2.11), and c.c. denotes the complex conjugation, we obtain

$$\begin{aligned} u_{n\pm j}(t) &= \epsilon e^{i\psi_{n\pm j}}\left[F \pm j\epsilon\frac{\partial F}{\partial X} + (j\epsilon)^2\frac{1}{2}\frac{\partial^2 F}{\partial X^2} \pm \ldots\right] + \epsilon^2\left[G_0 \pm j\epsilon\frac{\partial G_0}{\partial X} + (j\epsilon)^2\frac{1}{2}\frac{\partial^2 G_0}{\partial X^2} \pm \ldots\right] \\ &\quad + \epsilon^2 e^{i\psi_{n\pm j}}\left[G_1 \pm j\epsilon\frac{\partial G_1}{\partial X} + (j\epsilon)^2\frac{1}{2}\frac{\partial^2 G_1}{\partial X^2} \pm \ldots\right] + \ldots + \text{c.c.} \end{aligned} \tag{2.23}$$

and

$$\frac{d}{dt} = \frac{\partial}{\partial t} + \epsilon^2\frac{\partial}{\partial T}. \tag{2.24}$$

Next, we substitute Eqs. (2.22) and (2.23) into the discrete Swift-Hohenberg equation (2.2) and equate the coefficients of each harmonic in ψ at each order of ϵ.

At $O\left(\epsilon e^{i\psi}\right)$, we have

$$\left[1 - r_0 + 4\left(\frac{\cos(kh)-1}{h^2}\right)\left(1 + \frac{\cos(kh)-1}{h^2}\right)\right]F = 0. \tag{2.25}$$

Because F cannot be zero, its coefficient must vanish, which is satisfied for k and r_0 given by Eqs. (2.10) and (2.12), or (2.11) and (2.14), respectively.

At $O\left(\epsilon^2 e^{i\psi}\right)$, we obtain

$$\left[\frac{4i\sin(kh)}{h^4}\left(2(\cos(kh)-1) + h^2\right)\right] = 0. \tag{2.26}$$

At $O\left(\epsilon^3 e^{i\psi}\right)$, we obtain

$$F_T = AG_{1X} + CF_{XX} + 3b_3\bar{F}F^2 + r_1 F - \left[1 - r_0 + 4\left(\frac{\cos(kh)-1}{h^2}\right)\left(1 + \frac{\cos(kh)-1}{h^2}\right)\right]H_1, \tag{2.27}$$

where

$$\begin{aligned} A &= -\left[\frac{4i\sin(kh)}{h^4}\left(2(\cos(kh)-1) + h^2\right)\right] \\ C &= -2\left[\frac{\cos(kh)\left(h^2-2\right) + 2\cos(2kh)}{h^4}\right]. \end{aligned} \tag{2.28}$$

By using (2.25) and (2.26), we can eliminate the coefficient of H_1 and obtain Ginzburg-Landau equation for F

$$F_T = CF_{XX} + 3b_3|F|^2F + r_1F. \tag{2.29}$$

Because we focus on the time-independent system $F_T = 0$, we have

$$CF_{XX} + 3b_3|F|^2F + r_1F = 0, \tag{2.30}$$

where

$$C = -\frac{\left(h^2-4\right)}{h^2} \tag{2.31}$$

and

$$C = \frac{2\left(h^2-4\right)}{h^4} \tag{2.32}$$

for $h \leq 2$ and $h > 2$, respectively.

The uniform solution of equation (2.30) is

$$F(X) = \left(-\frac{r_1}{3b_3}\right)^{\frac{1}{2}} e^{i\phi}, \tag{2.33}$$

corresponding to spatially periodic states with period P near $r = 0$

$$u_{P,n} = 2\left(\frac{(r_0-r)}{3b_3}\right)^{\frac{1}{2}} \cos\left(khn+\phi\right) + O(r-r_0).$$

Localized states satisfying $F \to 0$ as $X \to \pm\infty$ are given by

$$F(X) = \left(-\frac{2r_1}{3b_3}\right)^{\frac{1}{2}} \operatorname{sech}\left(X\left(\frac{r_1}{C}\right)^{\frac{1}{2}}\right)e^{i\phi}, \tag{2.34}$$

that using (2.22) lead to the solution (2.35).

2.5 Localized solutions

In the continuum limit $h \to 0$, there are localized solutions bifurcating from r_0 [21]. In the following, we study the effect of the dicretization to such solutions.

As derived in Section 2.4, localized solutions of the discrete Swift-Hohenberg equation bifurcating from r_0 are given asymptotically at the leading order by

$$u_{l,n} = \sqrt{\frac{2(r_0 - r)}{3b_3}}\,\mathrm{sech}\left(hn\left(\frac{(r-r_0)}{C}\right)^{\frac{1}{2}}\right) \times \cos\Big(khn + \phi\Big) + O(r - r_0). \tag{2.35}$$

Note that the parameter ϕ is the phase of the pattern within the sech envelope, which within this asymptotics remains arbitrary. In the continuum limit $h \to 0$, the phase-shift is $\phi = 0$ or $\pi/2$ [21], which can only be determined using exponential asymptotics [23, 60, 68, 84]. Here, aside from the locking between the sech envelope and the underlying wave train, for $h > 0$ there is also the possibility for the envelope to be locked with the spatial discretization. However, this will be beyond the scope of this chapter and in the following we will only consider the phase pertaining to the continuous limit above.

2.5.1 Snaking regions: r vs. h

By using Eq. (2.35) as our initial guess for the numerics, we obtain the existence curve of localized solutions. Figure 2.8 shows the bifurcation diagram of the localized solutions that form the snaking behavior for the phase-shift $\phi = 0$ and $\pi/2$ for a value of $h < 1$. The vertical axis is the solution norm [see (2.20)]. We also show the corresponding solutions in the same figures.

One can note that the bifurcation diagram is similar to that of the continuous Swift-Hohenberg equation [21]. However, we note one difference where up in

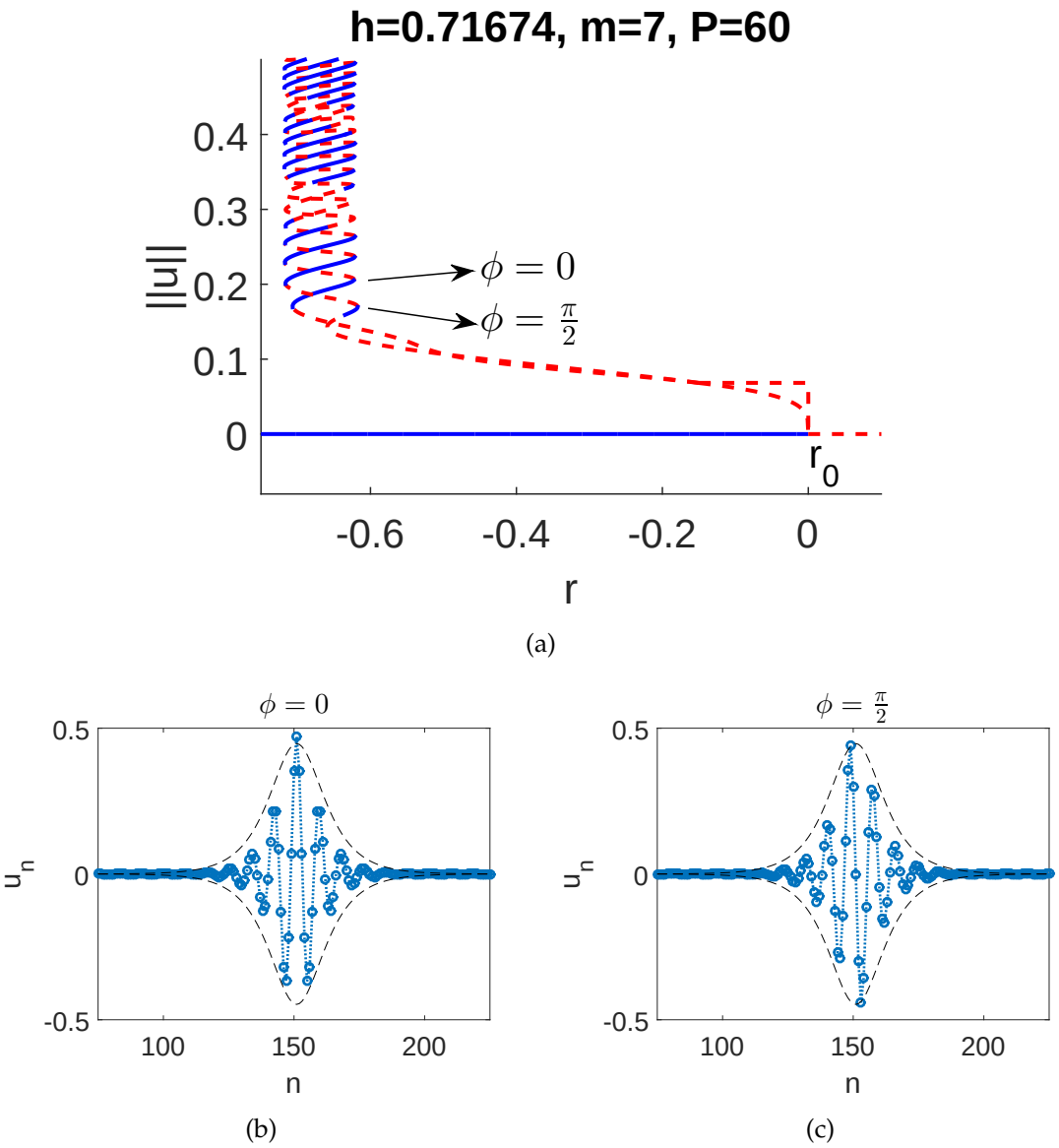

Figure 2.8. (a) Bifurcation diagram of the localized solution for $h = 0.71674$ with $m = 7$, $P = 60$. (b), (c) Profiles of localized solutions next to the bifurcation point r_0. The dashed curves in panel (b), (c) correspond to the envelope given by (2.35).

the snaking diagram, we obtain intervals of norm where both solutions are all unstable.

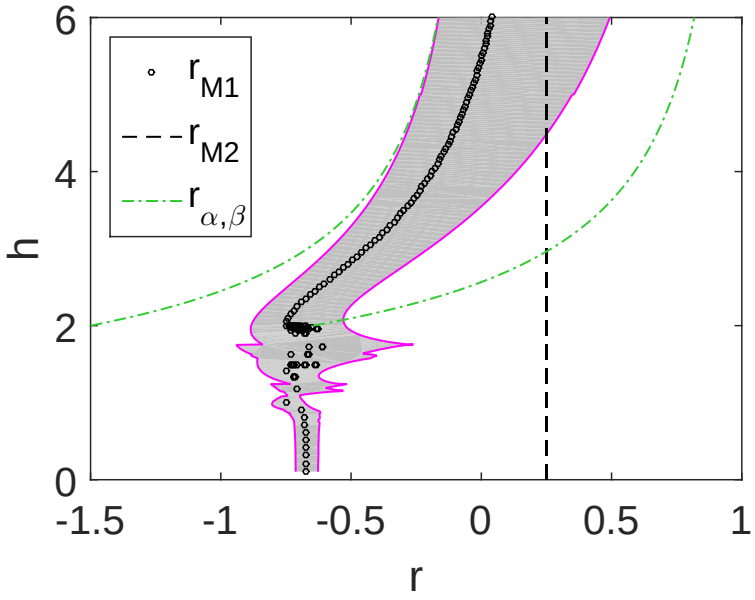

Figure 2.9. The pinning region as a function of h indicated by the gray area. The Maxwell points are also denoted. r_{M2} is defined in (2.36). r_α and r_β are analytical approximations derived in Sec. 2.6.

At present we may conclude that the discretization parameter h only effects slightly to the snaking behavior. However, in the following we will show that the range of parameter $1 \leq h < 2$ is particularly peculiar as there are detachments of snaking structures.

In Fig. 2.9 we plot the pinning region, which is bounded by left and right turning points of the snaking curve, for varying h. We obtain smooth boundaries in the regions $h < 1$ and $h \geq 2$, while there are jumps and pikes of pinning region boundaries in the region $1 \leq h < 2$. Analyzing the snaking profiles around the jump or spiking points closely, we obtain that they correspond to the detachment of a snaking profile from the main branch as depicted in Fig. 2.10.

Figure 2.10(a) shows the bifurcation diagram before the jump, showing a complex snaking. Right after the jump, we obtain a much simpler snaking structure as shown in Fig. 2.10(b). The change of the bifurcation diagram in panel

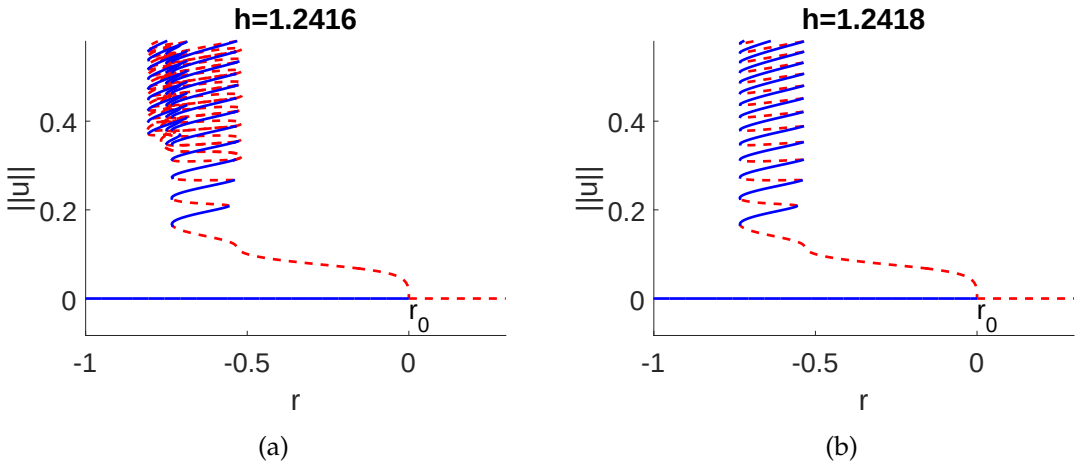

Figure 2.10. The homoclinic snaking (a) before and (b) after a jump in Fig. 2.9.

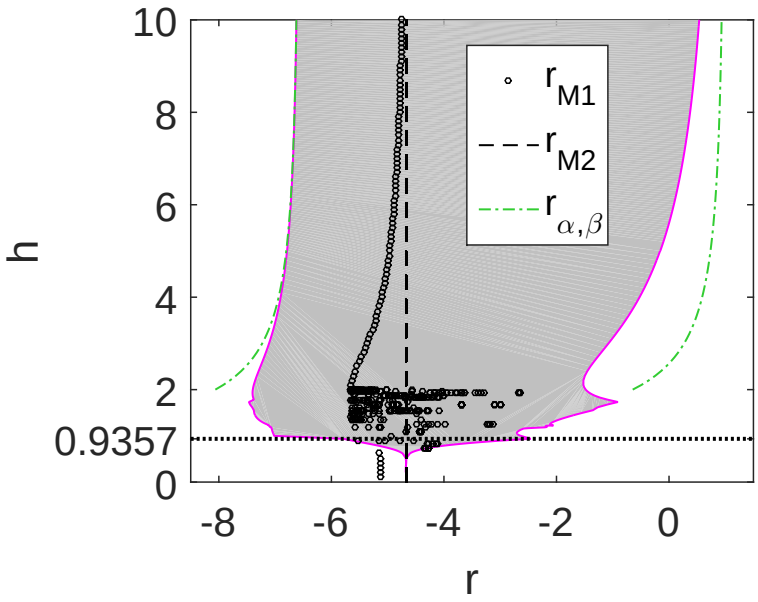

Figure 2.11. The same as in Fig. 2.9 for $b_3 = 5.5$. The horizontal dotted line indicates a sample value of h that will be considered further later (see Fig. 2.12) for having three types of localized solutions.

(a) to that in panel (b) is due to the detachment of a snaking structure (not shown here) from the main branch, which is the general scenario of the jumps and pikes observed in Fig. 2.9.

Overall we say from Fig. 2.9 that for $h < 1$, the influence of the discretization from the fourth derivative term is more dominant than the second derivative one, while for $h \geq 2$ it is the opposite. For the intermediate interval $1 \leq h < 2$,

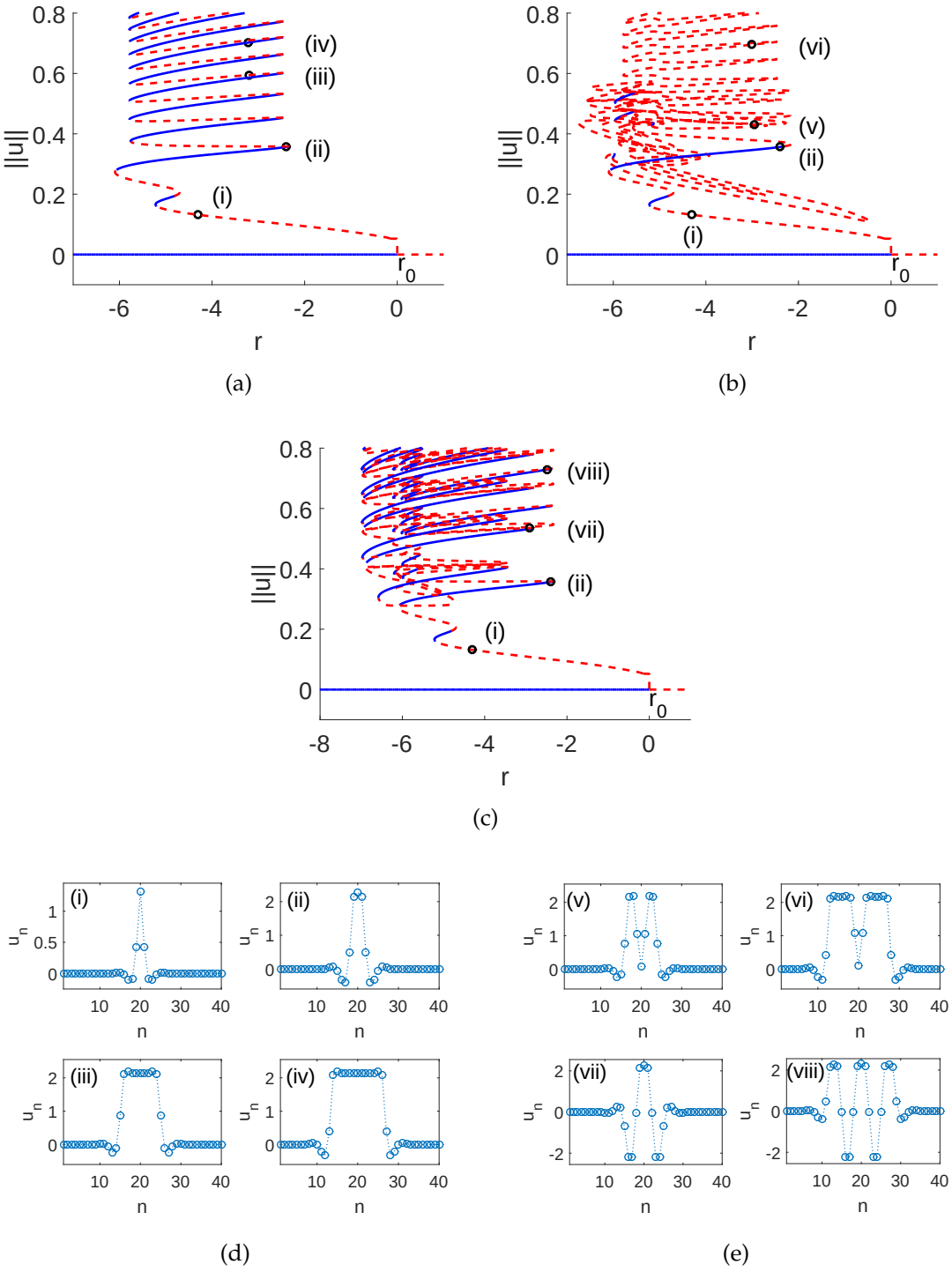

Figure 2.12. Three different snaking diagrams (a)-(c) and their localized solutions (d) and (e) that were obtained for $h = 0.9357$ with $\phi = 0$ and $b_3 = 5.5$. The three diagrams share the same portion of curve between r_0 and point (ii). In the continuum limit $h \to 0$, only the bifurcation diagrams in (a) and (b) were reported in [19].

the influence of the discretization from the second and the fourth derivatives is relatively the same that yields non-trivial bifurcation curves.

In Fig. 2.9, we depict Maxwell points defined previously as the points when the energy of the periodic solutions vanishes. It is particularly interesting to note that there are many Maxwell points in the region $1 \leq h < 2$, especially when $h \to 2$. Additionally, we also plot r_{M2} as vertical dashed line, that is defined as the point when the energies of U_+ and U_0 are equal, i.e., $E[U_+] - E[U_0] = 0$. The point can be calculated easily as

$$r_{M2} = 1 - \frac{3b_3^2}{16b_5}, \tag{2.36}$$

which is exactly the same as that of the continuum limit [21]. This special point will also be relevant later on when we consider the effect of varying b_3.

In the continuous case, it was shown that the pinning region enlarges with increasing b_3 and above a critical $b_3 \approx 3.521$ there is no snaking formed any more [21]. The snaking simply just collapses into a vertical line. This happens when the right boundary of the snaking region touches the special point (2.36). In Fig. 2.11 we plot the pinning region for varying discretization parameter h with $b_3 = 5.5$. One can observe that for small h indeed there is no snaking. However, when h is large enough, a snaking behavior is obtained again.

For this value of b_3, we also still see jumps and pikes along the pinning region boundaries. In this case we even observe a more complicated structure than that in Fig. 2.10, where the snaking involves three different branches. One example is for $h \sim 0.9357$. We show in Fig. 2.12 the different branches and their corresponding solutions.

The three bifurcation diagrams in Figs. 2.12(a), 2.12(b), and 2.12(c) share the same portion of curves from the bifurcation point r_0 until point (ii). Point (ii) is a bifurcation point, from which emanates the three different branches. In Figs.

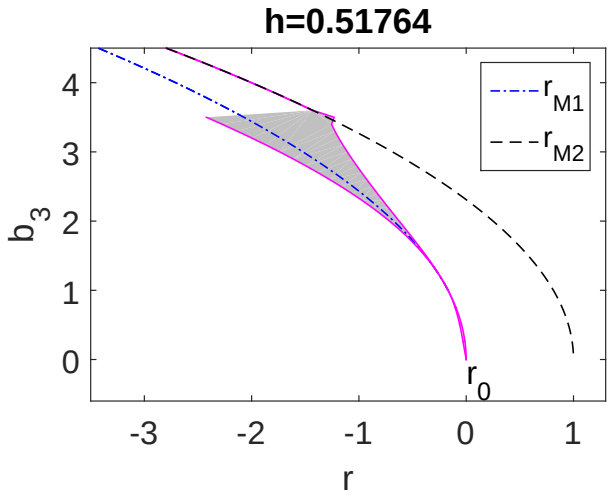

(a)

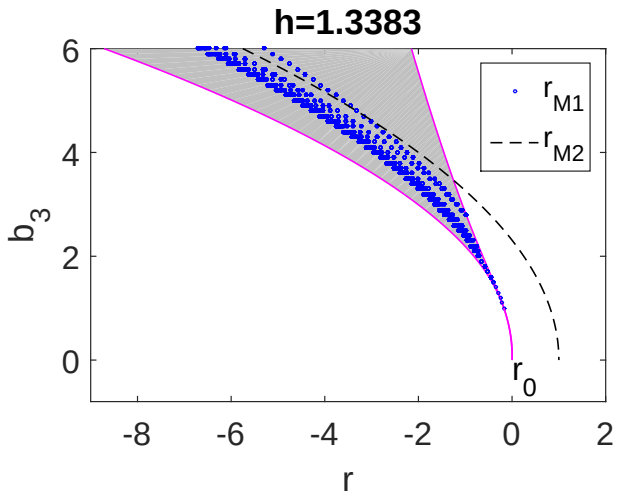

(b)

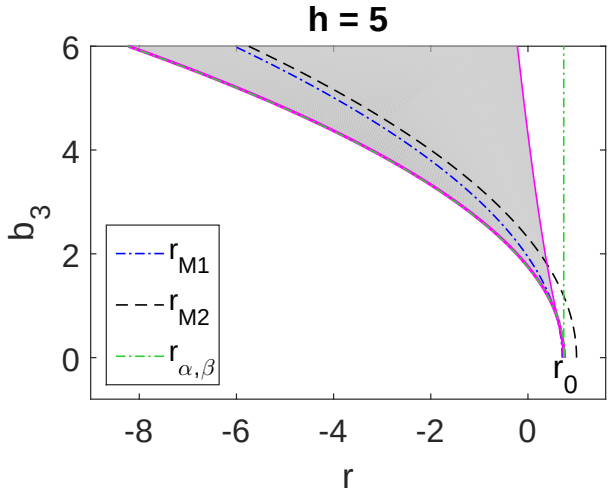

(c)

Figure 2.13. The pinning regions indicated by the gray area for three different values of h representing the region (a) $h \leq 1$, (b) $1 \leq h < 2$, and (c) $h \geq 2$. See the text for the definition of r_{M1}, r_{M2}, r_α, and r_β.

2.12(d) and 2.12(e) we show the corresponding solution profiles for each branch at the indicated points in Figs. 2.12(a), 2.12(b), and 2.12(c).

For $h < 0.9357$, the solutions are similar to those in Fig. 2.12(d), i.e., branch in Fig. 2.12(a). For $h \approx 0.9357$, the solutions in Figs. 2.12(d) and 2.12(e) coexist. In particular, localized solutions such as those shown in Fig. 2.12(e) are the ones that give a complicated bifurcation diagram that experiences detachment and attachment processes for $0.9357 \leq h < 2$.

Solutions in Figs. 2.12(d) and 2.12(e) can be seen to rather have a flat plateau around U_+, from which one obtains their relation to the special point r_{M2} [19]. In the continuum limit $h \to 0$, the reported diagram was only that shown in Figs. 2.12(a) and 2.12(b) [19].

Here, we would like to study further the effect of the parameter b_3 on the snaking in the discrete system. We now fix h and vary b_3 instead.

Figure 2.13(a) shows the pinning region for $h < 1$ represented by $h = 0.51764$. The region behaves quite similarly as the continuous Swift-Hohenberg equation [19]. Maxwell point is always inside the snaking region. Beyond $b_3 = 3.521$, the solution stops snaking and follows the point r_{M2} [21].

Figure 2.13(b) shows the pinning region for $1 \leq h < 2$, which is represented by $h = 1.3383$. The discretization causes the presence of multiple Maxwell points appearing inside the pinning region. What is notable is the result that unlike the previous case for $h < 1$, here the pinning region does not feel the presence of the special point r_{M2}.

Figure 2.13(c) shows the pinning region for $h \geq 2$, which is represented by $h = 5$. The result shows that there is only one Maxwell point (2.21). Note that r_{M1} and r_{M2} converge to the same point when $h \to \infty$. The point r_{M2} does not affect the pinning region just like in the previous case when $1 \leq h < 2$.

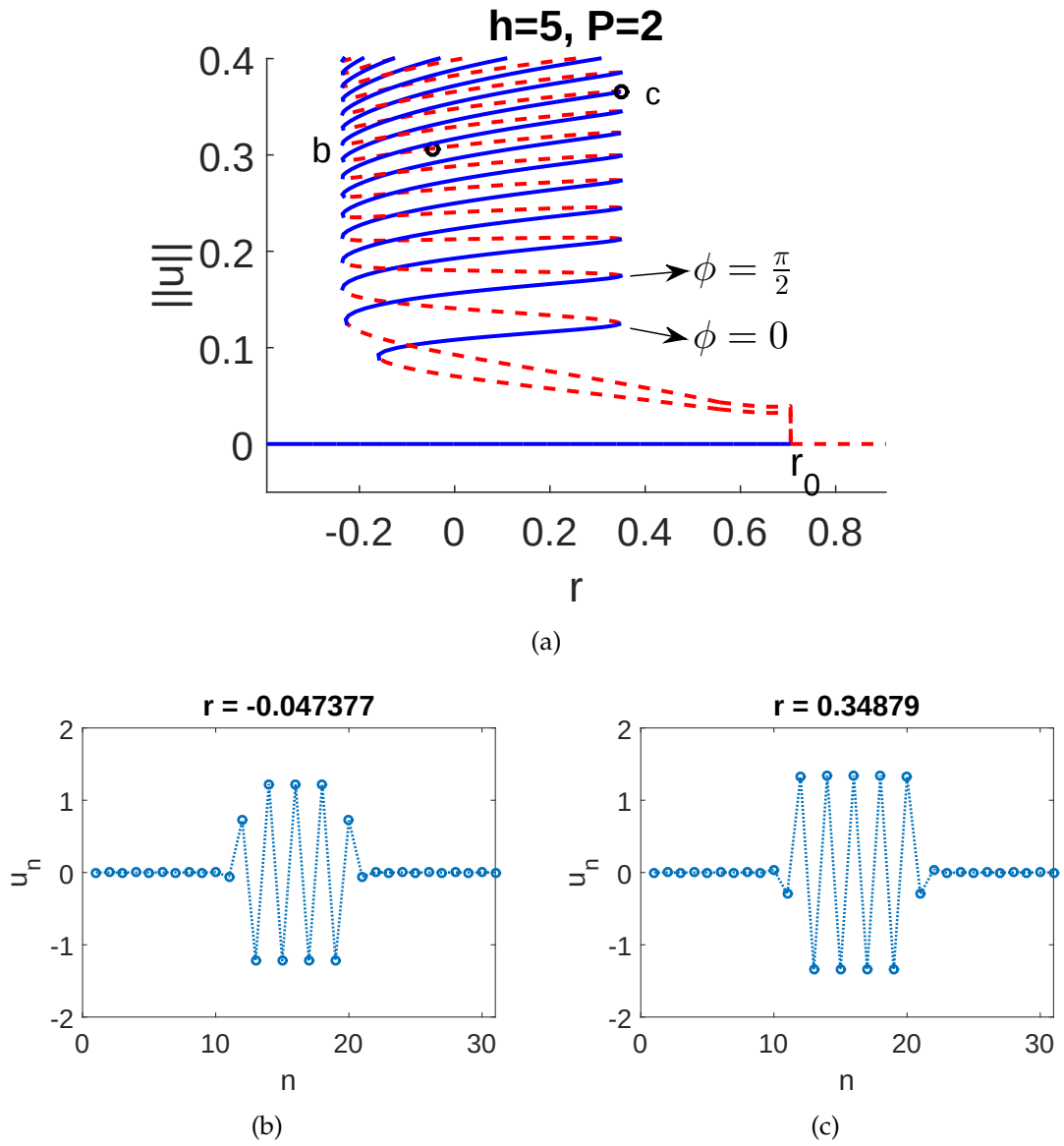

Figure 2.14. The bifurcation diagram of localized solutions for $h = 5$ and their corresponding profiles at the points indicated by the letters in (a).

2.6 Analytical approximation

It is important to note that when $h \gg 1$, the discrete system is actually weakly coupled. Figure 2.14 shows the bifurcation diagram of localized solutions for $h = 5$ and the corresponding solutions. The panels show the fact that as we vary r along the branch, there is basically only one node that is active and varies following

the variation of the parameter r, while the other points are either in the periodic solution part or in the region of the uniform zero solution.

From (2.2), we can assume that up in the snaking diagram only five nodes are involved in the dynamics, i.e.,

$$u_{n-2} = 0, \quad u_{n-1} = 0, \quad u_n = v, \quad u_{n+1} = \pm\hat{\varepsilon}, \quad \text{and} \quad u_{n+2} = \mp\hat{\varepsilon}. \tag{2.37}$$

Here, $\hat{\varepsilon}$ is the approximate amplitude of the periodic solution given by (2.19) and v is the active node. Substituting (2.37) into the time-independent discrete Swift-Hohenberg equation (2.2) will yield a fifth order polynomial for the variable v

$$P_5(v) = -b_5 v^5 + b_3 v^3 + \left(r - 1 + \frac{4}{h^2} - \frac{6}{h^4}\right) v \mp \frac{2\hat{\varepsilon}}{h^2} \pm \frac{5\hat{\varepsilon}}{h^4} = 0. \tag{2.38}$$

We call (2.38) a one-active site approximation. Without loss of generality, we can consider one sign only from the plus-minuses in the polynomial because of its symmetry. We plot in Fig. 2.15 the polynomial (2.38) for $h = 5$.

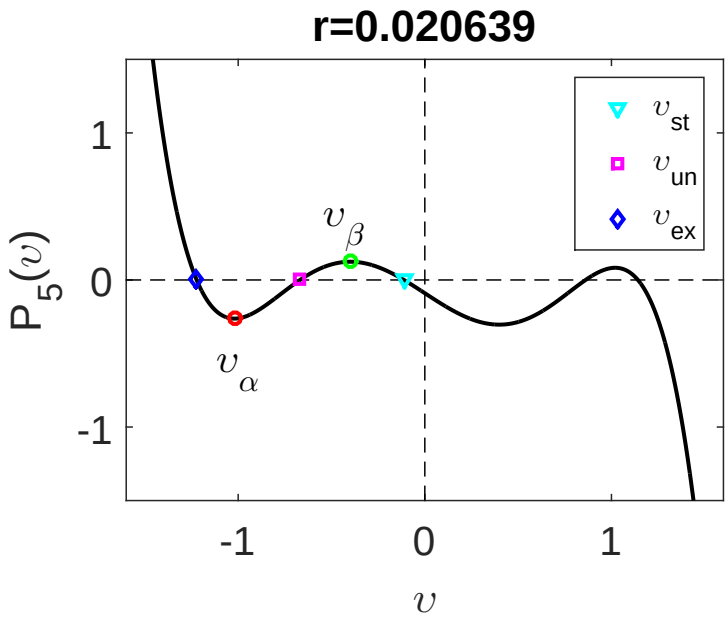

Figure 2.15. One-active site polynomial for $h = 5$. v_α and v_β represents the left and the right pinning boundary. v_{st} represents the stable site of the lower solution. v_{un} represents the unstable site of the solution. v_{ex} represents the stable site of the upper solution.

In general, the function will have five real roots. Three of them are related to the snaking as they can disappear in a saddle-node bifurcation with varying r. The roots are indicated in Fig. 2.15. The boundaries of the pinning region can then immediately be recognized as the condition when the local minimum at $v = v_\alpha$ or the local maximum at $v = v_\beta$ touches the horizontal axis. To be precise, v_α and v_β correspond to the left and right boundaries of the pinning region, respectively.

It is rather straightforward to obtain that

$$\begin{aligned} v_{\alpha,\beta} &= \frac{1}{10b_5 h}\left(10b_5\left(3b_3h^2 \pm \left(h^4\left(20b_5\left(r-r_0\right)+9b_3^2\right)-80h^2b_5+200b_5\right)^{\frac{1}{2}}\right)\right)^{\frac{1}{2}} \\ &= \frac{1}{\sqrt{10b_5}}\left(3b_3 \pm \left(20b_5\left(r-r_0\right)+9b_3^2\right)^{\frac{1}{2}}\right)+\mathcal{O}\left(\frac{1}{h}\right). \end{aligned} \tag{2.39}$$

The boundaries of the pinning region are then given by

$$r_{\alpha,\beta} \approx \hat{r}_{\alpha,\beta} - \frac{2}{h^2}\left(2+\frac{\sqrt{5b_3+5\sqrt{4b_5\left(\hat{r}_{\alpha,\beta}-1\right)+b_3^2}}}{\sqrt{3b_3+\sqrt{20b_5\left(\hat{r}_{\alpha,\beta}-1\right)+9b_3^2}}}\right), \tag{2.40}$$

with

$$\hat{r}_\alpha = 1-\frac{b_3^2}{4b_5}, \quad \hat{r}_\beta = 1 \tag{2.41}$$

Comparisons between the numerical results and the approximations above are shown in Figs. 2.9, 2.11, and 2.13(c), where we can see that in general the approximation $r_{\alpha,\beta}$ gives good results particularly for the left boundary.

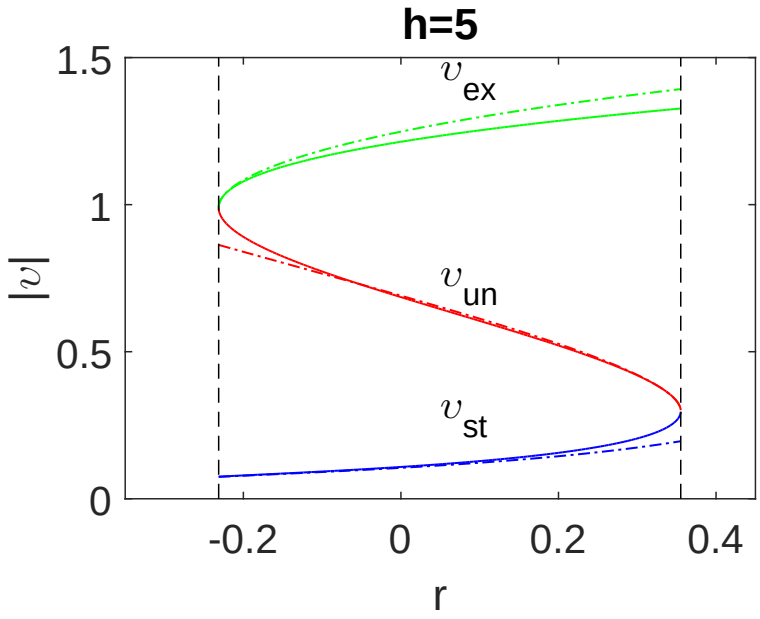

Figure 2.16. Comparisons of the roots of (2.38) that are related to snaking obtained numerically (solid lines) and the approximations (2.42), (2.43), and (2.44) (dashed lines). Here, $h = 5$.

We can also asymptotically obtain the three particular roots to be given by

$$v_{st} \approx \frac{\hat{\varepsilon}\left(2h^2-5\right)}{h^4(r-r_0)-4h^2+10}, \tag{2.42}$$

$$v_{un} = v_\beta - \sqrt{\frac{\left(r-r_\beta\right)}{10v_\beta^2 b_5 - 3b_3}} + O\left(r-r_\beta\right), \tag{2.43}$$

$$v_{ex} = v_\alpha + \sqrt{\frac{(r-r_\alpha)}{10v_\alpha^2 b_5 - 3b_3}} + O(r-r_\alpha). \tag{2.44}$$

Comparisons between the numerically computed roots of (2.38) relevant to snaking and the approximations (2.42), (2.43), and (2.44) are shown in Fig. 2.16.

We compare in Fig. 2.17(a), 2.17(c), and 2.17(e) the numerical results obtained from the solution of the full system and the approximations (2.37) using roots of the one-active site polynomial (2.38). One can see that the approximations are good.

Next, we will show that the one-active site approximation can also be used to approximate the critical eigenvalue of localized solutions in the pinning region.

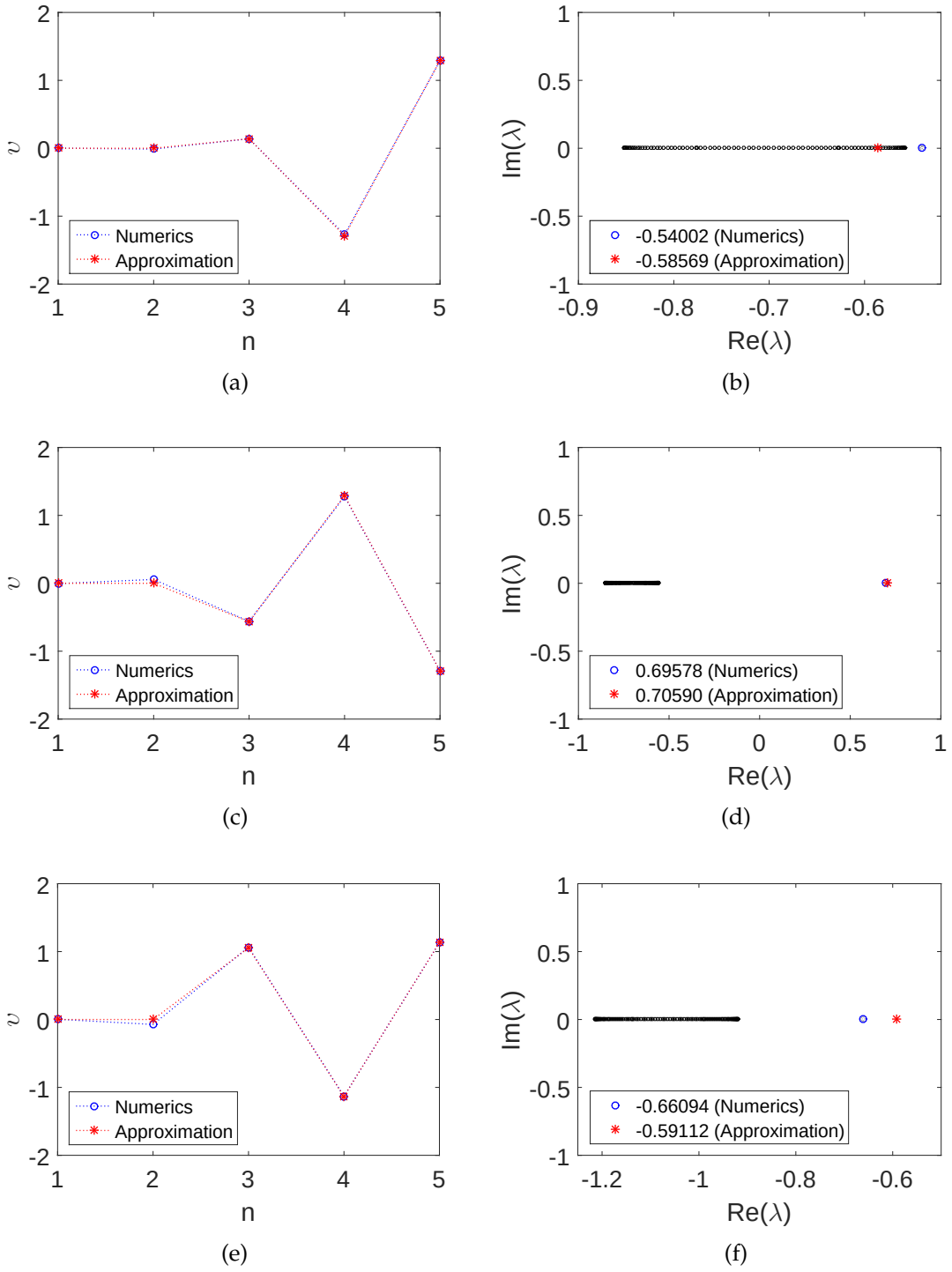

Figure 2.17. (a), (c), and (e) Comparisons between the numerically obtained localized solutions of the discrete Swift-Hohenberg equation (2.2) and the one-active site approximation (2.37) for $h = 5$. (b), (d), and (f) The corresponding spectrum of the localized solutions in the top panels that are computed numerically and the eigenvalue (2.46) approximating the critical spectrum.

This is obtained from realising that the dynamics of the active site will satisfy the equation $v_t = P_5(v)$. It is then immediate that the eigenvalue will be given by the linear eigenvalue problem

$$\lambda v = \frac{d}{dv} P_5(v)\Big|_{v=v_{st,un,ex}} v, \tag{2.45}$$

i.e.,

$$\lambda_{st,un,ex}(r) = -5b_5 v_{st,un,ex}^4 + 3b_3 v_{st,un,ex}^2 + \left(r - 1 + \frac{4}{h^2} - \frac{6}{h^4}\right). \tag{2.46}$$

Figures 2.17(b), 2.17(d), and 2.17(f) show numerically computed spectrum of the profiles in Figs. 2.17(a), 2.17(c), and 2.17(e) and our approximation (2.46), where rather excellent agreement is obtained.

2.7 Conclusion

We have considered a discrete Swift-Hohenberg equation that is obtained from discretizing the spatial derivatives of the continuous one. We have studied time-independent solutions, namely, uniform, periodic, and localized solutions and their (in)stabilities, from which we concluded that in terms of the discretization parameter h, the equation can be distinguished into three different regions, i.e., $0 < h < 1$, $1 \leq h < 2$, and $h \geq 2$. In the first interval, the uniform, the periodic and the localized solutions of the discrete Swift-Hohenberg equation have similar properties with the continuous case. As a direct consequence, our study indicates that to solve the (continuous) Swift-Hohenberg equation numerically using finite central differences, it can be sufficient to use relatively large $h < 1$.

As the discretization parameter becomes larger, features different from the continuous counterpart may emerge, such as instability of localized solutions for both phase $\phi = 0$ and $\pi/2$ for the same parameter values, extra bifurcation curves

for the periodic and localized solutions, and multiple Maxwell points. Moreover, one may also obtain a snaking structure in the bifurcation diagram of periodic solutions, that does not exist in the continuous limit, as well as complicated snaking structures for localized solutions.

Analytical approximations have been developed for the periodic and the localized solutions. The periodic solution amplitudes have been determined using variational methods, while the localized solutions have been approximated using asymptotic analysis.

The boundaries of the pinning region, i.e., of the homoclinic snaking that is associated with the localized solutions, have been studied numerically as well as analytically by developing a one-active site approximation. We have shown that the approximation can also be used to approximate the critical eigenvalue of a localized solution. Comparisons of the analytical results and the numerics show good agreement.

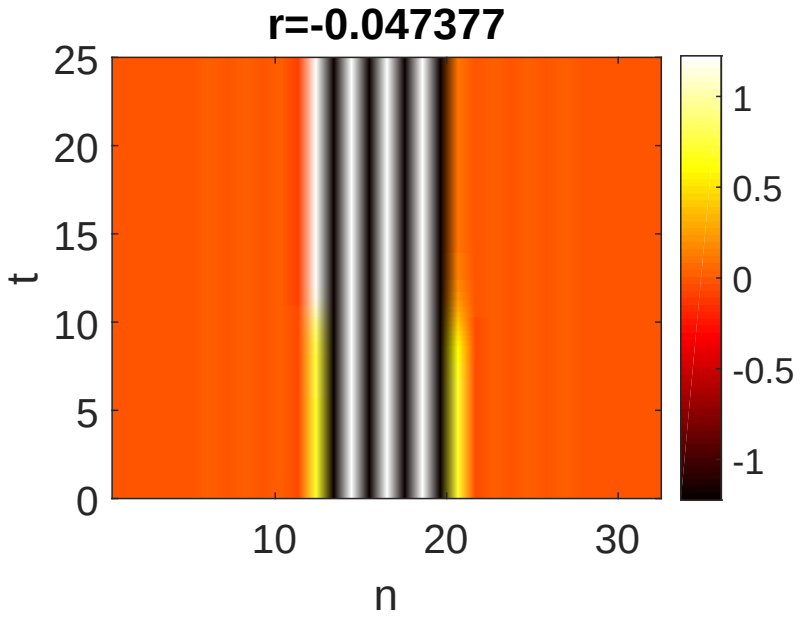

Figure 2.18. Time dynamics of the unstable solution shown in Fig. 2.14(b), that corresponds to point b in Fig. 2.14(a). The symmetric solution evolves into an antisymmetric one, which corresponds to a point on the stable branch right above point b.

In this work, we mainly only considered time-independent solutions, where we determined their local (in)stability from computing the spectrum of their corresponding linear differential operator. The typical time evolution of the unstable solutions, which is rather related to global dynamics, is depicted in Fig. 2.18, where an unstable solution would settle into a stable neighboring one.

Discussing time-dependent solutions, it is interesting to study the effect of parametric time-periodic forcing [46] to the snaking behavior in discrete systems, which is addressed for future work. The mechanism for snaking or non-snaking in discrete systems (in the continuous case, it is discussed in [2]) is also proposed to be studied in the future.

Chapter 3

Homoclinic snaking of discrete solitons in saturable optical cavities

3.1 Introduction

Recently, there has been a great interest in the study of localized patterns in nonlinear systems with rich multiplicity now known as homoclinic snaking [10, 18–21, 32, 33, 60, 66, 67]. While homoclinic snaking mostly has been studied in spatially continuous systems, it also occurs in spatially discrete models [25, 61, 74, 86, 96, 97].

In general, localized states are formed by combining back to back of two different states, which can be spatially periodic and uniform states or two different uniform states, and may occur because of the presence of bistability regime between the states. Homoclinic snaking appears as a bifurcation parameter is being varied. Along the existence diagram, new "rolls" in spatially continuous systems or new "sites" in weakly coupled equations are added at both fronts (i.e., Pomeau fronts) [19, 60, 76].

In nonlinear optics, homoclinic snaking has been observed experimentally in, e.g., driven optical systems [44], in 2D vertical-cavity surface-emitting lasers

(VCSELs) [88], vertical-cavity semiconductor optical amplifier [6], a spatially forced system [51], and liquid crystal light-valve [14].

The parameter interval where homoclinic snaking exists is called a pinning region and has been studied analytically and numerically for continuum and anti-continuum cases [19–21, 23, 35, 61, 68, 79, 84, 94]. Within this region, localized states have possibly infinitely many distinct stable solutions [97, 98] around the Maxwell point [76], which is a parameter value where the two states of localized solutions have the same energy [16, 53]. Pomeau recognized the snaking structure to be caused by a beyond-all-orders phenomenon [76].

In this work, we consider a discrete Ginzburg-Landau-type equation with saturable nonlinearity, which is a common mathematical model to study optical cavities [96–98]. Considering the same type of equations, but with a cubic nonlinearity, will result in the discrete Lugiato-Lefever equation [42, 43, 74]. The equation models light propagation in an array of weakly coupled optical waveguides [40, 41, 43]. The saturation creates families of both bright and gray solitons exhibiting multistability as they develop internal shelves in the pinning region for either zero or finite losses [98]. Previous numerical works also include homoclinic snaking and infinite multistability of stationary patterns [97] and the appearance of isolas via symmetry breaking [96]. However, homoclinic snaking in the equation has yet to be explored analytically.

The aim of the present chapter is to provide a detailed analysis of uniform and localized states of the equation and their bifurcation diagrams forming homoclinic snaking. We study the formation of isolas of $\Subset$-shaped from a homoclinic snaking reported previously in [96]. Moreover, we present a semianalytical approximation to the width of the pinning region using a one-active site assumption. Even though the current work considers optical cavities with saturable nonlinearity, our results can be straightforwardly extended to cubic nonlinearity as well.

The chapter is organized as follows. The spatially discrete governing equation is discussed in Section 3.2. In the section, we also study uniform solutions and their linear stability. We discuss localized solutions, homoclinic snaking, and the formation of ⋐-shaped isolas in Section 3.3. We approximate the width of the pinning region analytically using a one-active site method in Section 3.4. We also compare the result with numerical computations in the section, where good agreement is obtained provided that the arrays are weakly coupled. Conclusions are in Section 3.6.

3.2 Mathematical Model

In this study, we consider the one-dimensional lattice equation for a complex field $A_n \in \mathbb{C}$, $n \in \mathbb{Z}$:

$$i\partial_t A_n + \delta A_n + \frac{\alpha|A_n|^2}{1+|A_n|^2}A_n + c\Delta A_n = P, \tag{3.1}$$

where $\Delta A_n = A_{n+1} + A_{n-1} - 2A_n$. A_n represents the amplitude of the nth identical optical resonator in a one-dimensional array [97], $c \geq 0$ denotes the strength of the nearest-neighbour coupling between oscillators. P is the amplitude of an applied optical pump field (real-valued and independent of n), which is our control/bifurcation parameter. $Re(\delta) = \delta_r$ represents detuning of the pump frequency from the resonant frequency of the oscillators. $Re(\alpha)$ indicates the strength of Kerr effect of the intensity-dependent refractive index. $Im(\delta) = \delta_i$ and $Im(\alpha)$ are linear and nonlinear loss terms, respectively. Using the results of [97], here we focus on two cases of parameter values, which yield rich dynamics and represent the general snaking behaviours in the discrete optical cavities, i.e.,

- Case 1 : $\delta = -9.2 + i$ and $\alpha = 10$,
- Case 2 : $\delta = 4 + i$ and $\alpha = -10$.

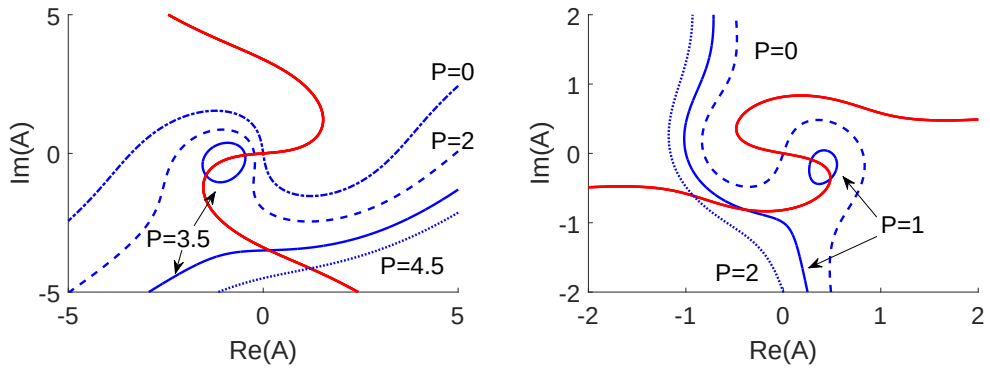

(a) Case 1 (b) Case 2

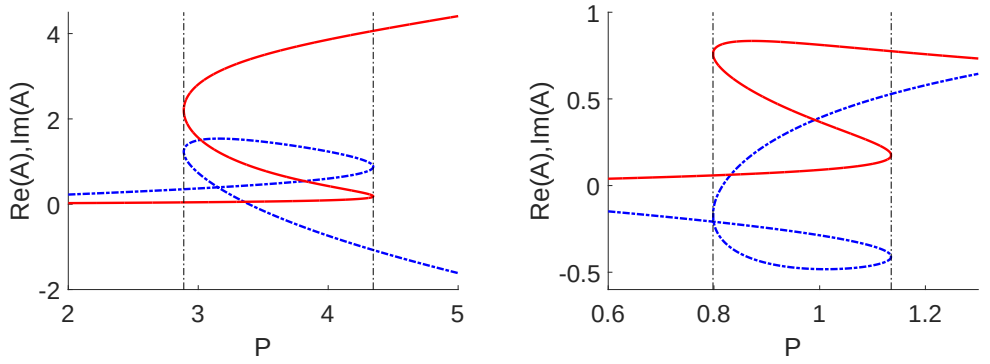

(c) Case 1 (d) Case 2

Figure 3.1. (a), (b) Contour plots of the algebraic equation (3.7) at several P. The blue solid/dashed/dotted lines represent the real parts of the equations $Re(F_u)$, while the red solid lines are for the imaginary parts $Im(F_u)$. Intersections between the blue and red curves represent uniform solutions of (3.7). The red curve from $\mathrm{Im}(F_u) = 0$ is independent of the optical pump field P because $P \in \mathbb{R}$. (c), (d) The uniform solutions as a function of P. The blue dotted-dashed and red solid lines in (a) and (b) indicate the real and the imaginary part of the solutions, respectively.

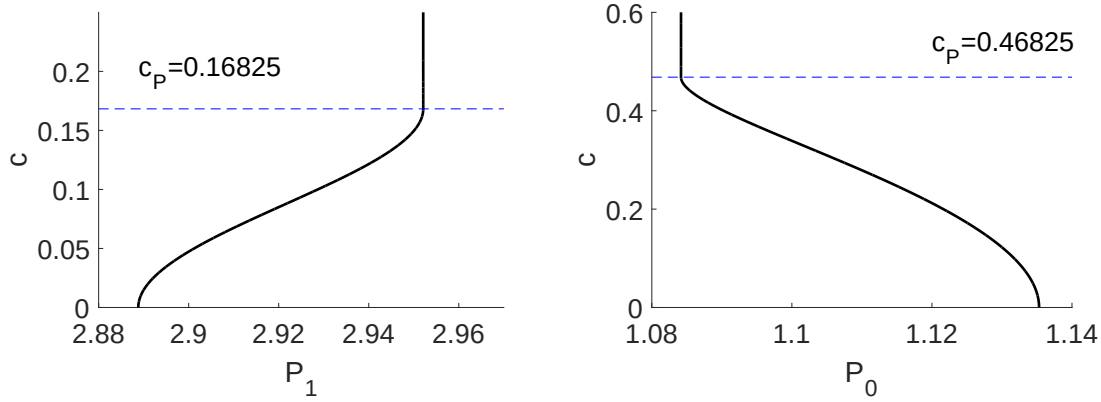

(a) Case 1 (b) Case 2

Figure 3.2. (In)stability point of the uniform solutions for case 1 and 2.

We consider the time-independent solution of equation (3.1), i.e.,

$$\delta A_n + \frac{\alpha|A_n|^2}{1+|A_n|^2}A_n + c\Delta A_n = P, \tag{3.2}$$

Once a solution $A_n = \tilde{A}_n = \tilde{x}_n + i\,\tilde{y}_n$ is obtained, its linear stability is then determined by writing

$$x_n = \tilde{x}_n + \epsilon\hat{x}_n e^{\lambda t},\ y_n = \tilde{y}_n + \epsilon\hat{y}_n e^{\lambda t}. \tag{3.3}$$

Substituting (3.3) into (3.1), linearizing about $\epsilon = 0$ and splitting the real and imaginary part of the resulting equations, we obtain the linear eigenvalue problem

$$\lambda\begin{pmatrix}\hat{x}_n\\ \hat{y}_n\end{pmatrix} = \mathcal{L}\begin{pmatrix}\hat{x}_n\\ \hat{y}_n\end{pmatrix}, \tag{3.4}$$

where

$$\mathcal{L} = \begin{pmatrix} -\delta_i - m_{11} & -\delta_r - c\Delta - m_{12}\\ \delta_r + c\Delta - m_{21} & -\delta_i - m_{22}\end{pmatrix} \tag{3.5}$$

is the linear differential operator of Eq. (3.1) and

$$\begin{aligned} m_{11} &= \frac{2\alpha\tilde{x}_n\tilde{y}_n}{\left(1+\tilde{x}_n^2+\tilde{y}_n^2\right)^2}, & m_{12} &= \frac{\alpha\left[\left(\tilde{x}_n^2+\tilde{y}_n^2\right)^2+\left(3\tilde{y}_n^2+\tilde{x}_n^2\right)\right]}{\left(1+\tilde{x}_n^2+\tilde{y}_n^2\right)^2},\\ m_{21} &= \frac{-\alpha\left[\left(\tilde{x}_n^2+\tilde{y}_n^2\right)^2+\left(3\tilde{x}_n^2+\tilde{y}_n^2\right)\right]}{\left(1+\tilde{x}_n^2+\tilde{y}_n^2\right)^2}, & m_{22} &= \frac{-2\alpha\tilde{x}_n\tilde{y}_n}{\left(1+\tilde{x}_n^2+\tilde{y}_n^2\right)^2}. \end{aligned} \tag{3.6}$$

A solution is said to be stable when $\mathrm{Re}(\lambda) < 0$ for all the eigenvalues and unstable otherwise.

3.2.1 Uniform solutions

Equation (3.1) has uniform solutions (homogeneous states) $A_n(t) = A$ satisfying

$$F_u(A) = \delta A + \frac{\alpha |A|^2}{1+|A|^2} A - P = 0. \tag{3.7}$$

Figure 3.1 shows the nullclines of the real and imaginary parts of F_u (3.7) for several values of P. As intersections between the blue and red curves represent uniform solutions of (3.7), we obtain that depending on P, we can have one or three solutions. The interval of P for three roots is bounded by turning points, where two roots coalesce. We present in Figs. 3.1(c) and 3.1(d) the roots as a function of P.

To determine the linear stability of the uniform solutions, one has $\hat{x}_n = ae^{ikn}$, $\hat{y}_n = be^{ikn}$, where k is the wave number of the perturbation, from which we obtain the dispersion relation

$$\lambda(k) = -\delta_i - \frac{1}{2}(m_{11} + m_{22}) \pm \frac{1}{2}\sqrt{\Gamma}, \tag{3.8}$$

where

$$\begin{aligned} \Gamma &= -8\cos(k)c\left[2\cos(k)\left(c + m_{12} - m_{21} - 4c + 2\delta_r\right)\right] - 4\left(\delta_r - m_{21}\right)\left(m_{12} + \delta_r\right) \\ &\quad -8c\left(2c - 2\delta_r - m_{12} + m_{21}\right) + \left(m_{11} - m_{22}\right)^2. \end{aligned}$$

A uniform solution is said to be stable when $\lambda(k)<0$ for $\forall k \in \mathbb{R}$ and unstable when $\exists k$ such that $\lambda(k) > 0$. The maximum of the spectrum (3.8) is attained at

$$k = \pm \begin{cases} \pi & , c < c_P \\ \arccos\left(\dfrac{4c - m_{12} + m_{21} - 2\delta_r}{4c}\right) & , c \geq c_P \end{cases} \tag{3.9}$$

where

$$c_P = \frac{1}{8}(m_{12} - m_{22} - 2\delta_r),$$

which is a parameter threshold for the stability change point of the uniform solution, see Fig. 3.2.

Figures 3.3(a) and 3.3(c) show the bifurcation diagrams of the uniform solutions for case 1. The point P_1 where the uniform solution changes its (in)stability is shifted to the right or to the left, which depends on the value of c. For $c < c_P$ (weakly coupled), P_1 is shifted to the left approaching the turning point as c decreases. Moreover, when $c = 0$ (uncoupled), P_1 is at the left turning point. The eigenvalue (3.8) that determines the linear stability is a function of c for $c < c_P$. On the other hand, P_1 is independent of c for $c \geq c_P$ (strongly coupled).

The same mechanism also occurs for case 2 with the (in)stability change at point P_0, see Figs. 3.3(b), 3.3(d), and 3.2(a). In case 2, P_0 is shifted to the right when c is getting smaller and it is shifted to the left when c is getting larger. Note that, for both cases, we have bistability of uniform solutions for $P_1 \leq P \leq P_0$.

3.3 Localized solutions and Snaking

Discrete optical cavity equation (3.1) admits localized solutions, namely onsite and intersite solutions that bifurcate from the uniform solutions at point P_0. Localized solution is formed by combining two stable uniform states, i.e., "upper" and "lower" branches, back to back.

3.3.1 Snaking

By applying numerical continuation for varying P, one can obtain the bifurcation diagrams for onsite and intersite solutions as shown in Fig. 3.4.

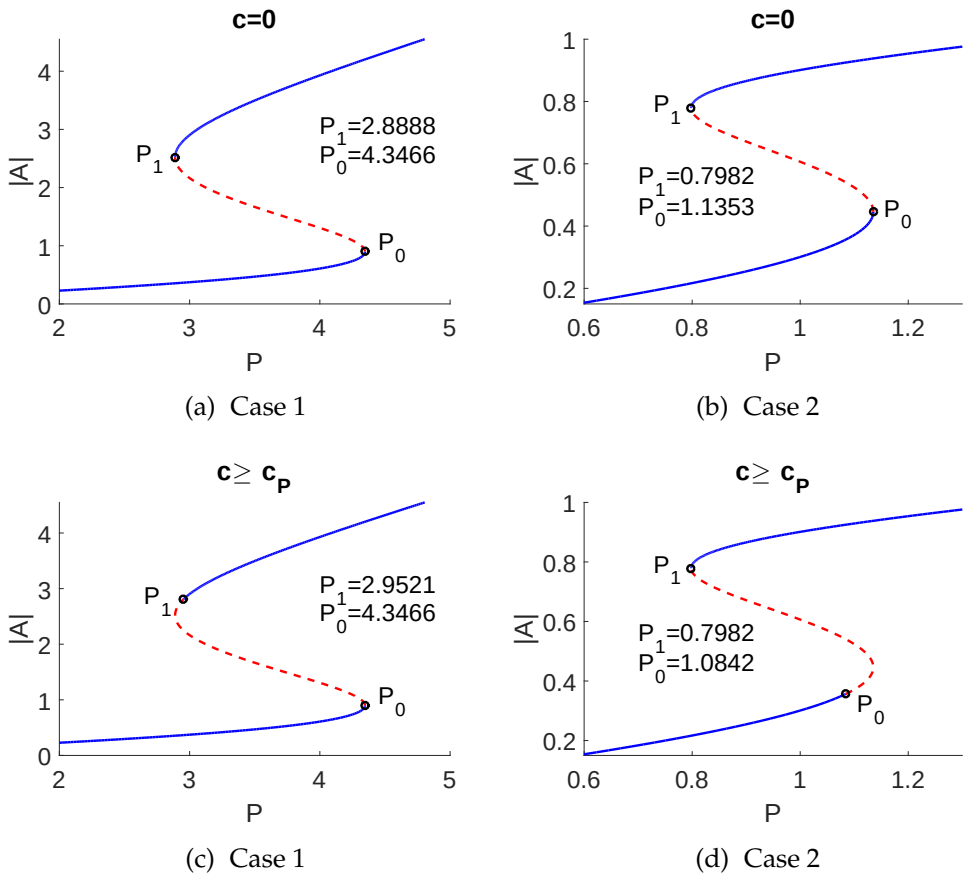

(a) Case 1 (b) Case 2

(c) Case 1 (d) Case 2

Figure 3.3. Bifurcation diagrams of the uniform solutions and their linear stability. The blue solid and red dashed lines in (c)-(f) represent stable and unstable solutions. Note that there is a stability shift past the turning points as c increases.

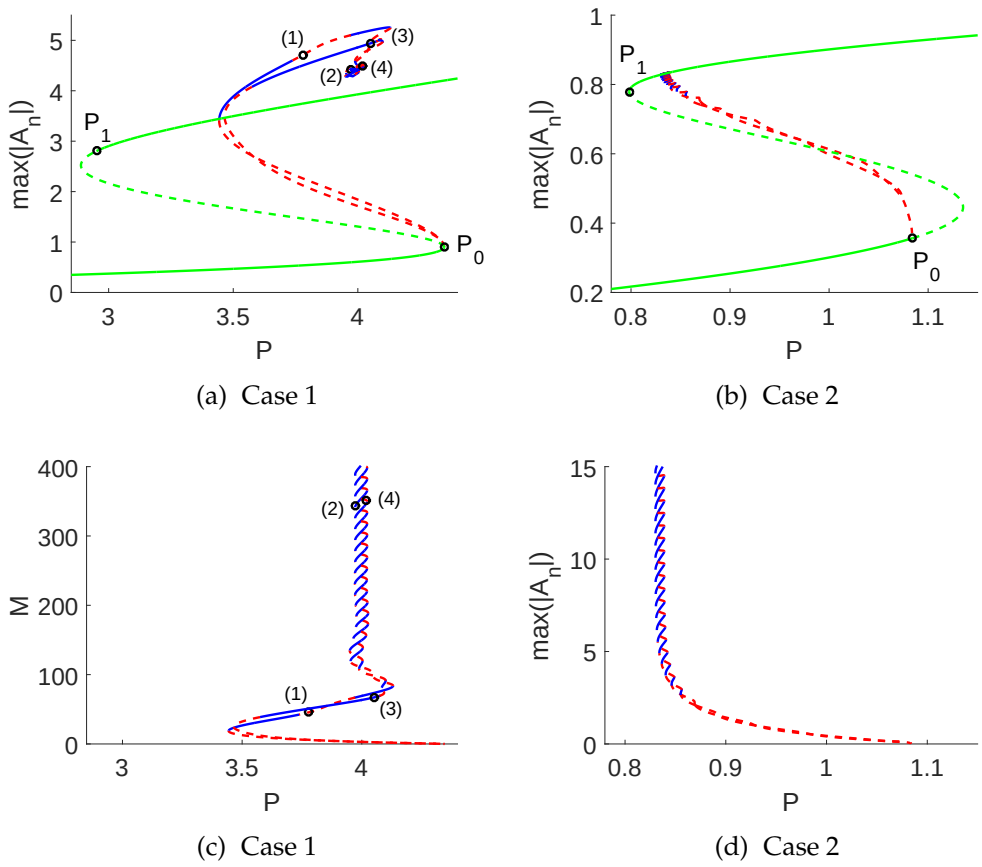

(a) Case 1 (b) Case 2

(c) Case 1 (d) Case 2

Figure 3.4. Bifurcation diagrams for case 1 and 2 for $c = 1$. The blue solid and red dashed lines represent stable and unstable solutions, respectivley. The green solid/dashed line represents uniform solution. The corresponding solutions at the indicated points in panel (a) and (c) are plotted in Fig. 3.5.

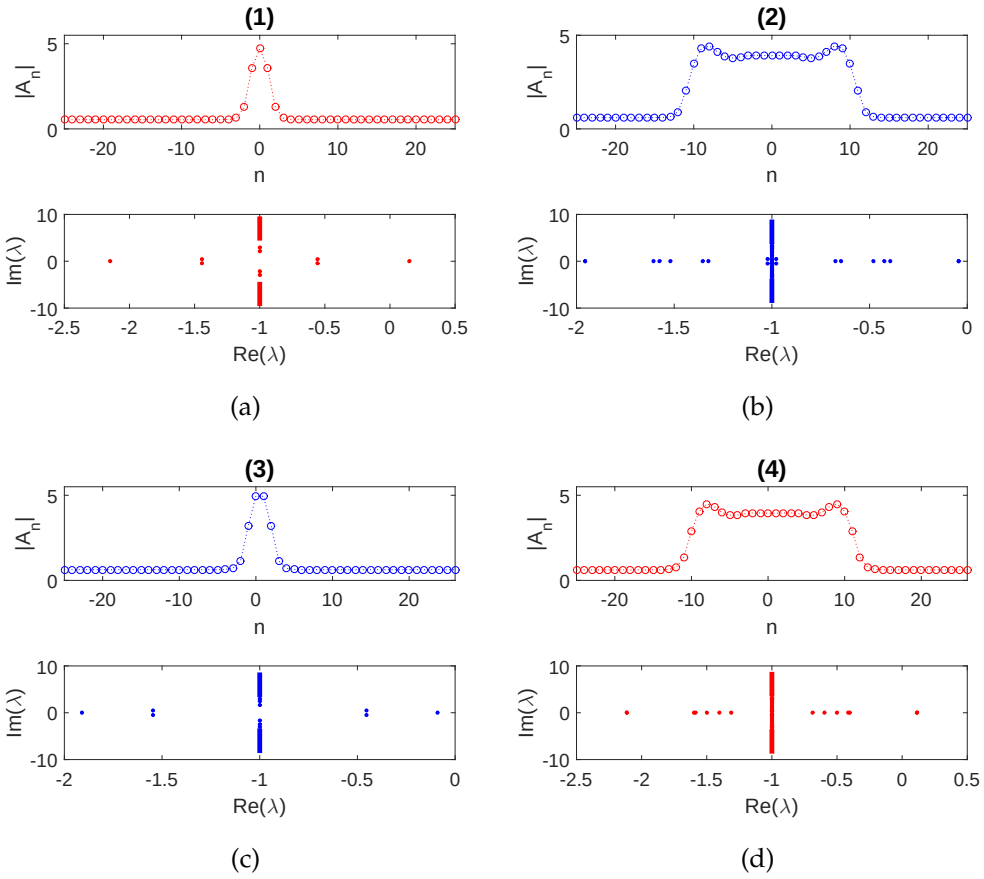

Figure 3.5. Plot of the onsite and intersite solution profiles on the bifurcation diagram in Figs. 3.4(a) and 3.4(c) and their spectrum in the complex plane. (a)-(b) and (c)-(d) depict onsite and intersite solutions, respectively.

We also introduce the “norm”, i.e.,

$$M = \sum_n \left(|A_n - A_\infty|^2 \right), \tag{3.10}$$

which we refer to as the mass of the soliton [96, 97]. By plotting the bifurcation diagrams in Figs. 3.4(a) and 3.4(b) in terms of the soliton mass instead, homoclinic snaking for onsite and intersite solutions are clearly seen in Figs. 3.4(c) and 3.4(d).

Figure 3.5 shows onsite and intersite localized solutions of the diagram in Fig. 3.4(c) for several values of P. As the bifurcation parameter P is being varied, the norm M will increase. The “upper" state of the localized solution will invade the “lower" state. Figure 3.6 shows the bifurcation diagrams of snaking for varying c for

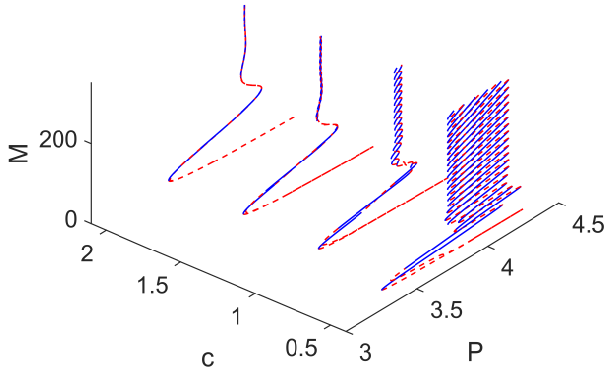

Figure 3.6. Bifurcation diagrams of case 1 for varying c.

case 1. One can see that the pinning region is getting wider as the coupling strength c decreases (weakly discrete). On the contrary, we do not have any snaking as $c \to \infty$. Furthermore, onsite and intersite solutions merge in the continuum limit.

3.3.2 ⋐-shaped isolas

One interesting phenomenon from the snaking in optical cavities equation is that when the pinning region expands as c decreases, at some point one will reach a regime where the background (uniform state) of the localized state ceases to exist. This phenomenon causes attachment or detachment process around the saddle-node bifurcations in the snaking branches. As an impact of this phenomenon, ⋐-shaped isolas will be formed when we vary the control parameter, i.e., P. Figure 3.7 shows the formation mechanism of the ⋐-shaped isolas present in case 1 as c is being varied. One can see that, the ⋐-shaped isolas are formed around $c \approx 0.39$ for case 1.

3.4 Pinning regions analysis

In this section, we analyze and discuss the pinning region and its approximation for case 1 and 2 when we vary the coupling strength c.

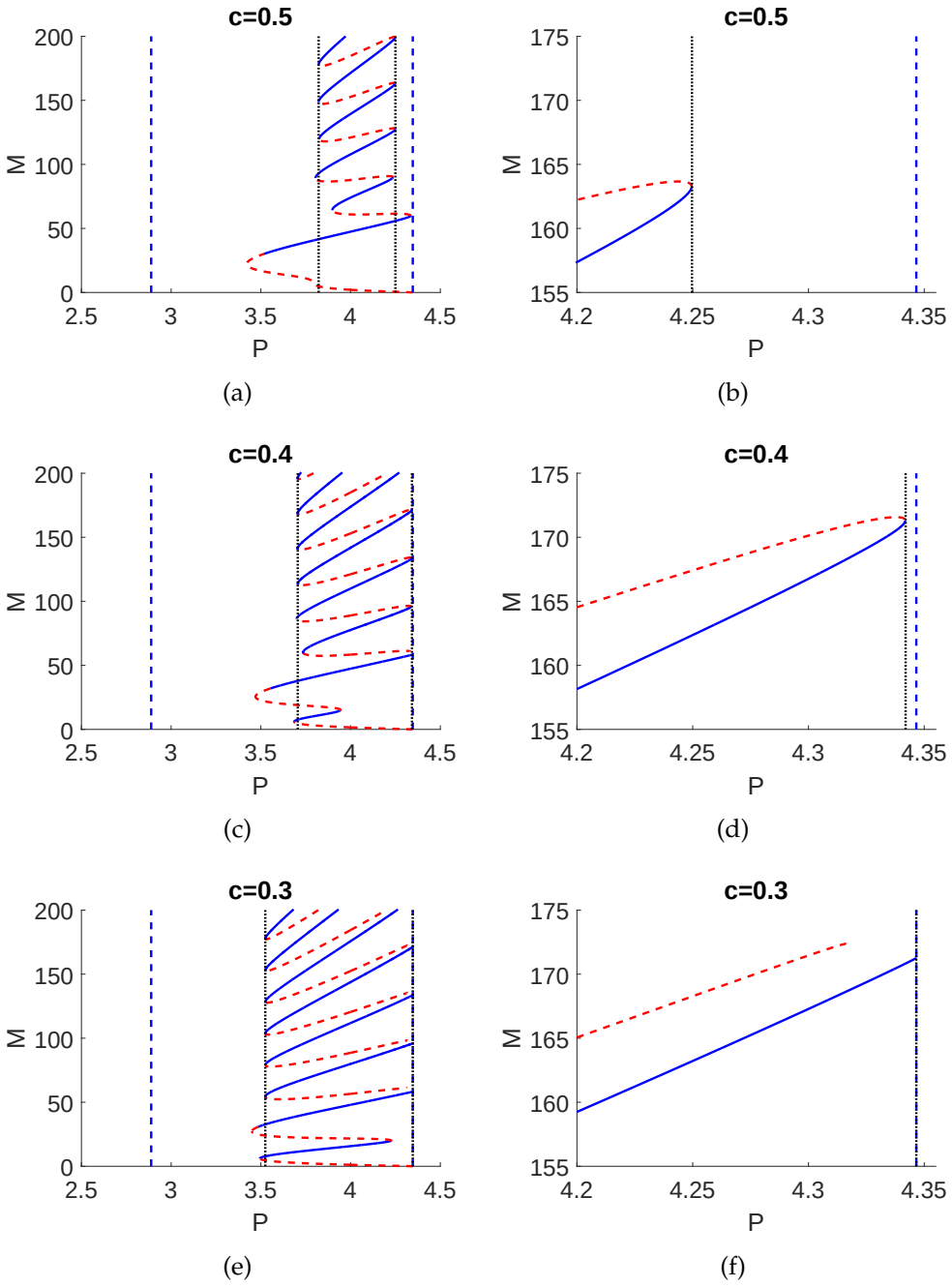

Figure 3.7. The occurence of ⋐-shaped isolas for case 1 (onsite solutions) when c is being varied.

3.4.1 Pinning region

It is important to note that pinning regions are bounded by turning points. Hence, the boundaries of the pinning regions can be computed from solving the extended system [48]

$$\begin{pmatrix} \partial_t A_n \\ \mathcal{L}\varphi \\ \|\varphi\| \end{pmatrix} = \begin{pmatrix} 0 \\ 0 \\ 1 \end{pmatrix}, \tag{3.11}$$

where φ is an eigenvector of the Jacobian $\mathcal{L}$, that corresponds to the largest eigenvalue being zero. By using Eq. (3.11), one can compute the left and right pinning regions without calculating the whole snaking. However, it needs a good initial condition to obtain the turning points, which is the boundary of the pinning region. Note that in the anti-continuum limit, the turning points of the uniform solutions also satisfy the extended system in Eq. (3.11).

Figures 3.8 and 3.9 show the pinning regions for case 1 and 2. Herein, we only simulate the pinning regions for varying c.

Figure 3.8(a) shows the pinning region when we vary c for case 1. One can see that the pinning region increases when c decreases. At $c \approx 0.39$, the right boundary of the pinning region reaches the right saddle point of the uniform solutions, i.e., the ⋐-shaped isolas are formed. On the contrary, the pinning region shrinks when c is getting larger as the onsite and intersite solutions become the same in the continuum limit.

Figure 3.9 shows the pinning region when we vary c for case 2. The main difference with case 1 is that there is no formation of ⋐-shaped isolas.

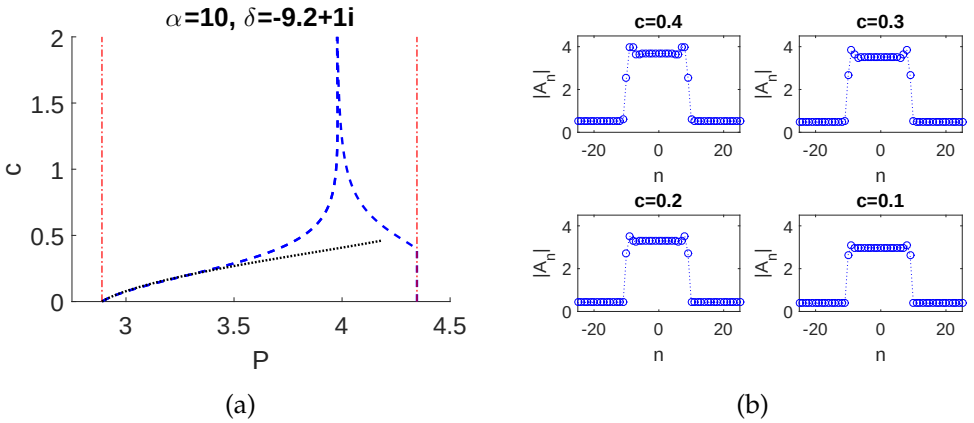

Figure 3.8. (a) The pinning region for case 1 and (b) their solution profiles at $P = 4$ for different values of c. The blue dashed lines indicate boundaries of the pinning region. The red dotted-dashed line indicates the turning point of the uniform solution. The black dotted line indicates the one-active site approximation of the pinning regions.

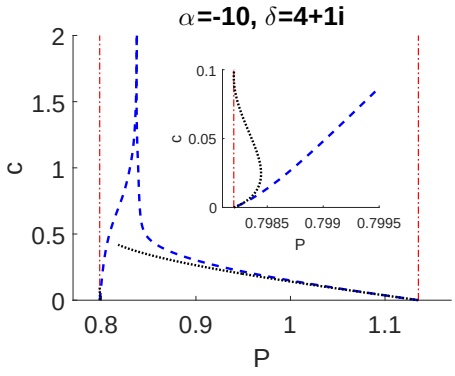

Figure 3.9. The same as Fig. 3.8(a), but for case 2.

3.4.2 One-active site

One can see that when we vary P, there is effectively only one node that is "active" at the fronts between the two states of the uniform solutions as shown in Fig. 3.5. By using the assumption that only three nodes involve in the dynamics as we vary P, write [61, 83]

$$A_{n-1} = u_1, \quad A_n = v, \quad \text{and} \quad A_{n+1} = u_2, \tag{3.12}$$

where u_1 and u_2 are uniform states (background states) on the upper and lower branch of Fig. 3.3 and v is the active node. By substituting (3.12) into the time

independent solutions of Eq. (3.2), we obtain

$$F_a(v) := \delta v + \frac{\alpha|v|^2}{1+|v|^2} v + c\,(u_1 + u_2 - 2v) - P = 0. \tag{3.13}$$

For the assumption to be valid, the solutions should be "discrete" enough, i.e., weakly coupled. In general, Eq. (3.13) can have one or three real solutions which is related to snaking. Two of the roots will disappear in a saddle-node bifurcation, which will correspond to a pinning region boundary. In Fig. 3.10, we show the one-active site function for case 1 and 2. The three roots are indicated in Fig. 3.10. The pinning region boundary is the condition when O and X or O and $\triangle$ merge. To be precise, the coalescence of points O and X or O and $\triangle$ corresponds to the left and right boundaries of the pinning regions, respectively. The mechanism for collisions is the same as that for the uniform solutions in Figs. 3.1(a) and 3.1(b).

Figures 3.8 and 3.9 show the comparison between the numerical results from (3.2) and the one-active site approximation (3.13).

Figure 3.8(a) shows that the one-active site approximation is good for small c. One can see, the solution profile for large c has more than one-active node on the "upper" state, see Fig. 3.8(b). In this case, the one-active site assumption is no longer valid.

The comparison between the numerical results and the one-active approximation for case 2 are shown in Fig. 3.9. The inset in Fig. 3.9 indicates the most important trait of the comparison. The simulation results show that the one-active site approximation gives better results for small c. Additionally, the one-active site approximation will also give better results if the pinning boundary is relatively far from the turning point of the uniform solution. One also can say that a one-active site approximation gives a good result when "upper" and "lower" states from the localized solutions are relatively flat (uniform) or weakly coupled and only one-active node connects them.

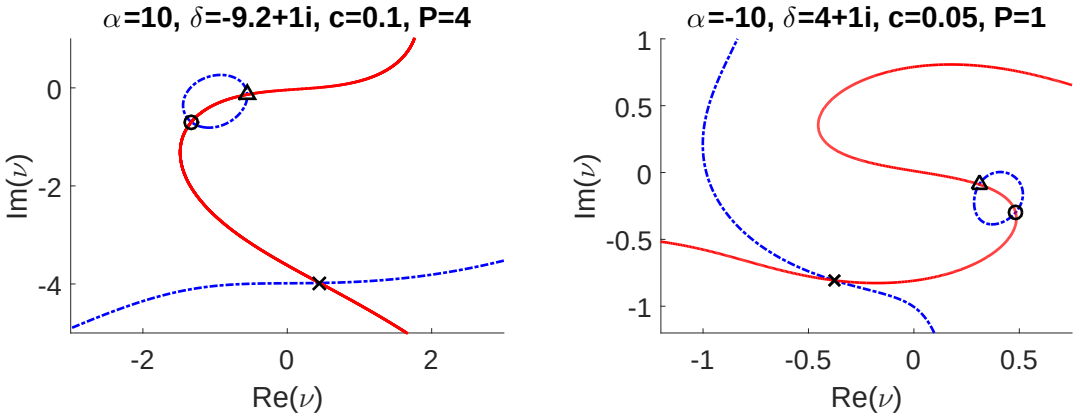

(a) Case 1 (b) Case 2

Figure 3.10. One-active site function for case 1 and 2. Blue dotted-dashed line represents real part of the one-active site function $Re(F_a)$. Red solid line represents imaginary part of the one-active site function $Im(F_a)$. Points O, X, and $\triangle$ represent the solutions of the one-active site function (3.13).

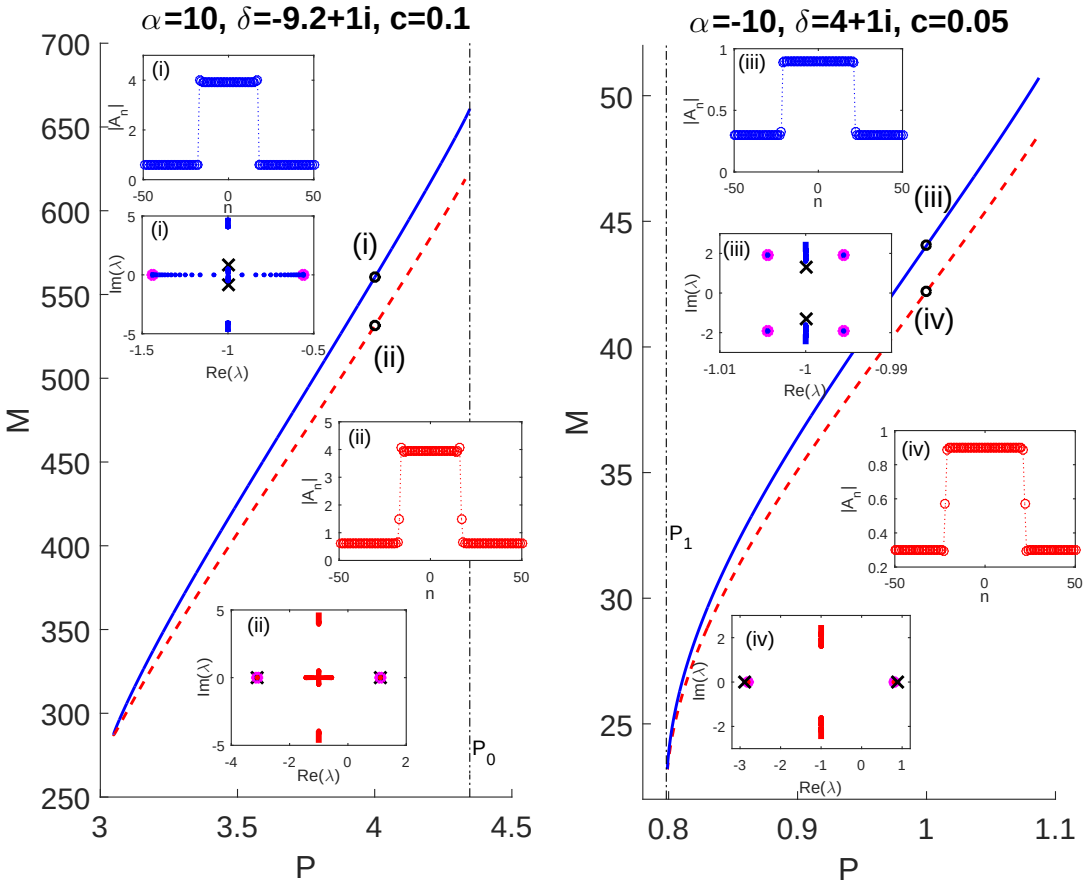

Figure 3.11. Left and right panles are bifurcation diagrams for case 1 and 2, respectively. The insets show localized solutions and their spectrum obtianed from Eq. (3.5) and from Eq. (3.15) shown in circles and crosses, respectively. Magenta cirle represents the maximum and minimum of real part eigenvalues from Eq. (3.2) and (3.13), respectively.

Next, the critical eigenvalue of localized solutions in the pinning region can also be approximated by our one-active site approximation. This could be obtained by considering the dynamics of Eq. (3.13), i.e.,

$$-i\,v_t = F_a(v). \tag{3.14}$$

Let $\tilde{v} = \tilde{v}_R + i\tilde{v}_I$ is a solution of the one-active site function (3.13). Linearising (3.14) around $\tilde{v}$, by writing $v = \tilde{v} + \epsilon(v_r + iv_i)e^{\lambda t}$ for small $|\epsilon|$ will yield the eigenvalue problem

$$\lambda \begin{pmatrix} v_r \\ v_i \end{pmatrix} = \begin{pmatrix} s_{11} & s_{12} \\ s_{21} & s_{22} \end{pmatrix} \begin{pmatrix} v_r \\ v_r \end{pmatrix}, \tag{3.15}$$

where

$$\begin{aligned} s_{11} &= -\delta_i - m_{11}(\tilde{v}_R, \tilde{v}_I), & s_{12} &= -\delta_r - 2c - m_{12}(\tilde{v}_R, \tilde{v}_I), \\ s_{21} &= \delta_r + 2c - m_{21}(\tilde{v}_R, \tilde{v}_I), & s_{22} &= -\delta_i - m_{22}(\tilde{v}_R, \tilde{v}_I), \end{aligned}$$

m_{11}, m_{12}, m_{21}, and m_{22} are giving in (3.6). We can simply obtain the eigenvalues

$$\lambda(P) = \frac{1}{2}\left(s_{11} + s_{22} \pm \sqrt{(s_{11} - s_{22})^2 + 4s_{12}s_{21}}\right). \tag{3.16}$$

The inset in Fig. 3.11 shows the numerically computed spectrum of the localized solutions and our approximations, where a good comparison is obtained. However, our approximation of critical eigenvalues do not coincide with the numerical results when the critical eigenvalues are from the background states, rather than from the front of the localized solution, as we can see in the insets (i) and (iii) in Fig. 3.11. Generally, the one-active site approximation is a good approximator to determine the stability of a localized solution in weakly coupled systems.

3.5 Pinning regions for varying $Re(\delta)$ and $Im(\delta)$

Figure 3.12 shows the pinning regions and their solution profiles (case 1 only) for varying $Im(\delta)$ and $Re(\delta)$. It also shows the comparison between the numerical results from Eq. (3.2) and the one-active site approximation (3.13).

Figure 3.12(a) shows a comparison of the pinning region for varying $Im(\delta)$. Herein, c is taken to be small, which is $c = 0.1$, because the one-active site approximation is good for a weak coupling condition. As we can see, the one-active site approximation gives good agreement for large $Im(\delta)$. The approximation starts to get farther away from the numerics at $Im(\delta) \approx 0.5$ as we decrease $Im(\delta)$. The approximation fails because the "upper" state from the localized solution starts to form a "non-uniform" state, see Fig. 3.12(c).

Figure 3.12(b) shows a comparison of the pinning region for varying $Re(\delta)$. As one can see, the one-active site approximation gives good agreement for smaller $Re(\delta)$. The approximation starts to have a significant difference at $Re(\delta) \approx -8$ as we increase $Re(\delta)$. This occurs because the "upper" state starts to form a "non-uniform" state when $Re(\delta)$ increases as shown in Fig. 3.12(d).

For case 2, the comparison between the numerical results and the one-active approximation for varying $Im(\delta)$ and $Re(\delta)$ are shown in Figs. 3.12(e) and 3.12(f), respectively.

To sum up, the simulation results show that the one-active site approximation gives good agreement for small c, large $Im(\delta)$, and small $Re(\delta)$. One also can say that it gives a good result when the "upper" and "lower" states of localized solutions are relatively uniform, weakly coupled, and only have one front that connects them.

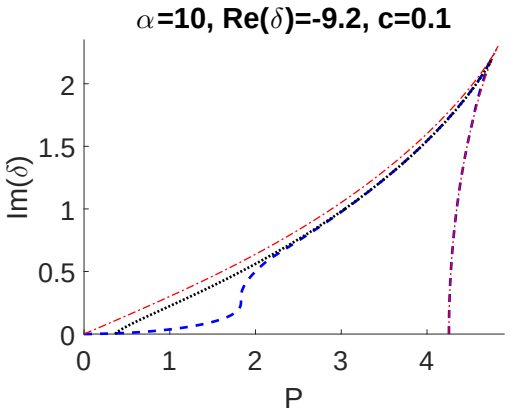

(a) Case 1

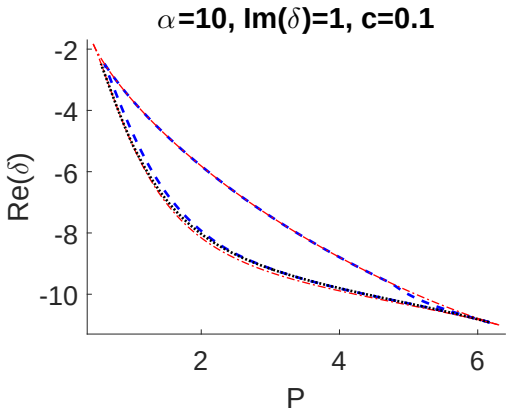

(b) Case 1

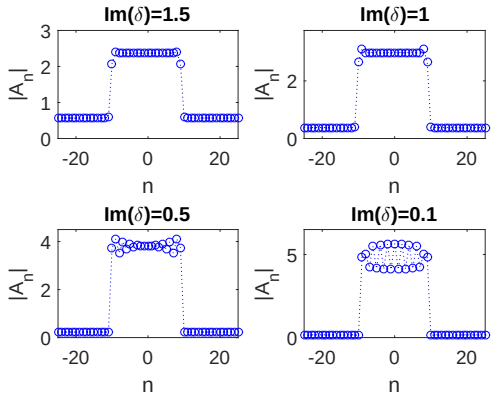

(c) Case 1

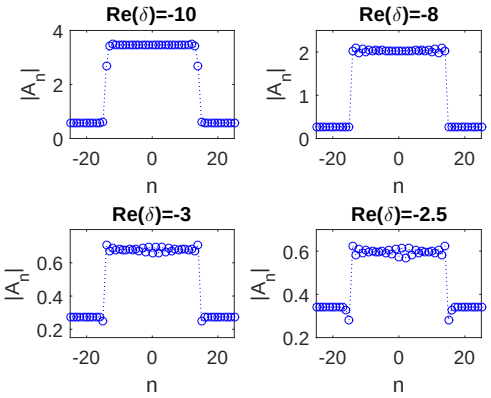

(d) Case 1

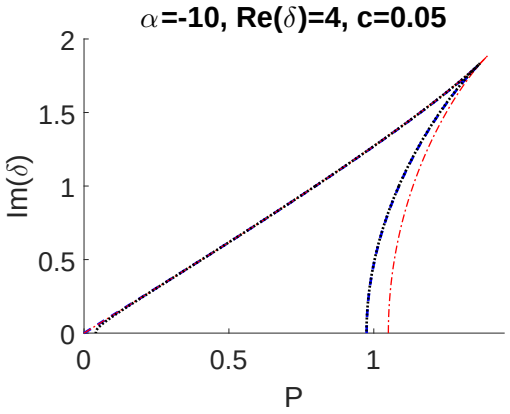

(e) Case 2

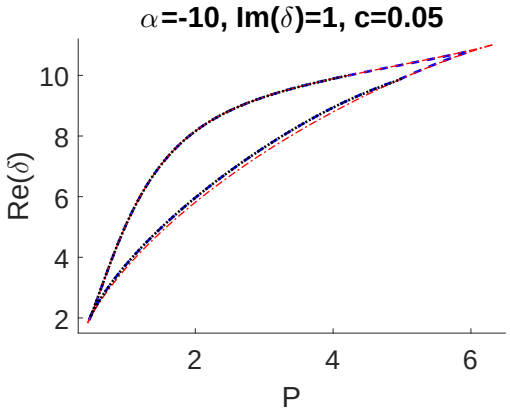

(f) Case 2

Figure 3.12. Panels (a), (b), (e), and (f) are the same as Figs. 3.8(a) and 3.9, but varying *Re*(δ) and *Im*(δ). Panels (b), (d) are solution profiles for different values of *Im*(δ) and *Re*(δ), respectively.

3.6 Conclusions

We have presented the study of time-independent solutions of the discrete optical cavities in saturable nonlinearity and their stability. We found that bifurcations of localized states from the uniform state can depend on the coupling strength between the arrays. The stability and turning points of the uniform solutions can be determined semianalytically. By using numerical continuation, we computed the pinning regions of localized solutions, within which the bifurcation diagrams form snaking structures when a parameter is being varied. Numerical simulations also showed the appearance of $\Subset$-shaped isolas in the bifurcation diagrams.

A one-active site approximation to analyze and approximate the pinning region boundary has been proposed. We also showed that it can give a good approximation for localized solutions and the critical eigenvalues, especially for weakly coupled systems.

Applications of the one-active site approximation in higher dimensional systems will be reported elsewhere.

Chapter 4

Snakes in square, honeycomb and triangular lattices

4.1 Introduction

In recent years, a great deal of interest has been focussed on the study of homoclinic snaking [94] appearing in pattern formations in nonlinear systems, such as those in the Swift-Hohenberg equations [19–21], cellular buckling [53], neuronal model [3, 62], and optical systems [44, 96–98], leading to a rather complete understanding of their properties and mechanism of formation in the lower dimension. Homoclinic snaking has also been observed in different experiments, e.g., in magnetic fluids [65], liquid crystals [14, 51], shell bucklings [87], optical cavities [88], and semiconductor optical systems [6]. Generally, localized solutions may be present due to the existence of bistability regimes between homogeneous and periodic states or between homogeneous states themselves. We can obtain a localized state when we combine back to back two different states, which are connected by fronts [76].

Higher dimensional snaking has been studied as well [2, 66, 90]. Using the planar Swift-Hohenberg equation, several numerical observations show exotic solutions, such as stripes, localized spots and hexagon patches [30, 52, 66, 79]

and localized radial solutions [64, 69]. Localized square patterns have also been observed in the same equation with an additional nonlinear gradient term [80]. Planar neuronal models also exhibit similar exotic solutions [77]. Patchwork quilt state, i.e., regular triangles, [47] is foreseen in bistable systems with the symmetry $u \to -u$. Snaking involving various superpatterns [36, 55] is also anticipated. Snaking of localized structures called convectons in three-dimensional doubly diffusive convections has also been studied [8, 9].

All in all, details of the snaking behavior are rather more involved in higher dimensional case, such as overlapping pinning regions, complications that involve Maxwell points, and growing patterns by nucleating individual structure which break and recover the basic symmetry of the state [66]. Even a good qualitative picture of those behaviors is still an open problem [58].

This chapter provides a further step towards understanding the problem. However, rather than considering spatially continuous systems, we study a discrete one as it may provide a better control over, e.g., the patterns of localized states that may appear by determining the lattice types. In this work, we consider square, honeycomb, and triangular lattices. Our main finding is that the complexity and width of the snaking diagrams depend on the number of "fronts" admitted by the lattice patterns.

Homoclinic snaking is also observed in spatially discrete systems [24, 25, 61]. While in continuous systems snaking is caused by pinning between fronts and the underlying oscillatory states, in discrete setups it is due to the pinning of fronts and the imposed lattices, i.e., in continous equations homoclinic snaking occurs when localized states add "rolls" at the fronts, in discrete systems they add "cell". Homoclinic snaking in two-dimensional discrete systems has also been numerically studied in [24, 86], where it was shown that bifurcation diagrams of

localized solutions can exhibit a complicated behavior, which is not clearly well understood yet.

In this work, we consider a two-dimensional discrete Allen-Cahn equation with cubic and quintic nonlinearity [86]. The equation can be considered to come from the two-dimensional discrete nonlinear Schrödinger equation

$$i\dot{\psi}_n + c\Delta\psi_n + 2|\psi_n|^2\psi_n - |\psi_n|^4\psi_n = 0, \tag{4.1}$$

where $\psi_n(t)$ is an array of complex field and Δ is a Laplacian operator of the nearest neighbour differences. By substituting $\psi_n(t) = u_n e^{-i\mu t}$, where u_n is real stationary field into equation (4.1), we obtain

$$\mu u_n + c\Delta u_n + 2u_n^3 - u_n^5 = 0, \tag{4.2}$$

which is the time-independent discrete Allen-Cahn equation. In this chapter, we study homoclinic snaking boundaries of the system when the coupling between lattices is weak. In particular, we consider three different types of lattices, i.e., square, honeycomb, and triangular, which to our best knowledge have not been studied in the context of homoclinic snaking. Another main result is that we classify all the relevant structures causing saddle-node bifurcations that form the boundaries of the pinning regions.

The chapter is constructed as follows. The two-dimensional discrete Allen-Cahn equation is discussed in Section 4.2. We also discuss uniform states and their stability in the section. In Section 4.3, localized states and their homoclinic snaking for square, honeycomb, and triangular lattices are being discussed and calculated. In Section 4.4, we discuss active-cell approximations of the saddle-node bifurcations and details of the snaking structures reported in Section 4.3. Section 4.5 is our conclusions.

4.2 Mathematical model and uniform state

In this study, we consider the two-dimensional (2D) discrete Allen-Cahn equation, which is given by

$$\dot{u}_{n,m} = \mu u_{n,m} + 2u_{n,m}^3 - u_{n,m}^5 + c^{\square}\Delta^{\square}u_{n,m}, \tag{4.3}$$

where $u_{n,m}$ is a real stationary field defined on 2D integer lattice, μ is a real bifurcation parameter, $c^{\square}$ is the coupling strength of the nearest-cell, and $\Delta^{\square}$ is a discrete Laplacian operator on the 2D integer lattices $\mathbb{Z}^2$. We consider three lattice types, namely,

- Square lattice :

$$\begin{aligned} c^{\square}\Delta^{\square}u_{n,m} &= c^{+}\Delta^{+}u_{n,m} \\ &= c^{+}\Big(u_{n+1,m} + u_{n-1,m} + u_{n,m+1} + u_{n,m-1} - 4u_{n,m}\Big), \end{aligned} \tag{4.4}$$

- Honeycomb lattice :

$$\begin{aligned} c^{\square}\Delta^{\square}u_{n,m} &= c^{\curlywedge}\Delta^{\curlywedge\pm}u_{n,m} \\ &= c^{\curlywedge}\Big(u_{n+1,m} + u_{n-1,m} + u_{n,m\pm1} - 3u_{n,m}\Big), \end{aligned} \tag{4.5}$$

  where $\Delta^{\curlywedge+}$ and $\Delta^{\curlywedge-}$ correspond to the case when $n+m$ is even or odd, respectively,

- Triangular lattice :

$$\begin{aligned} c^{\square}\Delta^{\square}u_{n,m} &= c^{\divideontimes}\Delta^{\divideontimes}u_{n,m} \\ &= c^{\divideontimes}\Big(u_{n+1,m} + u_{n-1,m} + u_{n,m+1} + u_{n,m-1} + u_{n-1,m+1} + u_{n+1,m-1} \\ &\quad -6u_{n,m}\Big). \end{aligned} \tag{4.6}$$

In Fig. 4.1, we transform honeycomb and triangular lattices into square domain, i.e., brick and slanted-triangular lattices for the purpose of computation and plotting.

In particular, we study the time-independent solution of equation (4.3), i.e.,

$$\dot{u}_{n,m} = 0. \tag{4.7}$$

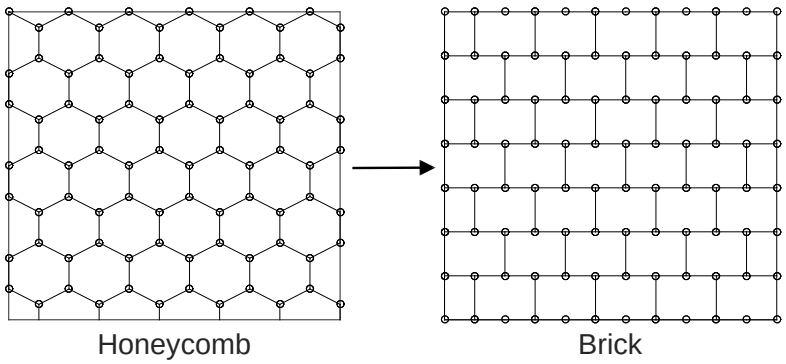

(a)

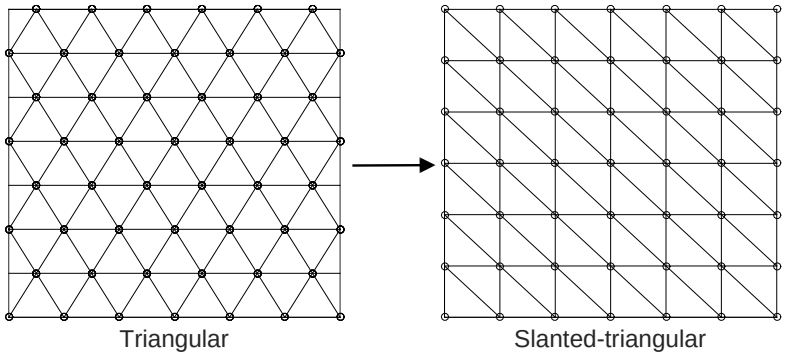

(b)

Figure 4.1. Honeycomb and triangular lattices. We transform the lattices into brick and slanted-triangular ones for the sake of computations and plotting in this chapter.

To determine the linear stability of a solution $\tilde{u}_{n,m}$, we write

$$u_{n,m} = \tilde{u}_{n,m} + \epsilon e^{\lambda t} \hat{u}_{n,m}. \tag{4.8}$$

By substituting (4.8) into (4.3) and linearizing around $\epsilon = 0$, we obtain the linear equation

$$\lambda \hat{u}_{n,m} = \mathcal{L} \hat{u}_{n,m}, \tag{4.9}$$

where

$$\mathcal{L} = \mu + 6\tilde{u}_{n,m}^2 - 5\tilde{u}_{n,m}^4 + c^{\square}\Delta^{\square}. \tag{4.10}$$

A uniform solution is said to be stable when all $\lambda \leq 0$ and unstable when $\exists \lambda > 0$.

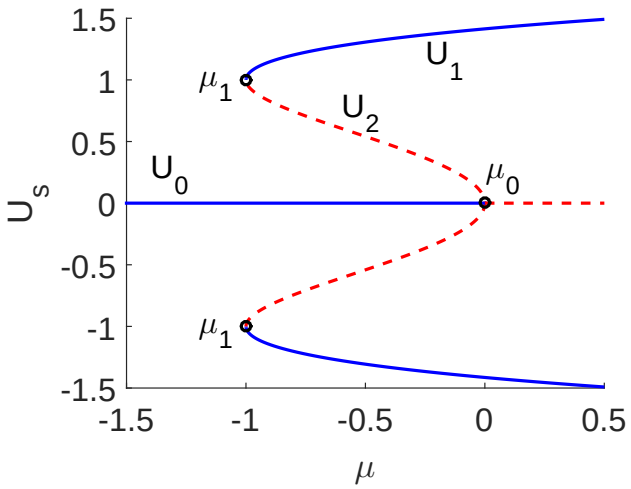

Figure 4.2. Uniform solution of the discrete Allen-Cahn equation. The blue solid and red dashed lines indicate stable and unstable solutions, respectively.

The 2D discrete Allen-Cahn equation (4.3) exhibits the same uniform solution as the one-dimensional case that has been studied by Taylor and Dawes in [86], which is given by

$$0 = \mu U_s + 2U_s^3 - U_s^5, \tag{4.11}$$

that can be solved to yield

$$U_0 = 0 \quad \text{and} \quad U_{1,2}^2 = 1 \pm \sqrt{1+\mu}. \tag{4.12}$$

We plot the solutions for varying μ in Fig. 4.2. To determine the linear stability of the uniform solutions $\tilde{u}_{n,m} = U_s$, where $s = 0,1,2$, one has $\hat{u}_{n,m} = e^{i(kn+lm)}$, where k and l are the wave number of the perturbations in the n and m directions, from which we obtain for the square and triangular lattices the dispersion relation

$$\lambda(k,l) = \mu + 6U_s^2 - 5U_s^4 + \gamma^{\square}(k,l), \quad \square = +, \ast, \tag{4.13}$$

where

$$\begin{aligned} \gamma^{+}(k,l) &= 2c^{+}\left(\cos(k) + \cos(l) - 2\right), \\ \gamma^{\ast}(k,l) &= 2c^{\ast}\left(\cos(k-l) + \cos(k) + \cos(l) - 3\right), \end{aligned} \tag{4.14}$$

respectively. As for the honeycomb lattice, we need to rewrite equation (4.3) into

$$\begin{aligned}\dot{\psi}_{n,m} &= \mu\psi_{n,m} + 2\psi_{n,m}^3 - \psi_{n,m}^5 + c^\curlywedge\left(\varphi_{n,m} + \varphi_{n,m-1} + \varphi_{n-1,m} - 3\psi_{n,m}\right),\\ \dot{\varphi}_{n,m} &= \mu\varphi_{n,m} + 2\varphi_{n,m}^3 - \varphi_{n,m}^5 + c^\curlywedge\left(\psi_{n,m} + \psi_{n,m+1} + \psi_{n+1,m} - 3\varphi_{n,m}\right).\end{aligned} \tag{4.15}$$

The perturbation ansatz in this case would be

$$\begin{pmatrix}\psi_{n,m}\\ \varphi_{n,m}\end{pmatrix} = U_s + \begin{pmatrix}\hat{\psi}_{n,m}\\ \hat{\varphi}_{n,m}\end{pmatrix}\epsilon e^{\lambda t}. \tag{4.16}$$

By substituting (4.16) into (4.15) and linearizing around $\epsilon = 0$, we obtain the eigenvalue problem

$$\lambda\begin{pmatrix}\hat{\psi}_{n,m}\\ \hat{\varphi}_{n,m}\end{pmatrix} = \begin{pmatrix}\mu + 6U_s^2 - 5U_s^4 - 3c^\curlywedge & c^\curlywedge\,\xi^-(k,l)\\ c^\curlywedge\,\xi^+(k,l) & \mu + 6U_s^2 - 5U_s^4 - 3c^\curlywedge\end{pmatrix}\begin{pmatrix}\hat{\psi}_{n,m}\\ \hat{\varphi}_{n,m}\end{pmatrix}, \tag{4.17}$$

where

$$\xi^\pm(k,l) = 1 + \cos(k) + \cos(l) \pm i\left(\sin(k) + \sin(l)\right). \tag{4.18}$$

Hence, we have the dispersion relation for the honeycomb lattice, i.e.,

$$\lambda(k,l) = \mu + 6U_s^2 - 5U_s^4 - 3c^\curlywedge \pm c^\curlywedge\sqrt{2\left(\cos(k-l) + \cos(k) + \cos(l)\right) + 3}. \tag{4.19}$$

The points μ_s, $s = 0,1$ is Fig. 4.2 denote the stability change of U_s. They correspond to a condition when the maximum of the dispersion relation (4.13) and (4.19) touch the k,l plane, which is attained at $k = l = 0$ for all of the lattice types. One can note that we have bistability interval $\mu \in [\mu_1, \mu_0]$ for the uniform solutions, see Fig. 4.2. Furthermore, the bifurcation diagram and the stability of the uniform solution in Fig. 4.2 is the same as those in the one-dimensional model [24, 86].

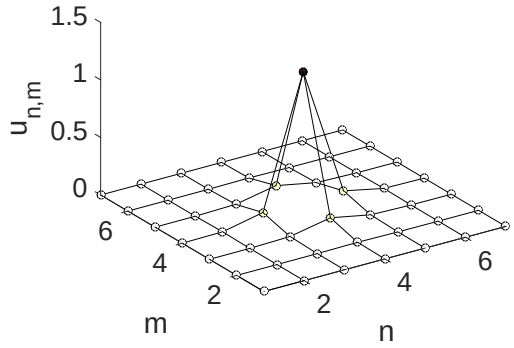

(a) Site-centred solution of square lattice

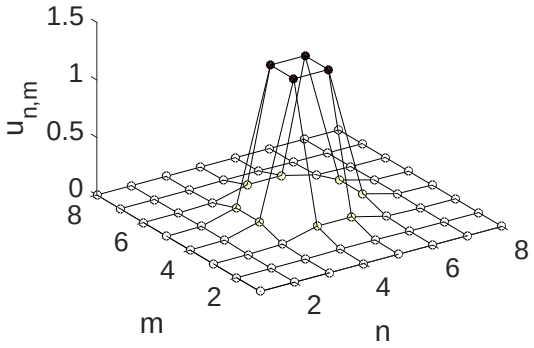

(b) Bond-centred solution of square lattice

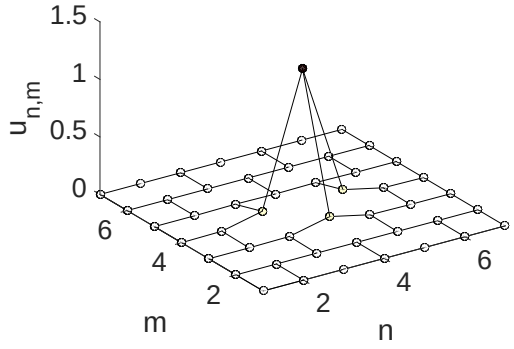

(c) Site-centred solution of honeycomb lattice

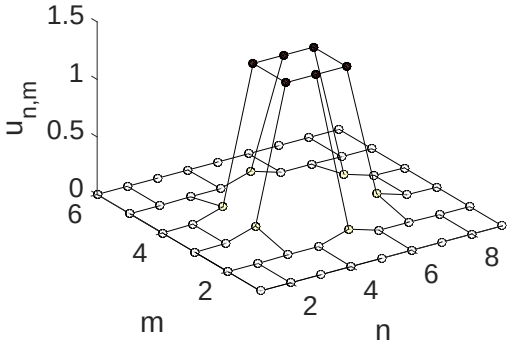

(d) Bond-centred solution of honeycomb lattice

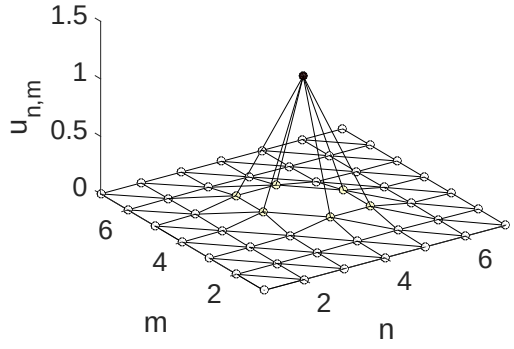

(e) Site-centred solution of triangular lattice

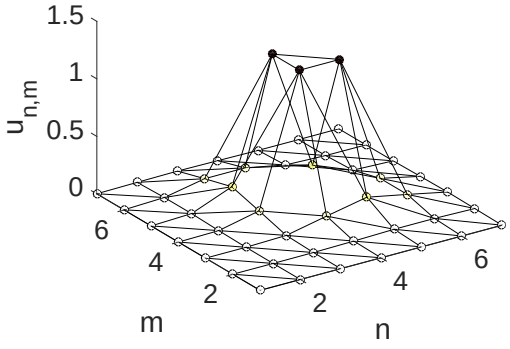

(f) Bond-centred solution of triangular lattice

Figure 4.3. Structures of fundamental localized solutions for $c^+ = c^\curlywedge = c^\divideontimes = 0.05$ and $\mu = -0.6$.

4.3 Localized solution and snaking

The discrete Allen-Cahn equation (4.3) admits localized solutions that bifurcate from the uniform solution U_0 at point μ_0. We are particularly interested in

fundamental localized solutions, i.e., site-centred and bond-centred solutions, which are the counter-part of onsite and intersite solutions in the one-dimensional case. They are formed by two bistable states from the uniform solutions, i.e., the non-zero state U_1 as the "upper" state and zero state U_0 as the "background" state.

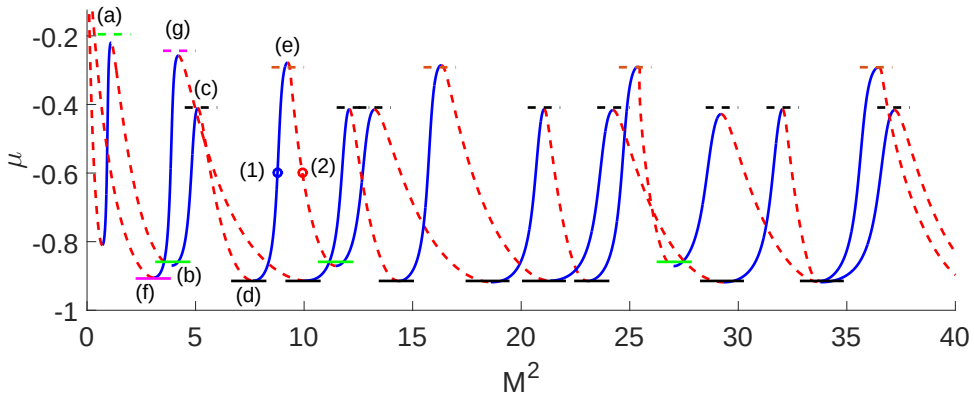

(a) $c^+ = 0.05$

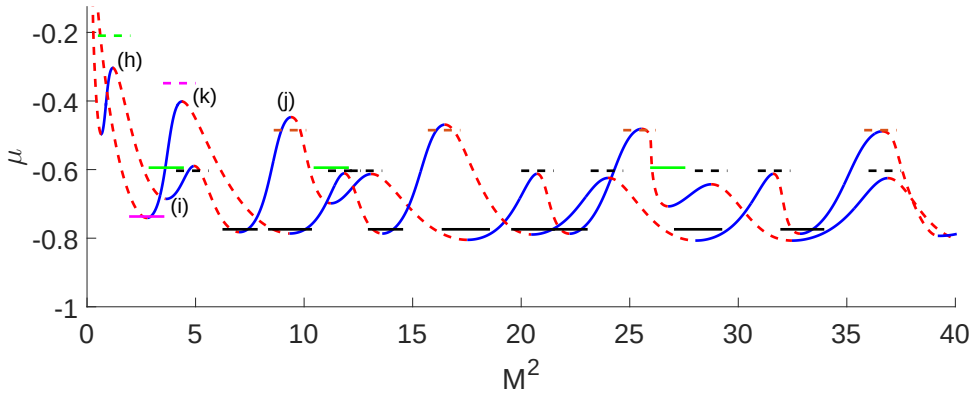

(b) $c^+ = 0.15$

Figure 4.4. Panels (a) and (b) show bifurcation diagrams for square lattice. The solid and dashed lines around turning points of the snaking curves are the approximation of "lower" and "upper" saddle-node bifurcations, respectively. The green, black, magenta, and brown line colors correspond to saddle-node bifurcations from our active-cell approximations of type 1, 2, 3, and 4.

In 2D case, site-centred solution is a solution profile with odd number exited sites as shown in Figs. 4.3(a), and 4.3(c), and 4.3(e). On the other hand, bond-centred states are solutions with the excited sites bonding with other sites and forming the simplest polygon. Examples of bond-centred solutions are shown in

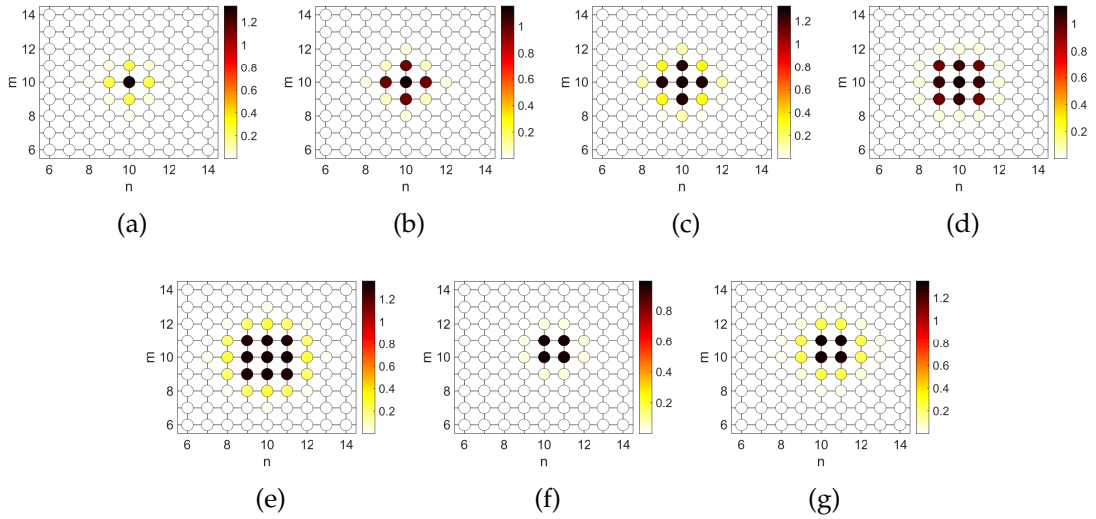

Figure 4.5. Top-view of localized solution profiles in square lattice that correspond to points in Fig. 4.4(a).

Figs. 4.3(b), 4.3(e), and, 4.3(f). Herein, we use 20×20 lattice domain and periodic boundary conditions for all of the lattice types.

By using site-centred and bond-centred solutions in Fig. 4.3 as initial guess and performing numerical continuation for varying μ, one will obtain bifurcation diagrams of the localized solutions that shows a snaking structure, see Figs. 4.4 - 4.9. Here, we use a scaled version of the $\mathbb{L}_2$ norm or "mass" norm [86]

$$M = \left(\sum_{n,m} \frac{u_{n,m}^2}{1+\sqrt{1+\mu}} \right)^{\frac{1}{2}}. \tag{4.20}$$

The snaking structures in the bifurcation diagrams exist at certain region called pinning region [76]. In 1D case, we have one pinning region, which in the limit $M \to \infty$ is bounded by two saddle-node bifurcations [24, 86]. In 2D case, saddle-node bifurcations may occur at several values of bifurcation parameter due to the presence of multiple types of saddle-node bifurcations, as we will show below. One can define that in 2D case, the pinning region is formed by the largest distance between the upper and lower saddle-node bifurcations. The snaking structure in the bifurcation diagrams may also give complicated snaking and

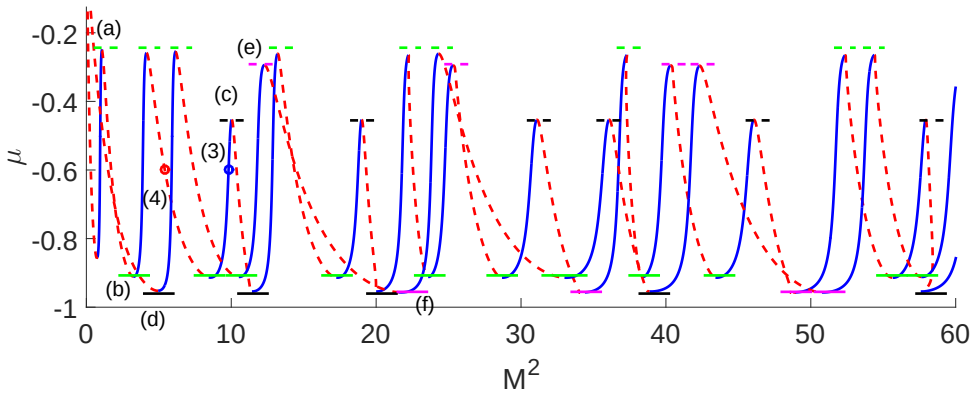

(a) $c^{\curlywedge} = 0.05$

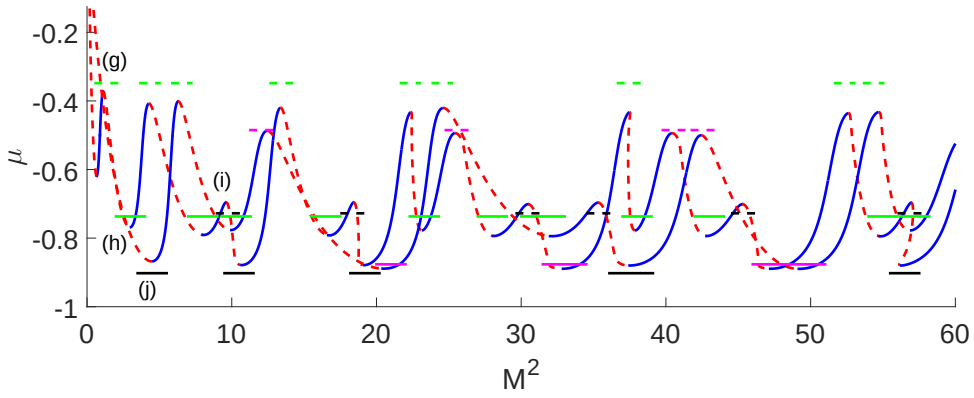

(b) $c^{\curlywedge} = 0.15$

Figure 4.6. The same as figure 4.4 for honeycomb lattice. The green, black, and magenta line colors correspond to our active-cell approximations of type 1, 2, and 3.

isolas structures [86]. In the next section, we will discuss the site-centred and bond-centred localized states and their snaking structures in square, honeycomb, and triangular lattices.

4.3.1 Square lattice

Figure 4.4 shows bifurcation diagrams for square lattice at $c^+ = 0.05$ and 0.15. As we can see, the saddle-node bifurcations occur at several bifurcation parameters μ. Moreover, the distance between the "upper" and "lower" saddle-node bifurcations are getting smaller when the coupling strength c^+ increases. In the continuum

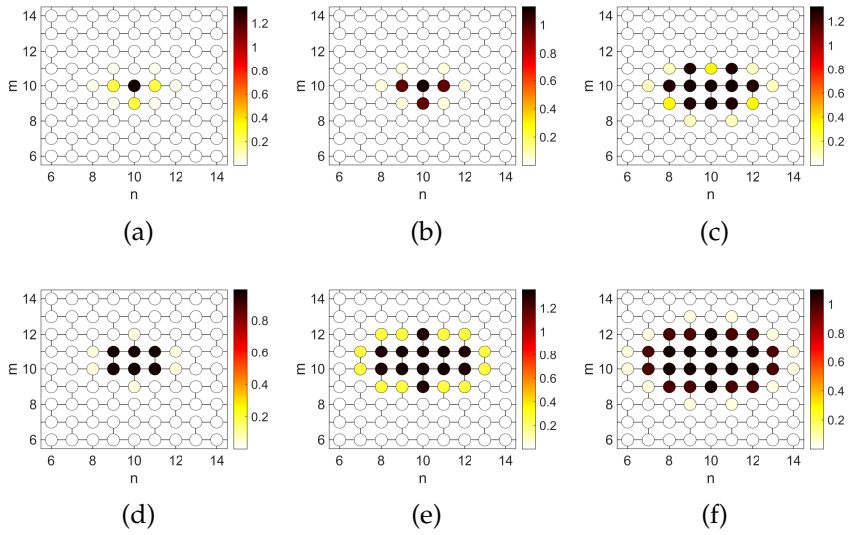

Figure 4.7. Top-view solution profiles in honeycomb lattice that correspond to points in Fig. 4.6(a).

limit $c^+ \to \infty$, the site-centred and bond-centred solutions merge as the snaking disappears, which also occurs in the 1D case.

Figures 4.5 shows several top-view (2D projection) of the solution profiles at the saddle-node bifurcations for $c^+ = 0.05$, which correspond to the bifurcation diagrams in Fig. 4.4. One can see that, as the norm M increases, the "upper" state invades "lower" state of the localized solution. In the 1D case, the mechanism of "upper" state invading "lower" state occurs around the fronts and it has two directions. In the square lattice, the front states clearly have four directions as one can deduce from the Laplacian operator Δ^+.

4.3.2 Honeycomb lattice

Figure 4.6 shows bifurcation diagrams for honeycomb lattice at $c^\curlywedge = 0.05$ and 0.15. In general, the properties of the snaking in the bifurcation diagrams are the same as square lattice. However, at the same value of coupling strength, it has larger pinning regions compared to the square lattice. It happens because the Laplacian

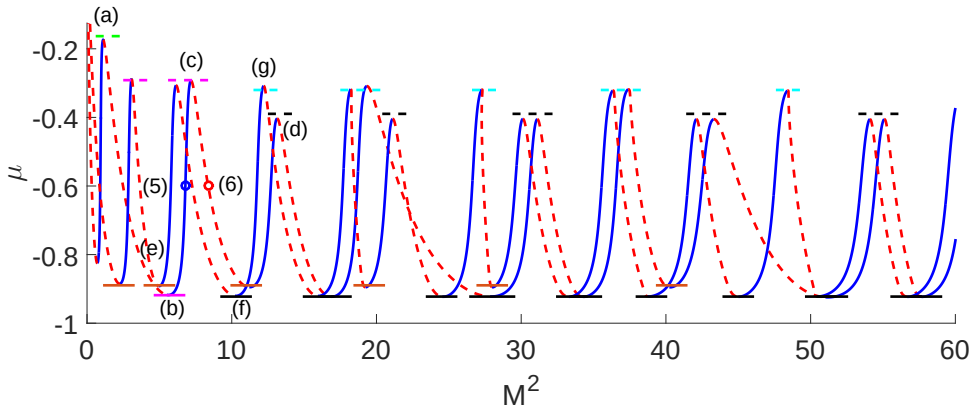

(a) $c^{\curlywedge} = 0.03$

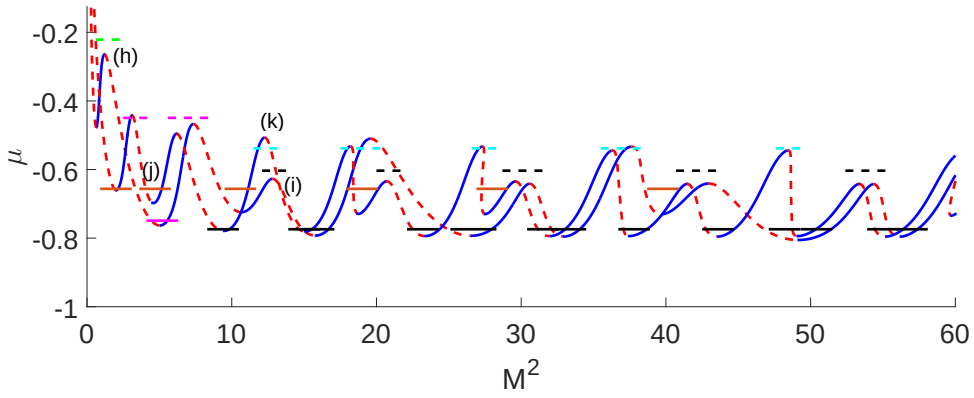

(b) $c^{\curlywedge} = 0.1$

Figure 4.8. The same as Figs. 4.4 and 4.6 for triangular lattice. The green, black, magenta, brown, and cyan line colors correspond to our active-cell approximations of type 1, 2, 3, 4, and 5.

operator $\Delta^{\curlywedge}$ for the honeycomb lattice has fewer front, i.e., three fronts, than the square lattice that connect the "upper" and "lower" states.

Figure 4.7 shows several top-view of the solution profiles at the saddle-node bifurcations for $c^{\curlywedge} = 0.05$, which correspond to the snaking bifurcations in Fig. 4.6(a). The localized solution behavior also has the same mechanism as that in the square lattice, where the "upper" state invades the "lower" state as the norm M increases.

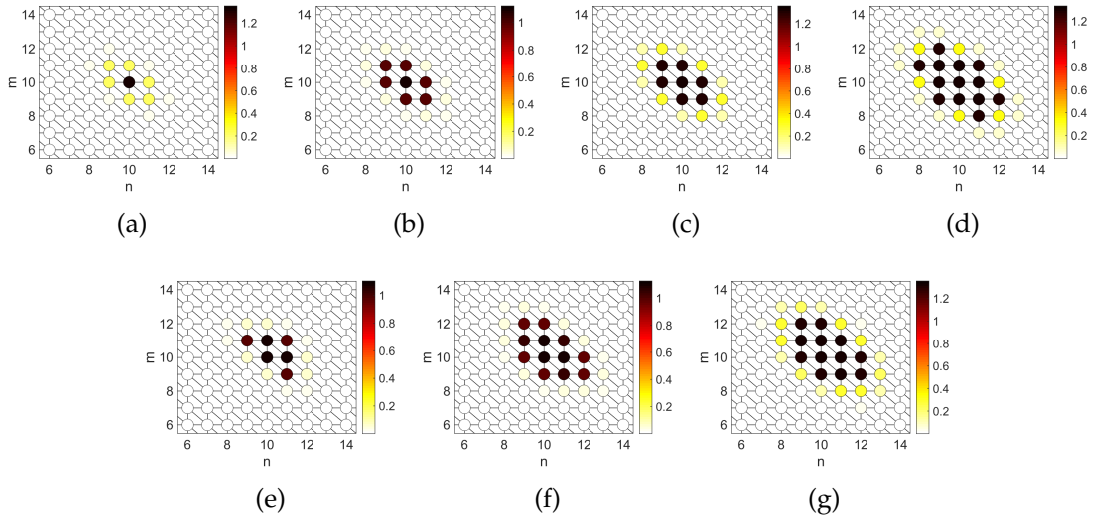

Figure 4.9. Top-view solution profiles in triangluar lattice that correspond to points in Fig. 4.8(a).

4.3.3 Triangular lattice

Figure 4.8 shows bifurcation diagrams for triangular lattice at $c^{\ast} = 0.03$ and 0.1. The main difference between the square, honeycomb and triangular lattices is that the triangular lattice has relatively the smallest pinning region at the same value of coupling strength. It happens because the triangular lattice has six fronts in the Laplacian operator $\Delta^{\ast}$. Several top-view solution profiles at the saddle-node bifurcations are shown in Fig. 4.9 for $c^{\ast} = 0.03$, which correspond to bifurcation diagrams in Fig. 4.8(a).

In summary, the number of cells that involve in the Laplacian operator determines the 2D lattice front direction. One can say that the width of the pinning region is inversely proportional to the number of fronts, which is not the same as in the 1D case.

Square lattice

Type	a	b
1	1	4
2	2	4
3	1	3
4	1	2

Honeycomb lattice

Type	a	b
1	1	3
2	2	3
3	1	2

Triangular lattice

Type	a	b
1	1	4
2	2	5
3	2	5
4	2	6
5	2	4

Table 4.1: List of coefficients in the active-cell approximations for all lattices.

4.4 Saddle-node bifurcation analysis

In general, when the coupling strength is quite small (weakly coupled), the solution consists of only three states, i.e., "upper" state U_1, "lower" state U_0, and front (active-cell). By using the assumption, we can assume that there are only three states that involve in the dynamics. Hence, we can re-write equation (4.3) into a simple ordinary differential equation [61]

$$\dot{x} = F(x) = \mu x + 2x^3 - x^5 + Z(x), \tag{4.21}$$

where

$$Z(x) = c^{\square}\left(aU_1 - bx\right), \tag{4.22}$$

and x is the front. The coefficients a and b are determined by the type of lattice and the number of "upper" state U_1, "lower" state U_0, and active-cell at the front. The list of coefficients a and b are shown in Table 4.1 for the square, honeycomb, and triangular lattices. In general, $F(x)$ can have five real roots. Note that only two of them are related to the snaking as they correspond to the "upper" and "lower" saddle-node bifurcations. One can recognise that a saddle-node bifurcation is a condition when $F(x)$ at the local minimum $x = x_\alpha$ and local maximum $x = x_\beta$ vanishes, which correspond to the "lower" and "upper" saddle-node bifurcations,

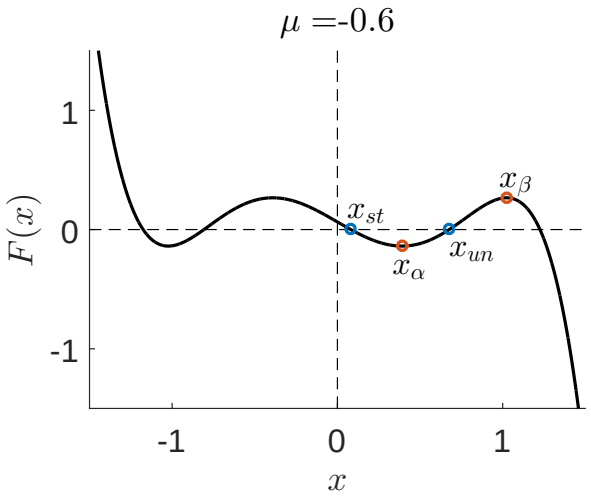

Figure 4.10. Active-cell function type 1 for square lattice at $c^{+} = 0.05$. x_{α} and x_{β} indicate as lower and upper saddle-node bifurcations. x_{st} and x_{un} represent the stable and unstable cell solution.

respectively. It is quite straightforward to obtain that

$$x_{\alpha,\beta} = \left(\frac{3}{5} \pm \frac{1}{5}\sqrt{9 + 5(\mu - c^{\square} b)}\right)^{\frac{1}{2}}. \tag{4.23}$$

We found that there are several types of saddle-node bifurcations in the snaking diagrams. By identifying the types of saddle-node bifurcations, we can apply the active-cell approximation to the solution profiles. In particular, we have four, three, and five types of saddle-node bifurcations for the square, honeycomb, and triangular lattices, which are classified by the numbers and positions of the "upper" state U_1, "lower" state U_0, and active-cell in their solution profiles, see Figs. 4.11, 4.12, and 4.13. One also can say that the active-cell approximation is a rotation invariant at their center or axes. The approximations for all of the saddle-node bifurcation results are shown in Figs. 4.4, 4.6, and 4.8.

4.4.1 Square lattice

Figure 4.4(a) shows several types of saddle-node bifurcations and their approximations for the square lattice at $c^+ = 0.05$. In general, there are four types of saddle-node bifurcations for the square lattice, see Fig. 4.11.

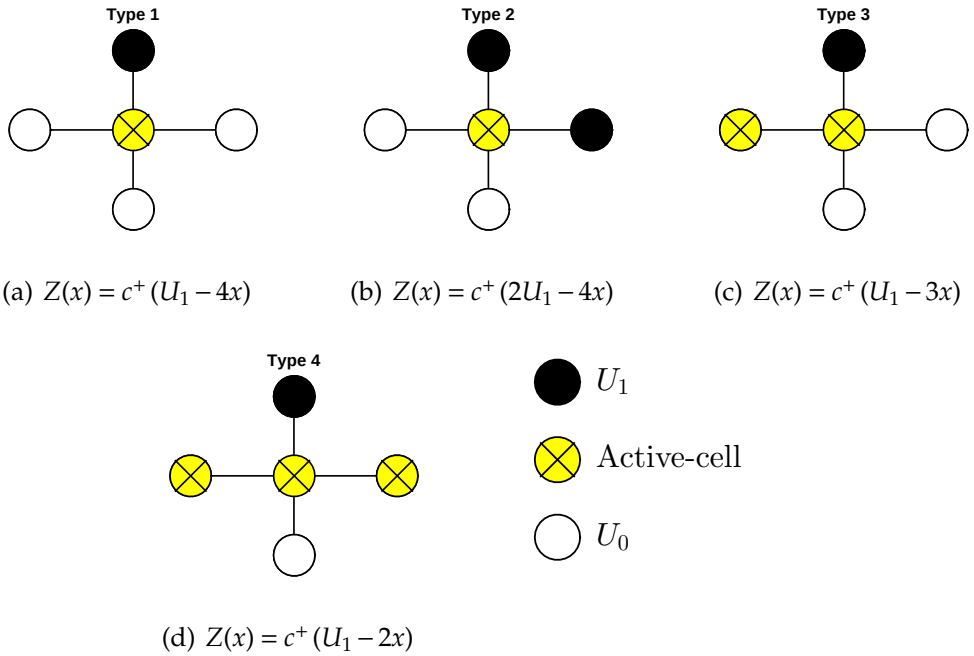

Figure 4.11. Types of active-cell approximations for square lattice.

The bifurcations at points (a) and (b), (c) and (d), (f) and (g), and (e) are belong to type 1, 2, 3, and 4, respectively. The saddle-node bifurcations of type 1 and 3 only appear in site-centred and bond-centred solutions. Meanwhile, type 2 and 4 may appear in both site-centred and bond-centred solutions. The approximations for all of the types give good agreement for the "lower" and "upper" saddle-node bifurcations. Note that type 2 and 4 mostly appear in the large value of norm M.

Figure 4.4(b) shows the approximation results of the saddle-node bifurcations for square lattice at $c^+ = 0.15$. By comparing between $c^+ = 0.05$ and 0.15, one can see that the active-cell approximations give better results at smaller coupling strength. As we can see, the active-cell approximations fail to approximate points (h), (i), (j), and (k). These happen because the solution fronts that do not satisfy the active-cell

approximation assumption. As the coupling is getting larger, one will have more cells with different amplitudes around the fronts that are also excited.

4.4.2 Honeycomb lattice

Figure 4.6(a) shows several types of saddle-node bifurcations and their approximations for the honeycomb lattice at $c^\curlywedge = 0.05$. In general, there are three types of saddle-node bifurcations for the honeycomb lattice, see Fig. 4.12.

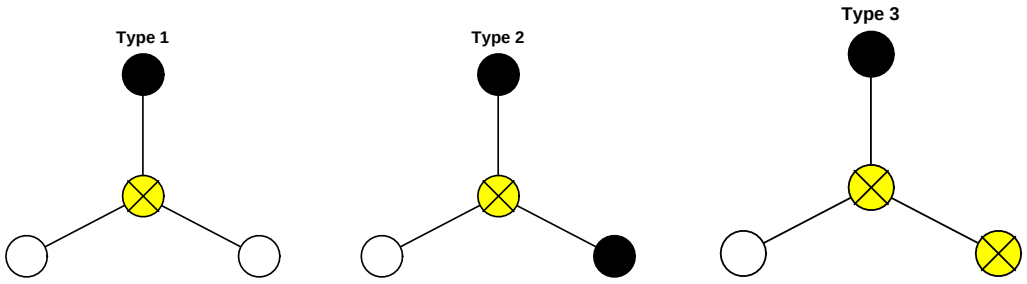

(a) $Z(x) = c^\curlywedge(U_1 - 3x)$ (b) $Z(x) = c^\curlywedge(2U_1 - 3x)$ (c) $Z(x) = c^\curlywedge(U_1 - 2x)$

Figure 4.12. Types of active-cell approximations for honeycomb lattice.

The bifurcations at points (a) and (b), (c) and (d), and (f) and (g) are belong to type 1, 2, and 3, respectively. All of the types of saddle-node bifurcations appear in site-centred and bond-centred solutions. Generally, the approximation for all of the types give good agreement for the "lower" and "upper" saddle-node bifurcations.

Figure 4.6(b) shows the approximation results of the saddle-node bifurcations for honeycomb lattice at $c^\curlywedge = 0.15$. By comparing between $c^\curlywedge = 0.05$ and 0.15, one can see that the active-cell approximations give better results at smaller coupling strength. As we can see, the active-cell approximations fail to approximate points (g), (h), (i), and (j). These also happen due to the solution fronts that do not satisfy the active-cell approximation assumption. As the coupling is getting larger, one will have more cells with different amplitudes around the fronts that are also excited, which also happen in square lattice.

4.4.3 Triangular lattice

Figure 4.8(a) shows several types of saddle-node bifurcations and their approximations for the triangular lattice at $c^{\divideontimes} = 0.03$. In general, there are five types of saddle-node bifurcations for the triangular lattice, see Fig. 4.13.

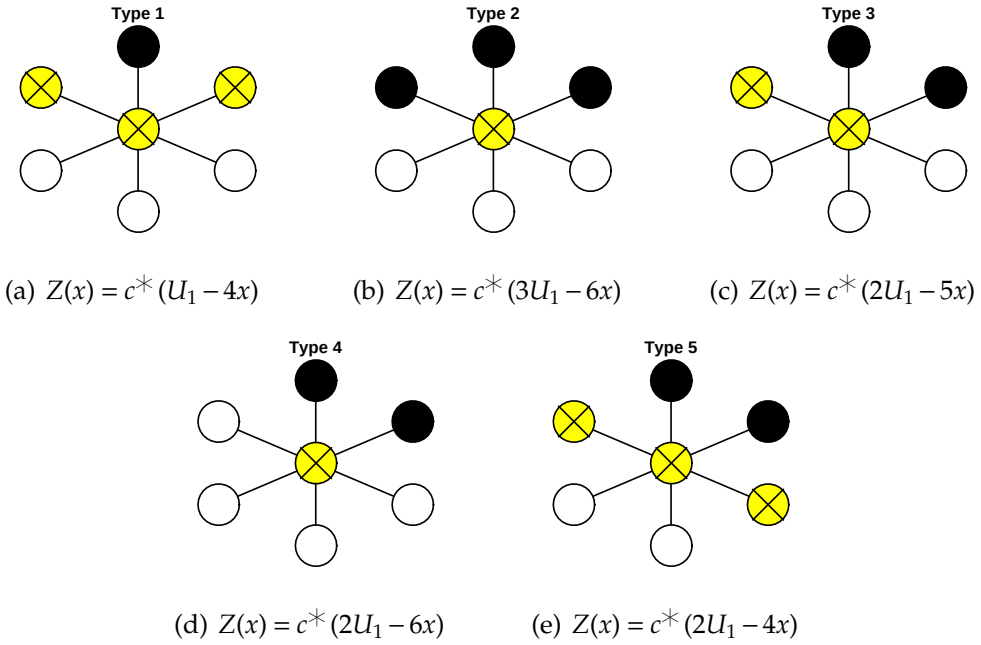

(a) $Z(x) = c^{\divideontimes}(U_1 - 4x)$ (b) $Z(x) = c^{\divideontimes}(3U_1 - 6x)$ (c) $Z(x) = c^{\divideontimes}(2U_1 - 5x)$

(d) $Z(x) = c^{\divideontimes}(2U_1 - 6x)$ (e) $Z(x) = c^{\divideontimes}(2U_1 - 4x)$

Figure 4.13. Types of active-cell approximations for triangular lattice.

The bifurcations at points (a), (d) and (f), (b) and (c), (e), and (g) are belong to type 1, 2, 3, 4, and 5, respectively. All of the types of saddle-node bifurcations appear in site-centred and bond-centred solutions. In general, the approximation for all of the types give good agreement for the "lower" and "upper" saddle-node bifurcations. Note that type 4 and 5 only appear in the "lower" and "upper" saddle-node bifurcations, respectively.

Figure 4.8(b) shows the approximation results of the saddle-node bifurcations for triangular lattice at $c^{\divideontimes} = 0.1$. By comparing between $c^{\divideontimes} = 0.03$ and 0.1, one can see that the active-cell approximations also give better results at smaller coupling strength. As we can see, the active-cell approximations fail to approximate points (h), (j), (k), (k), (l), and (n). These also happen due to the solution fronts do not

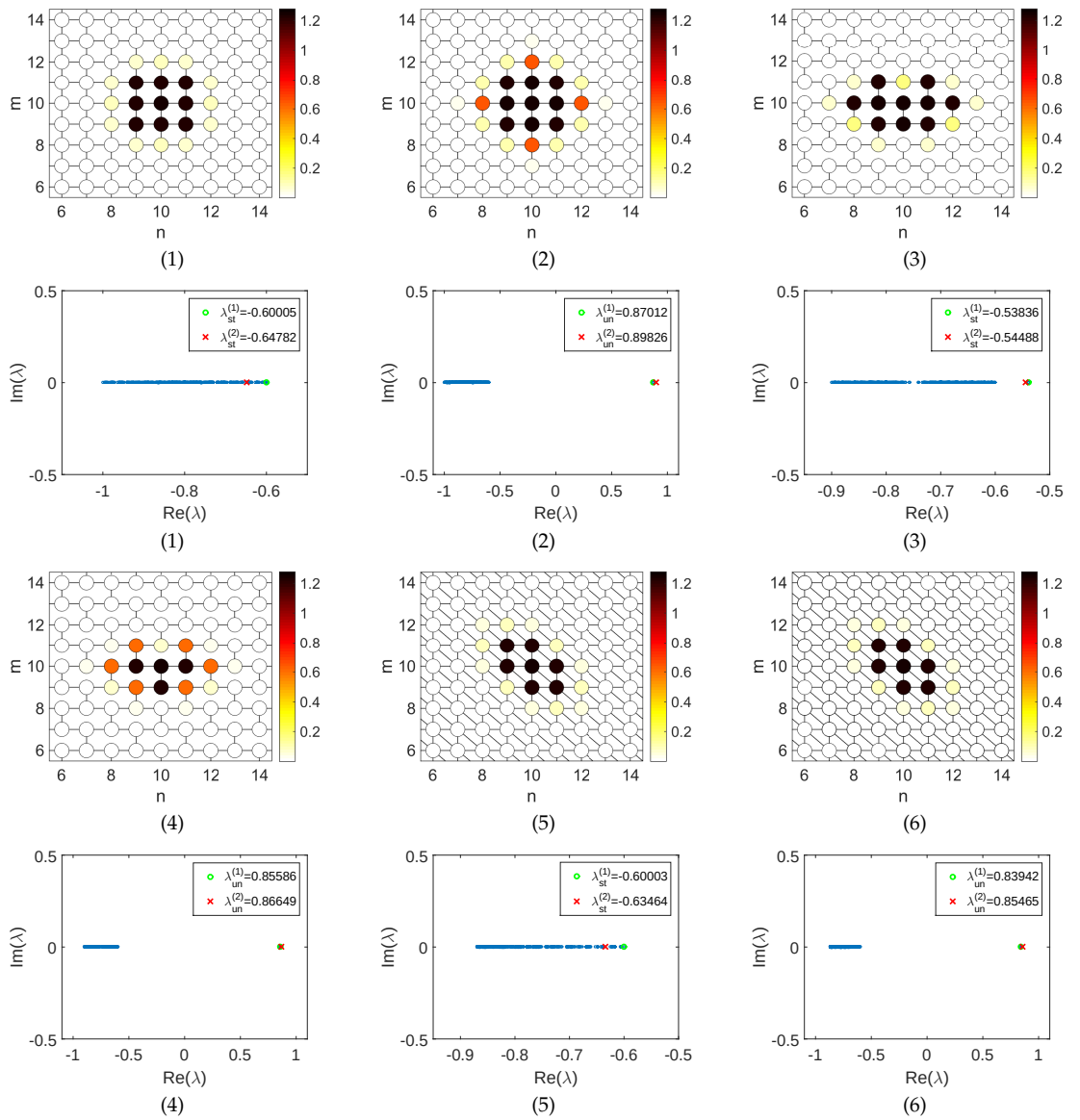

Figure 4.14. Plot of the localized states, their corresponding numerical eigenvalues, and critical one obtained the active-cell approximation indicated in Figs. 4.4(a), 4.4(b), 4.6(a), 4.6(b), 4.8(a), and 4.8(b) for stable and unstable site-centered solutions for all of the lattice types.

satisfy the active-cell approximation assumption. As the coupling is getting larger, one will have more cells with different amplitudes around the fronts that are also excited, which also happens in square and honeycomb lattices.

All in all, at a relatively small coupling strength, the active-cell approximation is a good approximator, especially when we have a fewer number of fronts in the Laplacian operator. Thus, at the same coupling strength, honeycomb lattice gives

the best result because it has three fronts while square and triangular lattices have four and six fronts, respectively. Note that the first saddle-node bifurcation that appear right after the branching points of localized solutions for all of the lattice types cannot be approximated by our method because the solutions are rather close to the continuum limit.

4.4.4 Eigenvalue approximation

The active-cell approximation also can to be used to approximate the critical eigenvalue of the equation (4.3) for all of the lattice domains. By considering our assumption in equation (4.21), it is straightforward that from the linearization, one can obtain the eigenvalue problem

$$\lambda x = \frac{d}{dx} F(x)\Big|_{x=x_{st,un}} x, \tag{4.24}$$

i.e., λ is given by

$$\lambda(\mu) = \mu + 6x_{st,un}^2 - 5x_{st,un}^4 + \frac{\partial Z(x_{st,un})}{\partial x_{st,un}}. \tag{4.25}$$

Our approximation of the critical eigenvalue at points (1)-(6) indicated in Figs. 4.4(a), 4.6(a), and 4.8(a) is shown in Fig. 4.14, where good results are obtained when the coupling is weak.

4.5 Conclusions

We have considered two-dimensional discrete Allen-Cahn equation with cubic and quintic nonlinearities in the domain of square, honeycomb, and triangular lattices. We have studied numerically and analytically the time-independent solutions, i.e., uniform and localized states and their stabilities.

Our numerical results show that the snaking structures from the localized states for all of the lattice structures can have many types of saddle-node bifurcations. Herein, we propose an active-cell approximation to estimate the saddle-node bifurcations. The results show that our assumption gives good agreement for weakly-coupled system, i.e., small coupling strength and fewer exited cells around the fronts of a localized solution. Moreover, we also showed that our approximation can be used to approximate the critical eigenvalue of localized states.

The idea of the work here may be extended to spatially continuous systems, where the “lattice types" can be imposed by introducing spatial heterogeneity through periodic-in-space linear potentials (see, e.g, [56] for a 1D problem that exhibits similar behaviors with a discrete setup [61]).

Chapter 5

Conclusions

In this thesis, we have studied bifurcations of localized solutions and their stability in several discrete systems, namely, the discrete Swift-Hohenberg equation, the discrete optical cavity equation with saturable nonlinearity, and 2D discrete Allen-Cahn equation with cubic and quintic nonlinearity on square, honeycomb and triangular lattices. Let us now summarize the work and the main results obtained in Chapters 2-4 and also point out several problems that would be interesting as future works.

5.1 Summary

In Chapter 1, we presented background information of pattern formations and a general review of the past research on homoclinic snaking in continuous and discrete systems, i.e., the Swift-Hohenberg equation, a discrete optical cavity equation and the discrete Allen-Cahn equation. We also presented a numerical continuation method, which is widely used in this thesis to obtain the bifurcation curves.

In Chapter 2, we considered the discrete Swift-Hohenberg equation with cubic and quintic nonlinearity, obtained from discretizing the spatial derivatives of the

Swift-Hohenberg equation using central finite differences. We investigated the discretization effect on the bifurcation behavior. There are three regions of the parameter intervals (i.e., $h < 1$ (strong coupling), $1 \leq h < 2$ (intermediate), $h \geq 2$ (weak coupling)) wherein the discrete Swift-Hohenberg equation behaves either similarly or differently from the continuum limit. When $1 \leq h \leq 2$, multiple Maxwell points can occur for the periodic solutions and may cause irregular snaking and isolas. The offset stability of the uniform solution and the pinning region are shifting for large discretization $h > 2$. Numerical continuation was used to obtain and analyze localized and periodic solutions for each case. Theoretical analysis for the snaking and stability of the corresponding solutions have been provided in the anti-continuum (uncoupled) limit.

From our studies above, we obtained that the amplitudes of periodic solution can be determined by using variational methods. Localised solutions can be approximated by using asymptotic analysis.

We also developed a one-active site approximation to determine and approximate the pinning region of localized solutions from the homoclinic snaking. The results showed that the approximation can also be used to approximate the critical eigenvalue of localized solutions. Comparisons of the analytical results and the numerics showed good agreement.

In Chapter 3, we studied time-independent solutions of an optical cavity equation with saturable nonlinearity. Localized solutions can be formed by combining two different uniform states. Homoclinic snaking from the localized solutions can be obtained by varying the bifurcation parameter P. The forming mechanism of $\Subset$-shaped isolas was also discussed, which is when the background of localized states disappear at a certain bifurcation parameter value. Herein, we also used a one-active site approximation to analyse homoclinic snaking when the

system is weakly coupled. Numerical simulations showed good agreement with the approximation for the pinning region and the critical eigenvalue.

In Chapter 4, we presented the study of time-independent solutions and their linear stabilities of the two-dimensional discrete Allen-Cahn equation with cubic and quintic nonlinearity. Three different types of lattices are considered, i.e. square, honeycomb, and triangular lattices. Herein, we extended the idea of a one-active site approximation into an active-cell approximation for two-dimensional systems. Again, numerical simulations showed that the approximation gives good agreement for all of the lattice types for weakly coupled system.

5.2 Future work

In this section, we note several problems that could be interestingly proposed as a future work. One possible problem is to study the effect of parametric time-periodic forcing to the snaking structure [46] and the mechanism for snaking or non snaking [2] for the discrete planar Swift-Hohenberg equation as we mentioned in Chapter 2. We can also consider quadratic and cubic nonlinearity for the discrete Swift-Hohenberg equation. Another problem that we could consider is including fractional derivatives to the Swift-Hohenberg or Allen-Cahn systems and analyze the effect to homoclinic snaking structures. Moreover, we also could pursue the one-active site or active-cell approximations on three-dimensional problem.

Bibliography

[1] A. V. Getling (1998). Rayleigh-Bénard Convection: Structures and Dynamics. *Singapore : World Scientific Publishing Co.*

[2] Avitabile, D., Lloyd, D. J. B., Burke, J., Knobloch, E., and Sandstede, B. (2010). To Snake or Not to Snake in the Planar Swift–Hohenberg Equation. *SIAM J. Appl. Dyn. Syst.*, 9(3):704–733.

[3] Avitabile, D. and Schmidt, H. (2015). Snakes and ladders in an inhomogeneous neural field model. *Physica D*, 294:24–36.

[4] Ball, P. (1999). The self-Made Tapestry Pattern Formation. *Trends in Medical Research*, 3.

[5] Ball, P. (2009). Shapes: nature's patterns: a tapestry in three parts. *Oxford University Press*.

[6] Barbay, S., Hachair, X., Elsass, T., Sagnes, I., and Kuszelewicz, R. (2008). Homoclinic snaking in a semiconductor-based optical system. *Phys. Rev. Lett.*, 101(25):253902.

[7] Barbay, S., Kuszelewicz, R., and Tredicce, J. R. (2011). Cavity solitons in VCSEL devices. *Adv. Opt. Tech.*, Article ID.

[8] Beaume, C., Bergeon, A., and Knobloch, E. (2011). Homoclinic snaking of localized states in doubly diffusive convection. *Phys. Fluids*, 23(9):094102.

[9] Beaume, C., Bergeon, A., and Knobloch, E. (2013). Convectons and secondary snaking in three-dimensional natural doubly diffusive convection. *Phys. Fluids*, 25(2):024105.

[10] Beck, M., Knobloch, J., Lloyd, D. J. B., Sandstede, B., and Wagenknecht, T. (2009). Snakes, Ladders, and Isolas of Localized Patterns. *SIAM J. Math. Anal.*, 41(3):936–972.

[11] Bensimon, D., Shraiman, B. I., and Croquette, V. (1988). Nonadiabatic effects in convection. *Phys. Rev. A*, 38(10):5461(R).

[12] Bentley, W. A. and Perkins, G. H. (1898). A Study of Snow Crystals. *Popular Science Monthly*, 53.

[13] Boeing, G. (2016). Visual analysis of nonlinear dynamical systems: Chaos, fractals, self-similarity and the limits of prediction. *Systems*, 4(4).

[14] Bortolozzo, U., Clerc, M. G., and Residori, S. (2009). Solitary localized structures in a liquid crystal light-valve experiment. *New Journal of Physics*, 11:093037.

[15] Bostock, D. (1994). Metaphysics books Z and H. *Clarendon Press*.

[16] Budd, C. J., Hunt, G. W., and Kuske, R. (2001). Asymptotics of cellular buckling close to the Maxwell load. *R. Soc. Lond. Proc. Ser. A Math. Phys. Eng. Sci.*, 457(2016):2935–2964.

[17] Budd, C. J. and Kuske, R. (2005). Localized periodic patterns for the non-symmetric generalized Swift-Hohenberg equation. *Physica D*, 208(1-2):73–95.

[18] Burke, J. and Dawes, J. H. P. (2012). Localised states in an extended Swift-Hohenberg equation. *SIAM J. Appl. Dyn. Syst.*, 11(1):261–284.

[19] Burke, J. and Knobloch, E. (2006). Localized states in the generalized Swift-Hohenberg equation. *Phys. Rev. E*, 73(5):056211.

[20] Burke, J. and Knobloch, E. (2007a). Homoclinic snaking: Structure and stability. *Chaos*, 17:037102.

[21] Burke, J. and Knobloch, E. (2007b). Snakes and ladders: Localized states in the Swift-Hohenberg equation. *Phys. Lett. A*, 360(6):681–688.

[22] Carretero-González, R., Talley, J. D., Chong, C., and Malomed, B. A. (2006). Multistable solitons in the cubic-quintic discrete nonlinear Schrödinger equation. *Physica D*, 216(1):77–89.

[23] Chapman, S. J. and Kozyreff, G. (2009). Exponential asymptotics of localised patterns and snaking bifurcation diagrams. *Physica D*, 238(3):319–354.

[24] Chong, C., Carretero-González, R., Malomed, B. A., and Kevrekidis, P. G. (2009). Multistable solitons in higher-dimensional cubic-quintic nonlinear Schrödinger lattices. *Physica D*, 238(2):126–136.

[25] Chong, C. and Pelinovsky, D. E. (2011). Variational approximations of bifurcations of asymmetric solitons in cubic-quintic nonlinear Schrödinger lattices. *Discrete & Continuous Dynamical Systems - S*, 4(5):1019–1031.

[26] Christov, C. I. and Velarde, M. G. (1995). Dissipative solitons. *Physica D*, 86(1-2):323–347.

[27] Clerc, M. G., Elias, R. G., and Rojas, R. G. (2010). Continuous description of lattice discreteness effects in front propagation. *Phil. Trans. R. Soc. A*, 369(1935):412–424.

[28] Clerc, M. G. and Falcon, C. (2005). Localized patterns and hole solutions in one-dimensional extended systems. *Physica A*, 356(1):48–53.

[29] Collet, P. (1998). Amplitude Equation for Lattice Maps , A Renormalization Group Approach. *Journal of Statistical Physics*, 90(5-6):1075–1105.

[30] Coullet, P., Riera, C., and Tresser, C. (2000). Stable static localized structures in one dimension. *Phys. Rev. Lett.*, 84(14):3069.

[31] Cross, M. C. and Hohenberg, P. C. (1993). Pattern formation outside of equilibrium. *Reviews of Modern Physics*, 65(3):851–1112.

[32] Dawes, J. H. P. (2008). Localized Pattern Formation with a Large-Scale Mode: Slanted Snaking. *SIAM J. Appl. Dyn. Syst.*, 7(1):186–206.

[33] Dawes, J. H. P. (2010). The emergence of a coherent structure for coherent structures: localized states in nonlinear systems. *Phil. Trans. R. Soc. A*, 368(1924):3519–3534.

[34] Dean, A., Matthews, P., Cox, S., and King, J. (2014). Orientation-dependent pinning and homoclinic snaking on a planar lattice. *SIAM J. Appl. Dyn. Syst.*, 14(1):481–521.

[35] Dean, A. D., Matthews, P. C., Cox, S. M., and King, J. R. (2011). Exponential asymptotics of homoclinic snaking. *Nonlinearity*, 24(12):3323–3351.

[36] Dionne, B., Silber, M., and Skeldon, A. C. (1997). Stability results for steady, spatially periodic planforms. *Nonlinearity*, 10(2):321.

[37] Doedel, E., Paffenroth, R. C., Champneys, A. R., Fairgrieve, T., Kuznetsov, Y. A., Oldeman, B., Sandstede, B., and Wang, X. (2002). AUTO2000 : A numerical bifurcation software. *Available to download from http://indy.cs.concordia.ca/auto/*.

[38] Doedel, E. J., Champneys, A. R., Dercole, F., Fairgrieve, T., Yu, A., Oldeman, B., Paffenroth, R., Sandstede, B., Wang, X., and Zhang, C. (2007). AUTO-

07P: Continuation and bifurcation software for ordinary differential equations. *Available to download from http://indy.cs.concordia.ca/auto/.*

[39] Douady, S. and Couder, Y. (1992). Phyllotaxis as a physical self-organized growth process. *Phys. Rev. Lett.*, 68(13):2098.

[40] Egorov, O., Etrich, C., Peschel, U., and Lederer, F. (2003). Discrete quadratic cavity solitons in waveguide arrays. *European Quantum Electronics Conference, EQEC 2003*, page 196.

[41] Egorov, O., Lederer, F., and Staliunas, K. (2007a). Subdiffractive discrete cavity solitons. *Optics Letters*, 32(15):2106–2108.

[42] Egorov, O. a. and Lederer, F. (2013). Spontaneously walking discrete cavity solitons. *Optics Letters*, 38(7):1010–1012.

[43] Egorov, O. A., Lederer, F., and Kivshar, Y. S. (2007b). How does an inclined holding beam affect discrete modulational instability and solitons in nonlinear cavities? *Optics Express*, 15(7):4149–4158.

[44] Firth, W. J., Columbo, L., and Maggipinto, T. (2007). On homoclinic snaking in optical systems. *Chaos*, 17:037115.

[45] French, A. P. (1971). Vibrations and waves. *CRC press*.

[46] Gandhi, P., Beaume, C., and Knobloch, E. (2015). A New Resonance Mechanism in the Swift–Hohenberg Equation with Time-Periodic Forcing. *SIAM J. Appl. Dyn. Syst.*, 14(2):860–892.

[47] Golubitsky, M., Swift, J. W., and Knobloch, E. (1984). Symmetries and pattern selection in Rayleigh-Bénard convection. *Physica D*, 10(3):249–276.

[48] Govaerts, W. J. F. (2000). Numerical Methods for Bifurcations of Dynamical Equilibria (Google eBook). *SIAM*, page 362.

[49] Haeckel, E. (2012). Art forms in nature. *Courier Corporation*.

[50] Haeckel, E. (2013). Kunstformen der Natur. *BoD–Books on Demand*.

[51] Haudin, F., Rojas, R. G., Bortolozzo, U., Residori, S., and Clerc, M. G. (2011). Homoclinic snaking of localized patterns in a spatially forced system. *Phys. Rev. Lett.*, 107(26):264101.

[52] Hilali, M. F., Métens, S., Borckmans, P., and Dewel, G. (1995). Pattern selection in the generalized Swift-Hohenberg model. *Phys. Rev. E*, 51(3):2046.

[53] Hunt, G. W., Peletier, M. A., Champneys, A. R., Woods, P. D., Wadee, M. A., Budd, C. J., and Lord, G. J. (2000). Cellular buckling in long structures. *Nonlinear Dynamics*, 21(1):3–29.

[54] Hunter, J. K. and Nachtergaele, B. (2001). Applied Analysis. *Singapore : World Scientific Publishing Co.*

[55] Judd, S. L. and Silber, M. (2000). Simple and superlattice Turing patterns in reaction–diffusion systems: bifurcation, bistability, and parameter collapse. *Physica D*, 136(1-2):45–65.

[56] Kao, H.-C., Beaume, C., and Knobloch, E. (2014). Spatial localization in heterogeneous systems. *Phys. Rev. E*, 89(1):012903.

[57] Keller, H. B. (1987). Numerical Methods In Bifurcation Problems. *Applied Mathematics*, 217:50.

[58] Knobloch, E. (2008). Spatially localized structures in dissipative systems: Open problems. *Nonlinearity*, 21(4):T45–T60.

[59] Kozyreff, G., Assemat, P., and Chapman, S. J. (2009). Influence of boundaries on localized patterns. *Phys. Rev. Lett.*, 103(16):164501.

[60] Kozyreff, G. and Chapman, S. J. (2006). Asymptotics of large bound states of localized structures. *Phys. Rev. Lett.*, 97(4):044502.

[61] Kusdiantara, R. and Susanto, H. (2017). Homoclinic snaking in the discrete Swift-Hohenberg equation. *Phys. Rev. E*, 96(6):062214.

[62] Laing, C. R., Troy, W. C., Gutkin, B., and Ermentrout, G. B. (2001). Multiple bumps in a neuronal model of working memory. *SIAM J. Appl. Math.*, 63(1):62–97.

[63] Lindenmayer, A. (1968). Mathematical models for cellular interactions in development II. Simple and branching filaments with two-sided inputs. *Journal of Theoretical Biology*, 18(3):300–315.

[64] Lloyd, D. and Sandstede, B. (2009). Localized radial solutions of the Swift-Hohenberg equation. *Nonlinearity*, 22(2):485.

[65] Lloyd, D. J., Gollwitzer, C., Rehberg, I., and Richter, R. (2015). Homoclinic snaking near the surface instability of a polarisable fluid. *J. Fluid Mech.*, 783:283–305.

[66] Lloyd, D. J. B., Sandstede, B., Avitabile, D., and Champneys, A. R. (2008). Localized Hexagon Patterns of the Planar Swift–Hohenberg Equation. *SIAM J. Appl. Dyn. Syst.*, 7(3):1049–1100.

[67] Lloyd, D. J. B. and Scheel, A. (2017). Continuation and Bifurcation of Grain Boundaries in the Swift-Hohenberg Equation. *SIAM J. Appl. Dyn. Syst.*, 16(1):252–293.

[68] Matthews, P. C. and Susanto, H. (2011). Variational approximations to homoclinic snaking in continuous and discrete systems. *Phys. Rev. E*, 84(6):066207.

[69] McCalla, S. and Sandstede, B. (2010). Snaking of radial solutions of the multi-dimensional Swift-Hohenberg equation: A numerical study. *Physica D*, 239(16):1581–1592.

[70] Mccullen, N. and Wagenknecht, T. (2016). Pattern Formation on Networks: From Localised Activity to Turing Patterns. *Scientific Reports*, 6:1–13.

[71] Oppenheim, A. (2011). Signals and Systems. *Prentice Hall*, pages 1–50.

[72] Padovan, R. (1999). Proportion: Science, Philosophy, Architecture. *Taylor & Francis*.

[73] Peletier, L. A. and Rodríguez, J. A. (2004). The Discrete Swift-Hohenberg Equation. *University of Leiden. Mathematical Institute*.

[74] Peschel, U., Egorov, O., and Lederer, F. (2004). Discrete cavity soliton. *Optics Letters*, 29(16):1909–1911.

[75] Plateau, J. A. F. (1873). Statique expérimentale et théorique des liquides soumis aux seules forces moléculaires. *Gauthier-Villars*, 2.

[76] Pomeau, Y. (1986). Front motion, metastability and subcritical bifurcations in hydrodynamics. *Physica D*, 23(1-3):3–11.

[77] Rankin, J., Avitabile, D., Baladron, J., Faye, G., and Lloyd, D. J. B. (2013). Continuation of localised coherent structures in nonlocal neural field equations. *SIAM J. Sci. Comput.*, 36(1):B70–B93.

[78] Rodríguez, J. A. (2004). *Patterns described by Discrete and Continuous Dynamical systems*. PhD thesis.

[79] Sakaguchi, H. and Brand, H. R. (1996). Stable localized solutions of arbitrary length for the quintic Swift-Hohenberg equation. *Physica D*, 97(1-3):274–285.

[80] Sakaguchi, H. and Brand, H. R. (1997). Stable localized squares in pattern-forming nonequilibrium systems. *Europhys. Lett.*, 38(5):341–346.

[81] Seydel, R. (2009). Practical bifurcation and stability analysis. *Springer*, 5(3):346–346.

[82] Stevens, P. S. (1974). Patterns in nature. *Atlantic Monthly*.

[83] Susanto, H., Kusdiantara, R., Li, N., Kirikchi, O. B., Adzkiya, D., Putri, E. R. M., and Asfihani, T. (2018). Snakes and ghosts in a parity-time-symmetric chain of dimers. *Phys. Rev. E*, 97(6):062204.

[84] Susanto, H. and Matthews, P. C. (2010). Variational approximations to homoclinic snaking. *Phys. Rev. E*, 84(6):066207.

[85] Swift, J. and Hohenberg, P. C. (1977). Hydrodynamic fluctuations at the convective instability. *Phys. Rev. A*, 15(1):319.

[86] Taylor, C. and Dawes, J. H. (2010). Snaking and isolas of localised states in bistable discrete lattices. *Phys. Lett. A*, 375(1):14–22.

[87] Thompson, J. M. T. (2015). Advances in Shell Buckling: Theory and Experiments. *Int. J. Bifurcation Chaos*, 25:1530001.

[88] Tlidi, M., Averlant, E., Vladimirov, A., and Panajotov, K. (2012). Delay feedback induces a spontaneous motion of two-dimensional cavity solitons in driven semiconductor microcavities. *Phys. Rev. A*, 86(3):033822.

[89] Turing, A. M. (1952). The chemical basis of morphogenesis. *Phil. Trans. R. Soc. B*, 237(641):37–72.

[90] Uecker, H. and Wetzel, D. (2014). Numerical Results for Snaking of Patterns over Patterns in Some 2D Selkov–Schnakenberg Reaction-Diffusion Systems. *SIAM J. Appl. Dyn. Syst.*, 13(1):94–128.

[91] Von Kármán, T. (1963). Aerodynamics. *McGraw-Hill New York*, 9.

[92] Wickler, W. (1968). Mimicry in plants and animals. *London: Weidenfeld & Nicolson*.

[93] Wood, E. A. (1975). Science from your airplane window. *Courier Corporation*.

[94] Woods, P. and Champneys, A. (1999). Heteroclinic tangles and homoclinic snaking in the unfolding of a degenerate reversible Hamiltonian Hopf bifurcation. *Physica D*, 129(3-4):147–170.

[95] Yi, X., Wattis, J. A., Susanto, H., and Cummings, L. J. (2009). Discrete breathers in a two-dimensional spring-mass lattice. *J Phys A; Math Theor*, 42(35):355207.

[96] Yulin, A. and Champneys, A. (2011). Snake-to-isola transition and moving solitons via symmetry-breaking in discrete optical cavities. *Discrete & Continuous Dynamical Systems - S*, 4(5):1341–1357.

[97] Yulin, A. V. and Champneys, A. R. (2010). Discrete snaking: multiple cavity solitons in saturable media. *SIAM J. Appl. Dyn. Syst.*, 9(2):391–431.

[98] Yulin, A. V., Champneys, A. R., and Skryabin, D. V. (2008). Discrete cavity solitons due to saturable nonlinearity. *Phys. Rev. A*, 78(1):011804(R).